THE SEDIMENTARY ARCHITECTURE OF MEANDERING RIVERS: THE INFLUENCE OF BEND MIGRATION STYLE

BY

ALEXANDRA SANCHEZ

THESIS

Submitted in partial fulfillment of the requirements
for the degree of Master of Science in Geology
in the Graduate College of the
University of Illinois Urbana-Champaign, 2022

Urbana, Illinois

Advisor:

Professor James Best

ABSTRACT

Meandering rivers are ubiquitous in nature and play a major role in shaping the landscape and creating ecological diversity. Their deposits can also form a significant component of ancient alluvium. Past research has shown that meander bends and their point bars can display different modes of planform migration, such as expanding across the floodplain, translating down valley, and expanding/rotating. Numerical models and interpretations from outcrops have suggested that these different migration styles influence what is preserved in the sedimentary facies. However, few studies have sought to assess the validity of these assertions in modern rivers: the present thesis studies the classic Wabash River in Illinois as a site to test these ideas.

In this study, ground penetrating radar (GPR) surveys, multibeam echo sounder surveys (MBES), and remote sensing have been used to examine the Wabash River and test if migration style influences the subsurface sedimentary features. Two bends with different migration styles – an expanding (Maier Bend) and a translating (TB3) bend - were chosen to study the nature and rate of bend movement and links to facies characteristics and type. GPR surveys were conducted on the exposed meander point bars at low flow and established a series of flow normal and flow parallel GPR lines. When interpreting GPR data, the GPR facies are first described as the types of reflectors seen in the GPR profiles, allowing interpretation of the GPR facies in terms of sedimentary facies and subsurface architecture. In addition, the facies interpretations of the present thesis are compared to other models and studies conducted on meandering rivers.

Six GPR facies were identified. Facies 1 is divided into two categories. Facies 1a consists of low-angle (~5-13˚) reflectors with high-angle reflectors (20-30˚) or small-scaled trough-shaped (concave-upwards) reflectors packaged in between, which were interpreted as the point bar (accretion surfaces) migrating downstream with smaller scale superimposed bedforms.

Facies 1b has the same low-angle reflectors but lacks the small-scale features (bedforms) in between. Facies 2 consists of high angle reflectors (~15-32˚) and is 0.2-2m thick and interpreted as the deposits of unit bars. Facies 3 comprises small, concave-upwards, trough-shaped reflectors (1-2 m wide) interpreted as the deposits of dunes. Facies 4 is represented as larger-scale (10's of meters wide) trough-shaped reflectors that were interpreted as bar top hollows. Facies 5 consists of planar, parallel, reflectors, interpreted as deposition on low-angle planar surfaces, possibly by bedforms that were smaller than the resolution of the GPR. Facies 6 consists of hyperbolae, which are interpreted as either sections of the point bar with an abundance of gravel or buried tree trunks or branches.

All six of these facies were found in both bends with differing migration style, but in different abundance as assessed by quantification of facies types in every GPR section. Facies 1 was the dominant facies overall within Maier and TB3 bends. However, the distinguishing characteristic between the two bends is the abundance of Facies 1a (lateral accretion surfaces with small scale surface features) versus Facies 1b (lateral accretion surfaces with no small-scale features). Facies 1b is interpreted more frequently in Maier Bend than in TB3, and Facies 1a occurs more frequently in TB3 compared to Maier Bend. This difference is less likely due to differing bend migration styles and more likely due to grain size differences and the angle at which the GPR surveys were taken. Facies 2 (unit bars) were found more frequently in TB3 in comparison to Maier Bend, possibly due to the dominance of unit bars in a downstream translating bend, potentially making it a distinctive characteristic of a translating bend. Facies 3 (dunes) increases in abundance from upstream to downstream in both bends but is found more frequently in TB3. The abundance of Facies 3 is also likely due, similar to Facies 1, to the difference in grain size with respect to the resolution of the GPR, making it difficult to identify

small dunes in the GPR profiles. Facies 4 (bar top hollows) is only found at the tail end of the point bars. TB3 has a much larger bar top hollow compared to the Maier Bend point bar that is likely due to the migration pattern of TB3 as it wraps around the bend during translation. Facies 5 (planar deposition) is only found at either thalweg depth within the point bars or filling the bar top hollow and is the least abundant facies within the point bars. Lastly, Facies 6 (hyperbolae) is highly abundant but dependent on the amount of material (e.g., gravel or trees) present to cause the point reflectors within the GPR profile.

The results of this thesis were compared to three other depositional models for meandering rivers. The first model, the depositional model of Jackson, was based on the premise that the depositional facies are dependent on the nature of flow development within bends of different curvature. The sedimentary facies determined by Jackson were compared with the facies in the present thesis and similarities are found notably in the presence of unit bars (transverse bars in Jackson's model), dunes, and accretion surfaces. Willis's theoretical model predicts variation in the three-dimensional geometry of meander bend large-scale stratigraphy with differing bend geometry and hydraulics. The slopes and depositional patterns of Maier bend and TB3 point bars were compared to the Willis's predicted bedding geometry, showing similarities in the angle and shape of the bedding geometry slopes. However, the grain size distribution was a significant discrepancy between Willis's model and the Wabash River and thus may impart some discrepancies between the two. Lastly, the model of Hagstrom et. al was based on high-quality 3-D seismic data and information from hundreds of wellbores, testing if the accretion-package geometry affects the lithological variability of point bars. When comparing this model to the results of the present thesis, it was found that they were not entirely comparable due to the width of accretion surfaces not being able to be measured in the GPR

profiles. However, the overall depositional patterns found in the specific bend migration styles found in both studies were similar.

ACKNOWLEDGMENTS

To start, I would like to thank my advisor, Dr. Jim Best, for guiding me through writing my first thesis. I have learned a lot about what a thesis should and should not be. He has helped me discover what I enjoy about studying geology, and helped introduce many new and interesting research topics that I would not have easily found on my own. Additionally, I thank him through the many meetings discussing and trouble shooting how to conduct research and collect data during a pandemic. Lastly, I thank Jim for challenging me to write a thesis that I would be happy with.

I would also like to thank Dr. Kory Konsoer, LSU, and Dr. Taylor Rowley, USGS, for sharing their data with me when I could not collect my own due to the pandemic. Without them, this thesis would not exist. This dataset has been fascinating to study and I cannot wait to share the final results with you both.

Furthermore, I would like to thank my parents for supporting me in going back to school, even though my mom said I would be old by the time I finished. Despite that, they always encouraged me to do what is best for my career and life whether I went back to school or moved three-thousand miles away to live in new country. I would also like to thank my partner, Arete, for supporting me during my time here by listening to me rant about any frustrations, making me food for me during my late nights, and letting me cry into their shoulder when I thought I could not finish this thesis.

Lastly, I would like to thank my fellow geology graduate students, particularly Nooreen Meghani. Nooreen has been an amazing friend that has given me a lot of support in both my academic career and in my personal life as well.

TABLE OF CONTENTS

CHAPTER 1: INTRODUCTION

1.1 The Importance of Meandering Rivers

Meandering rivers are abundant in nature and provide many resources or habitat for humans and fauna (Ward and Stanford, 1995; Nagayama and Nakamura, 2018). Due to their importance to humans and the environment, meandering rivers have attracted the interest of many geoscientists to study the processes that drive their evolution and deposition products. The dynamics of meandering rivers are connected to processes that change and develop the floodplain, which in the long-term play a major role in shaping the surrounding landscape and transportation of sediment (Rhoads, 2020).

In addition to shaping the landscape and affecting life, meandering river deposits also form a significant component of ancient alluvium (Ghinassi et. al., 2014). Extensive research has examined modern channels and outcrops to develop models that explain the processes that create the deposits of meandering rivers. Past research has shown that meander bends and their point bars can show different types of planform migration (Figure 1.4), that include: point bars expanding across the flood plain, expanding/rotating, translating down valley or a combination of these modes (Jackson, 1976a; Ghinassi et. al. 2014). Numerical models and outcrop interpretations have proposed that different modes of migration influence what is preserved in the sedimentary facies (Willis, 1993; Ghinassi et al., 2014; Hagstrom et al., 2019). However, there have been few studies that assess the validity of these assertions in modern rivers.

1.2 Flow Processes and Deposition in Meandering Rivers

In the classic model for meandering rivers, flow within meander bends is characterized by a helicoidal motion with a component of surface flow towards the outer bank and bottom flow towards the inner bank (Figure 1.1). The thalweg (Figures 1.3 &1.4), the deepest part of the river

channel, corresponds approximately with the zone of maximum velocity, with scour pools developing near the outer bend. In simple meander bends, the velocity, asymmetry, and position of the thalweg swap over to the opposite side of the channel as the helicoidal flow changes its direction (Figure 1.1; Collinson, 1978). As a result of this flow pattern, the outer concave bank is where erosion occurs, and deposition occurs on the inner convex bank (Figure 1.1) that causes the channel to migrate transversely to the flow to deposit sediment by lateral accretion (image A in Figure 1.2; Collinson, 1978).

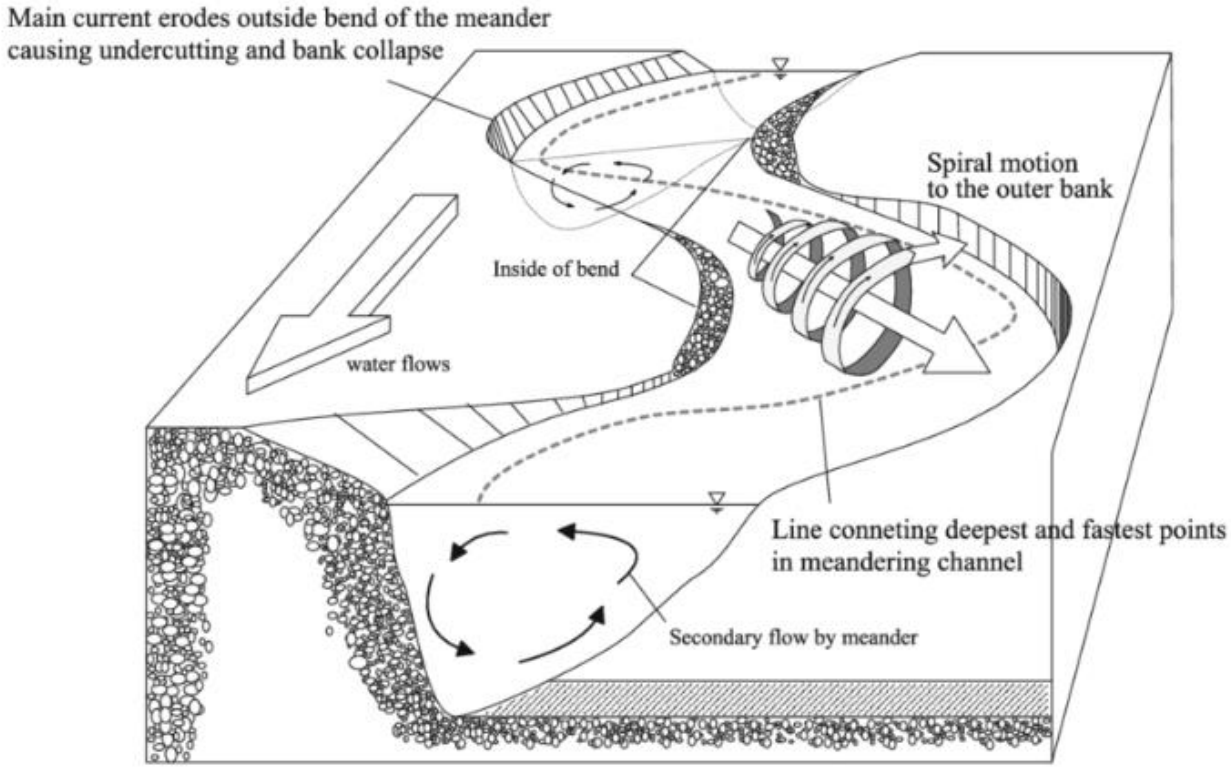

Figure 1.1: Physical processes in typical meandering channel, showing the effect of flow on deposition and erosion in the channel. From Park and Ahn, 2019.

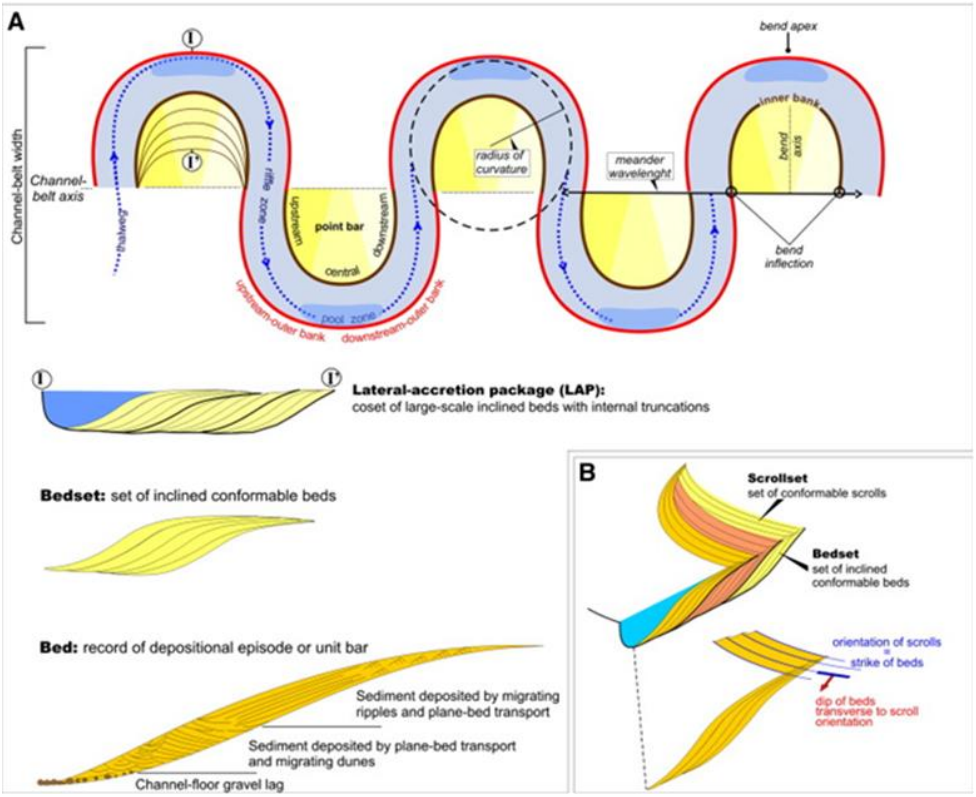

Figure 1.2: A: Nomenclature for meander-belt morphology and point-bar architecture, showing the deposition of lateral accretion packages in point bars. **B:** Relationship between stratal architecture and scroll-bar morphology. From Ghinassi et. al., 2016.

This pattern of water flow (Figure 1.1) within a meander bend determines deposition on the point bar. The classic model was first outlined by van Bendegom (1947), developed by Allen (1970a, b) and then extended by Bridge (1975, 1977), assuming a bankfull discharge and fully helicoidal flow around the bend (Figure 1.1). When farther from the thalweg, depth, velocity, and boundary shear stress lessen; and in combination with the upslope component of the helicoidal flow, these factors lead to the near-bed flow separating the grain sizes. As a result, this separation of grain sizes causes upward fining within the point bar deposits as seen in Figures 1.3 and 1.4 (Collinson, 1978). Besides the upward-fining sequence of grain size within point bar deposits, there are common types and patterns of bedforms that occur in the classic model of point bar deposition. Lateral accretion surfaces are preserved as a form of large scale, low angle cross-stratification (Figures 1.2 & 1.4). The angle as which these cross beds dip range from 1

degree to 25 degrees depending on the size of the meandering river and the bed material grain size. The thickness of the beds is uncertain but can be approximately equal to the channel depth (Miall, 1981). According to the classic model, dunes tend to be the dominant bedforms, in sand-bed rivers, particularly on the lower sections of point bars (Figure 1.4). On the upper sections of the point bars, ripples and plane beds occur most frequently (Figure 1.4). In addition to these common bedforms, there are also scroll bars that are elongated ridges that are approximately parallel to the point bars (Figure 1.4; Collinson, 1978). Although this classic model is widely accepted, others have argued that it is only one of several different models that can be applied to meandering river deposits (Miall, 1981).

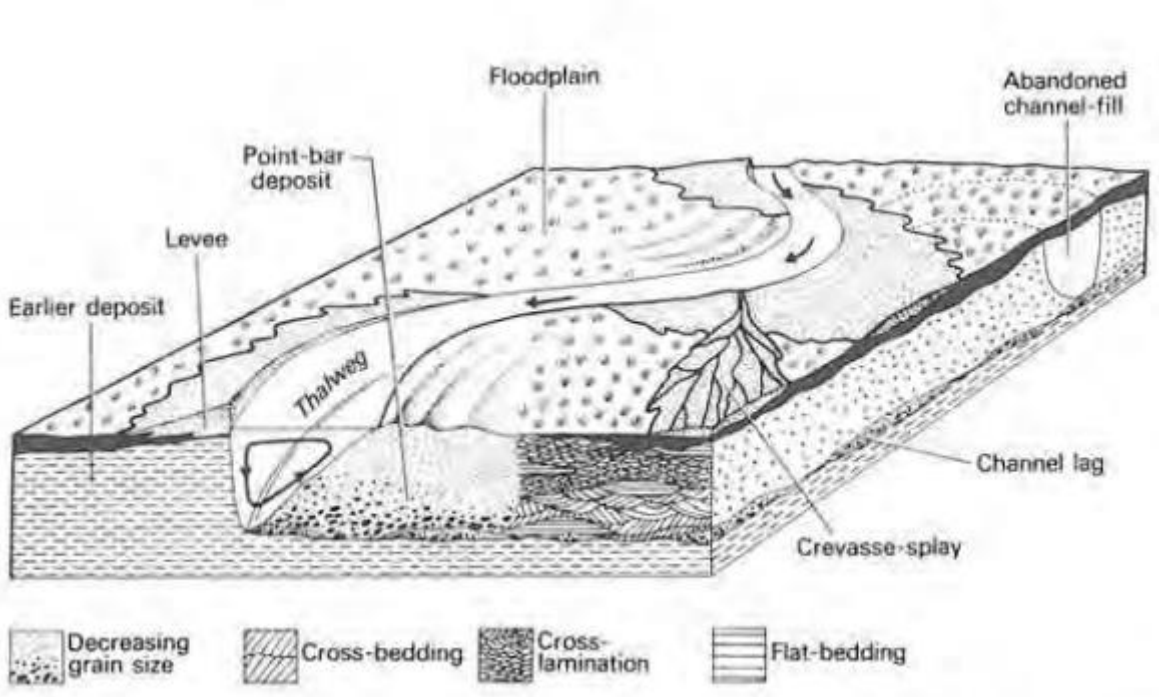

Figure 1.3: The classic point bar model for a meandering stream (after Allen, 1964, 1970b). Within the channel, the thalweg is labeled and a simplified example of flow through a meandering channel is demonstrated. The point bar deposit shows examples of facies expected in the rock record as well as the fining upward sequence of grain size. From Collinson, 1978.

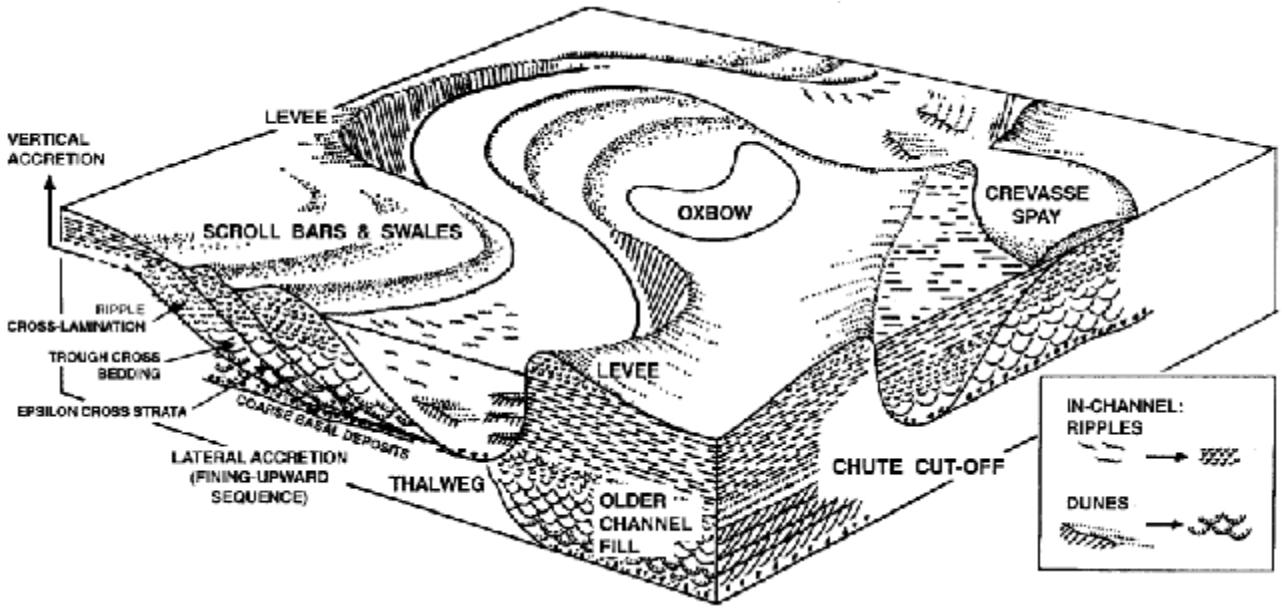

Figure 1.4: Another example of a meandering river based on the classic meandering river facies model, showing the geomorphic setting and sedimentological elements of the upward fining sequence (modified from Walker and Cant, 1984). From Hickin, 1978.

One model that challenged the classic model is the depositional model developed by Jackson (1976a), which is based on his research on bends in the Lower Wabash River. The depositional model of Jackson (1976a) showed that the classic fining-upward profile only occurs in the downstream section of the bend (Figure 1.7). The model demonstrates that on almost all meander bends that the helicoidal flow (Figures 1.1 & 1.5) is not developed immediately at the inflection point, but instead, the helicoidal flow patterns develops over a finite distance (Jackson, 1976a; Collinson, 1978; Miall, 1981). The upstream part of the meander bend inherits the flow pattern from the next bend upstream with the rotation of the flow in the opposite direction (Jackson, 1975b, 1976a). Consequently, three gradational zones can be determined around any meander bend (Jackson, 1975a, b). These zones include: a ‘transitional’ zone which is influenced by the upstream bend; a ‘fully developed’ zone where the local bend controls the flow and the classical model is applicable; and an ‘intermediate’ zone where the flow pattern transitions from one into the other (Jackson, 1976a; Collinson, 1978). The changing flow conditions while

moving downstream as well as the curvature of the bend (Figure 1.6) are reflected in the bedforms that are found on the surface and within the vertical sequence (Figure 1.7; Jackson, 1976a; Collinson, 1978).

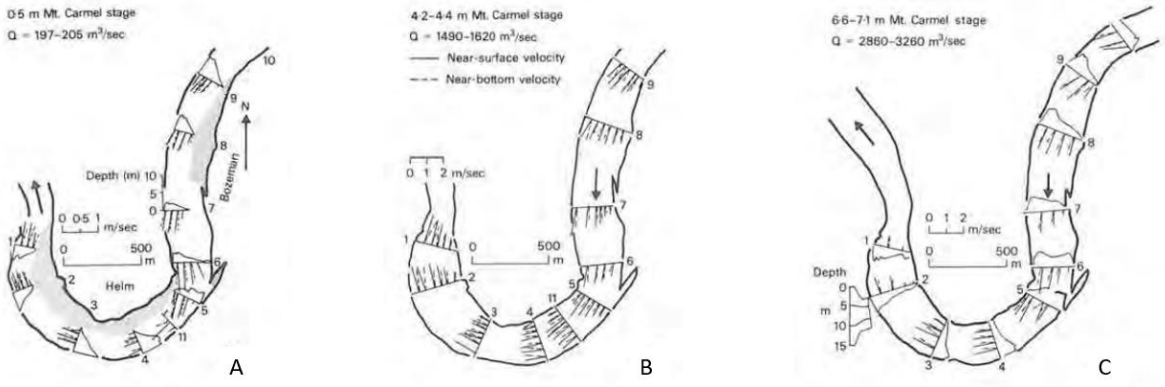

Figure 1.5: The variation of water flow patterns and facies distributions on point bars in the Lower Wabash River. **A-C:** Cross-channel profiles and velocity distribution at Helm Bend at increasing values of discharge. From Jackson, 1975b.

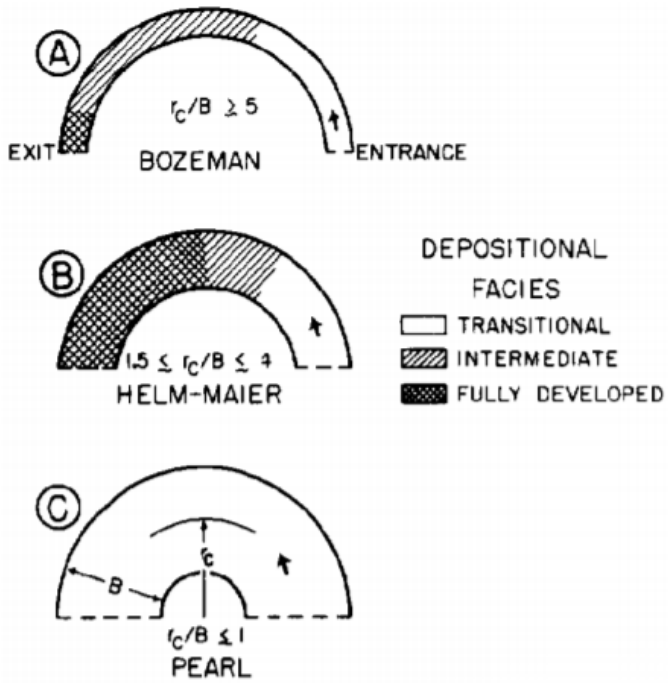

Figure 1.6: A-C: Distribution of depositional facies around meander bends of different relative curvature. r_c= radius of curvature of a meander bend, measured to the center of the channel water surface. B=width of the channel, measured along the water surface. From Jackson, 1976a.

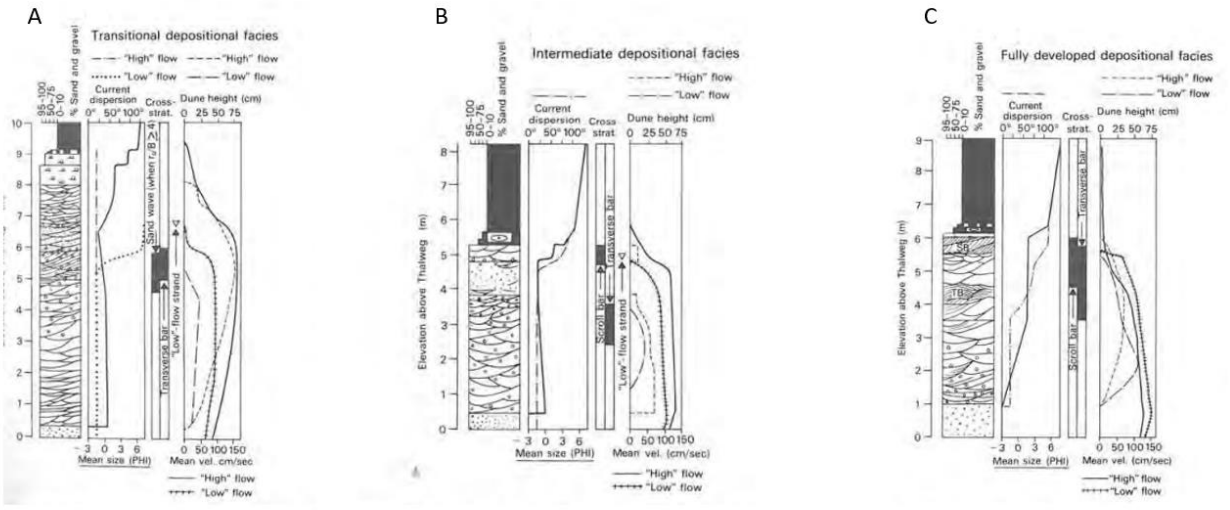

Figure 1.7: A-C: Depositional facies sequences from upstream to downstream on a point bar where the curvature is suitable for the full facies development as in the depositional model of Jackson (1976a). **A:** Transitional depositional facies. Based on transitional patterns of bedforms, current velocity, and bed-material size around Helm and Maier bends. **B:** Intermediate depositional facies. Based on patterns of bedforms, current velocity, and bed-material size along Bozeman traverses 6 and 7. **C:** Fully developed depositional facies. Based on fully developed patterns of bedforms, current velocity, and bed-material size of Helm and Maier bends. From Jackson, 1976a.

In the 'fully developed' zone (panel C in Figure 1.7), the bedform patterns follow the classical model closely; but in the 'transitional' zone, the sequence of grain size change is less evident and it may even coarsen upwards (Jackson, 1976a; Collinson, 1978). Also, the pattern of bedforms does not follow the classic model either, with bedforms such as ripples found in the lower part of the point deposits rather than dunes (Collinson, 1978). As a result, the depositional model of Jackson concludes that the vertical sequences of point bar deposits may not only vary from point bar to point bar, but also laterally within the deposits of one point bar (Jackson, 1976a; Collinson; 1978).

1.3 Style of Bend Migration and the Sedimentology in Meandering Rivers

Channel bend migration can be described in one or more of the following terms: expansion, translation, and rotation (Figure 1.8). For an expanding bend, the bend apex moves transversely from the channel belt axis (panel A in Figure 1.8; Ghinassi et al., 2014). As this

occurs, the bend curvature and flow-path both increase, which results in the channel sinuosity increasing as well. Translating bends maintain their sinuosity while the bend apex moves parallel to the channel-belt axis in the downstream direction (panel B in Figure 1.8; Ghinassi et al., 2014). Rotation of the bend occurs when the bend apex moves away from or towards the channel-belt axis (images C & D in Figure 1.8; Ghinassi et al., 2014). This causes the meander bend to become asymmetrical in shape. These patterns can also occur in combination with one another (images C&D in Figure 1.8; Ghinassi et al., 2014).

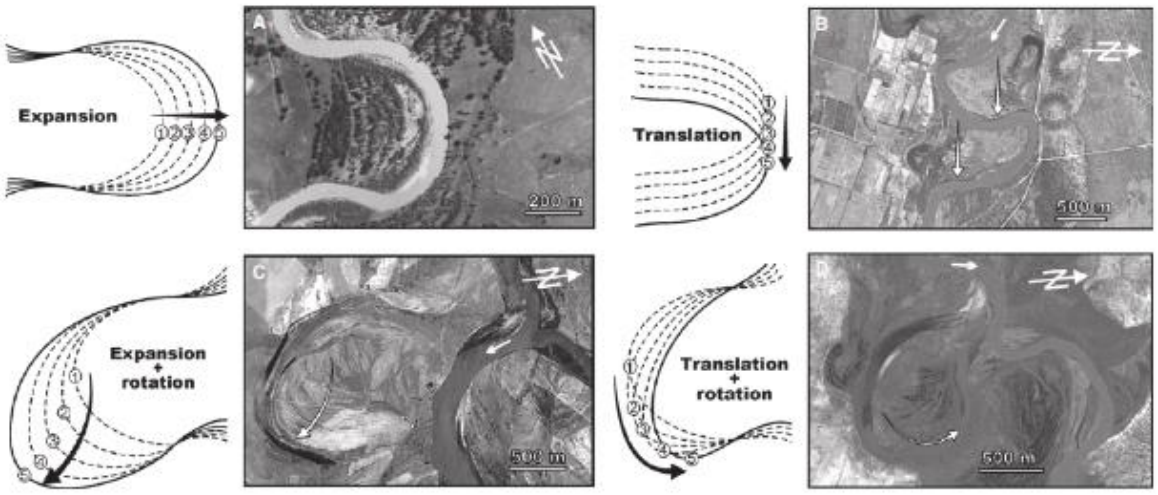

Figure 1.8: Basic planform modes of meander-bend transformation with examples from modern rivers: **A:** Murray River, Australia. **B:** Rio Colorado, Argentina. **C:** Rio Negro, Argentina. **D:** Rio Colorado, Argentina. From Ghinassi et al., 2014.

As a result, bend migration outside of expansion will affect the deposition and preservation of point bar facies that may not reflect the deposits of the classic model. For example, in addition to flow and curvature of the channel, the depositional model of Jackson (1976a) illustrates how preservation is determined by how the bends migrate. His hypotheses suggest by knowing the bend migration and flow throughout the channel, the depositional facies can be predicted. Figure 1.9 provides examples of idealized depositional facies distributions

based on the Maier, Helm, and Bozeman bends of the Wabash River in Illinois. These distributions were based on how the bend migrated as well as the bend curvature. In these specific depositional zones, the sedimentary facies should roughly reflect the sedimentary logs seen in Figure 1.7. These idealized migrations are not representative of all types of bend migration (Jackson, 1976a).

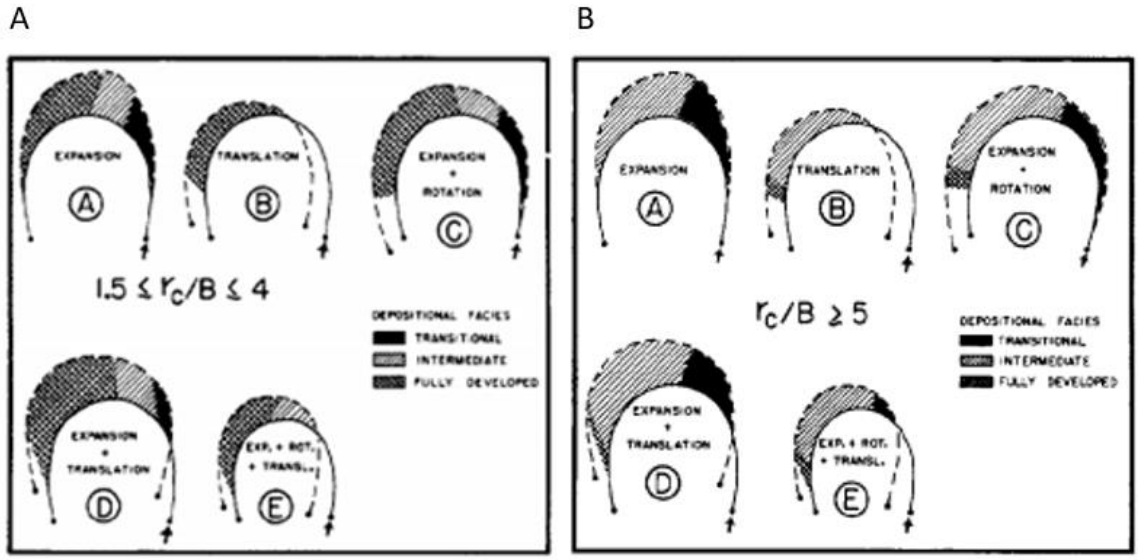

Figure 1.9: A: Preservation of depositional facies by idealized migrations of a moderately curved bend. Extent of each facies based on data for Helm and Maier bends in Jackson 1975, Table 2. **B:** Preservation of depositional facies by idealized migrations of gently curved bend. Extent of each facies based on data for Bozeman Bend in Jackson 1975, Table 2. From Jackson, 1976a.

Besides migration affecting the preservation of the depositional facies, other studies have also determined that bend migration can affect what facies are deposited at the point bar as well as the lithofacies distribution. Hagstrom et al. (2019) aimed to show that the accretion-package style affects the lithological variability of point bars. This study was based on high-quality 3-D seismic data and information from hundreds of wellbores from the Lower Cretaceous McMurray Formation in Alberta, Canada (Hagstrom et al., 2019). Five recurring accretion-package

geometries were established from this data: uniform width, wide at apex, narrow at apex, downstream wedge, and upstream wedge (Hagstrom et al., 2019). Each of these accretion-package geometries were associated with a specific type of bed migration (Figure 1.10; Hagstrom et al., 2019).

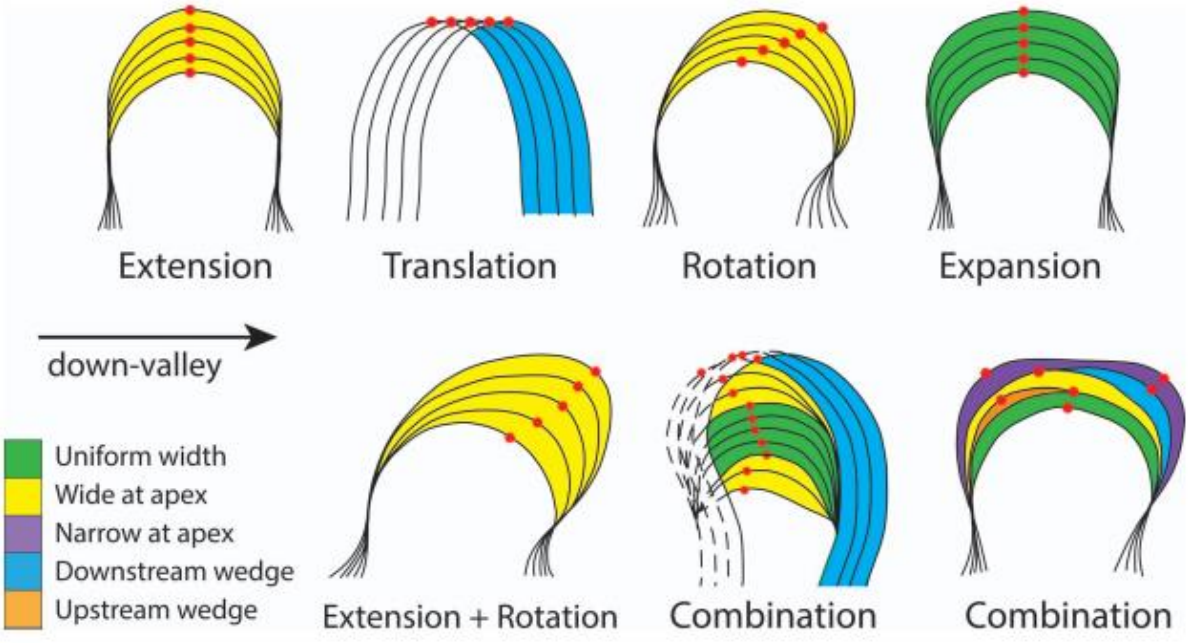

Figure 1.10: Accretionary styles created by different modes of meander migration (Daniel, 1971). Red dots are points of maximum bend curvature. Flow is clockwise. From Hagstrom et al., 2019.

For example, laterally migrating meanders are commonly associated with a "wide at apex" accretion-package geometry that is formed by sedimentation occurring at the bar apex (Hagstrom et al., 2019). Downstream-translating meanders typically are found alternating with "wide at apex" and "downstream wedge" accretion-geometry packages. The lithological changes for the translating migration style occur at the discontinuity surfaces that bound accretion packages, especially if the surface is associated with a change in migration styles (Hagstrom et al., 2019). Furthermore, Hagstrom et al. (2019) state that point bars with a greater planform complexity, resulting from multiple bend migration styles, will have a higher lithologic variability within the deposits.

Models based on modern rivers and ancient sediments are not the only method to be applied in order to understand bend migration and its effect on the deposition and preservation of point bars. Willis (1993) sought to interpret channel-bar geometry and migration of ancient river deposits; however, before that could be conducted, an understanding of the interaction between channel migration, temporal and spatial variations in channel bar surface geometry and facies, and outcrop orientation needed to be developed (Willis, 1993). As a result, Willis (1993) developed a theoretical and numerical model to predict variation in three-dimensional geometry and grain size distribution of point bar surfaces in channels of varying geometry and hydraulics. Figure 1.11 shows the results of these simulations and illustrates the progressive changes in simulated point bar geometry in profile and planform view for different types of bend migration (Willis, 1993). This theoretical model was then compared to several well-studied ancient deposits such as the Devonian Catskill Magnafacies (NY, USA) and the Miocene Siwalik Group (Potwar Plateau, Pakistan; Willis, 1993). The results of this comparison suggested that the bedding geometry and sedimentary characteristics discerned from the outcrops can be interpreted in terms of specific cross-sections through migrating channel bends of set geometry and hydraulics (Willis, 1993).

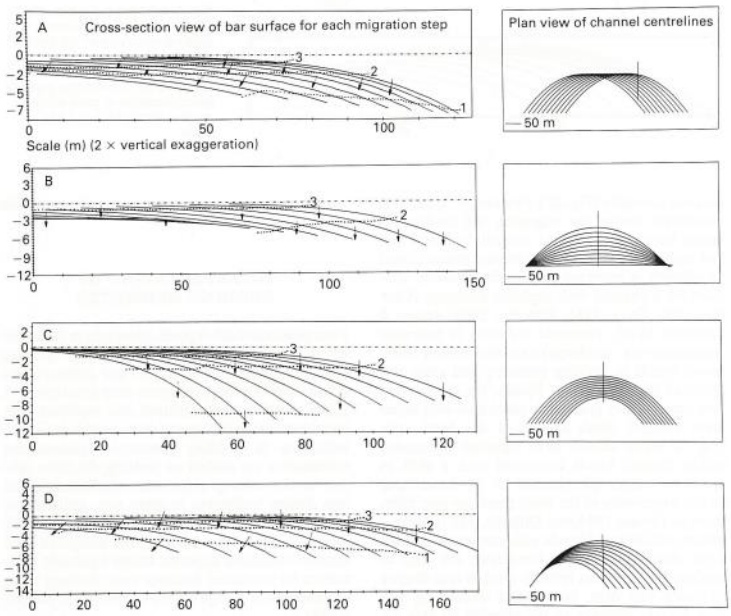

Figure 1.11: A-D: Profiles displaying progressive changes in simulated bar geometry as viewed in a plane perpendicular to the channel belt axis. Solid lines show apparent bar geometry after each migration step. Grain size contours (in phi increments) are displayed by dotted lines. Arrows show downstream channel orientation relative to the cross-section's exaggeration. Cross-section orientation relative to migrating channel centerline is displayed in box to the right of profiles. **A:** Variation in apparent bar geometry due to down valley bend translation; cross-sections progress from bend cross-over to bend apex positions. **B:** Progression of apparent point bar geometry due to sinuosity increase. All sections pass through the bend apex. **C:** Variation in apparent bar geometry with increasing bend wavelength. All profiles pass through the bend apex. **D:** Apparent bed geometry produced by increasing bend wavelength and progression from bend crossover to bend apex cross-sections. From Willis, 1993.

1.4 Motivation

There have been many studies that have reconstructed the paleoenvironments of meandering rivers by studying outcrops. However, these outcrops often show complex internal architecture with great variability, which make it challenging to yield a numerical analogue simulation for these ancient cases. Furthermore, it is difficult to create realistic models of these ancient systems. There have been some improvements in combining three-dimensional simulations with two-dimensional outcrop studies of point bar architecture (Ghinassi, et al., 2014). Despite these complexities, geoscientists have been able to use these numerical models and interpretations from outcrops to draw some conclusions on meander bend style and depositional patterns (Willis, 1993; Hagstrom et al., 2019). Both the models and interpretations,

such as those of Jackson (1976a), suggest that these different migration styles influence what is preserved in the sedimentary facies. However due to limits in technology, few studies have tested the validity of these claims in modern rivers.

Recently, there have been improvements in technology such as ground penetrating radar (GPR), multi-beam echo sounding (MBES), and remote sensing that allows geoscientists to study changes within modern river systems on a planform and bedform scale. With this improved technology, these models of point bar deposition can begin to be examined. This thesis will study two bends with differing bend migration styles in the classic Wabash River in Illinois to test these ideas. The Wabash River was chosen because it has been the site for depositional models like those of Roscoe Jackson have been described earlier in this chapter. Additionally, the stretch of the Wabash River outside of Grayville, Illinois meanders freely in its own alluvium, except for a few places that are limited by bedrock or Pleistocene glaciofluvial deposits.

1.5 Research Questions and Objectives

The main objectives of this research are to determine and quantify the sedimentary facies that are preserved within the point bar architecture of bends with different migration style to pose the following questions:

Q1) What facies characterize bends with different styles of migration?

Q2) How are these facies represented spatially in the broad alluvial architecture of these bends with different styles of migration?

Q3) How does this characterization of depositional facies compare to previous depositional models of meandering rivers?

These questions will help improve the understanding of what is preserved in the subsurface based on different bend migration styles within modern meandering rivers.

CHAPTER 2: FIELD AREA AND METHODS

2.1 Field Area

2.1.1 Location and Geology

The location of this research (Figure 2.1) is a 10km reach of the lower Wabash River near Grayville, Illinois, USA. The Wabash River is a mixed bedrock-alluvial system with bedrock outcropping within the channel with the bedrock outcrop being specifically in Maier Bend (labeled on Figure 2.1; Rowley, 2020). The bankfull width and depth for this reach are *c.* 225-300 m and 5-8m. The mean annual discharge of the lower Wabash River is 881 m^3s^{-1} with a mean annual peak discharge of 4112m^3s^{-1} that is based on 85 years of hydrologic data from a U.S. Geological Survey (USGS) gaging station at Mt. Carmel, Illinois that is roughly 20km upstream of Grayville (Konsoer et al., 2016a). This stretch of the Wabash River meanders freely across its floodplain, except in several sites where it erodes into Pleistocene glaciofluvial sediments or Carboniferous bedrock (Jackson, 1975; Konsoer et al., 2016b). No dredging operations occur in the Wabash River as it is not used for commercial navigation. The only engineering structures present are discontinuous levees that are usually set back from the channel by 100-200m (Konsoer et al., 2016a).

Within the research site, two bends were chosen for this study: Maier and Translating Bend 3 (TB3). Maier Bend (Figure 2.2) displays bend extension at the downstream end of the apex, adjusting to the erosion of the outer bank (Rowley, 2020). At the downstream end of Maier bend, there is a bedrock outcrop located on the outer bank (labeled in Figure 2.2) that acts like a lateral control point that narrows the channel (Konsoer et al., 2016a). TB3 (Figure 2.3), about 8km downstream of Maier bend, is skewed downstream and shows more deposition on the downstream end of the bar (Rowley, 2020).

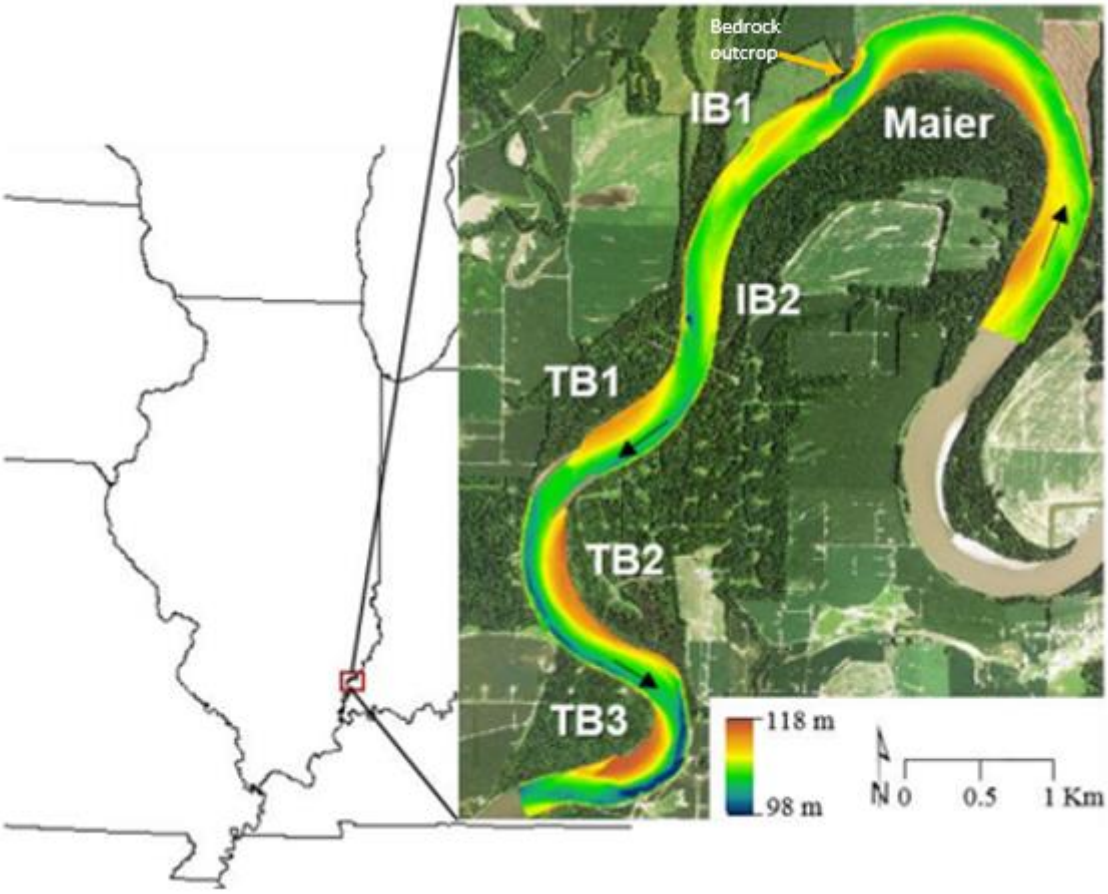

Figure 2.1: The study reach area along the Wabash River. Multibeam bathymetry displays elevation of the channel. Bend TB3 is approximately 8km downstream of Maier Bend. The black arrow indicates flow direction. Modified from Rowley, 2020.

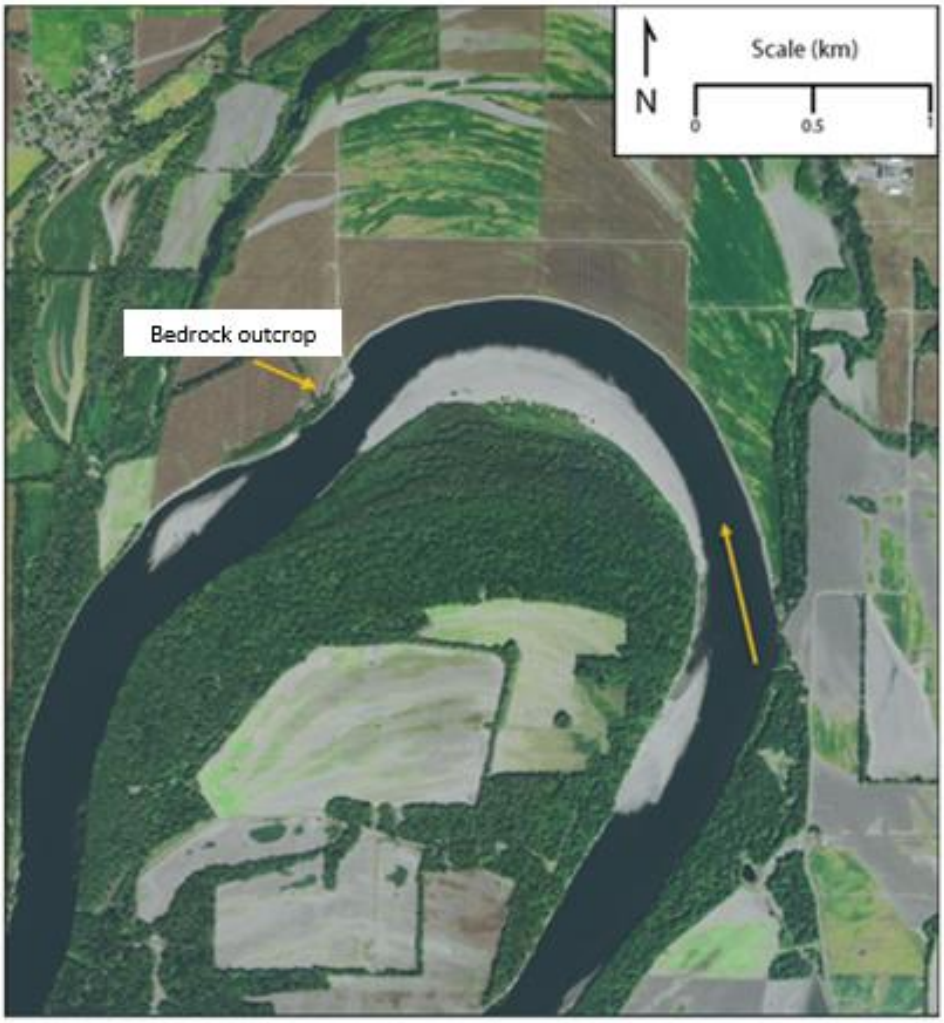

Figure 2.2: NAIP imagery of Maier Bend from 2015. Orange arrow shows direction of flow. Bedrock outcrop (labeled on image) is downstream to the Maier bend point bar.

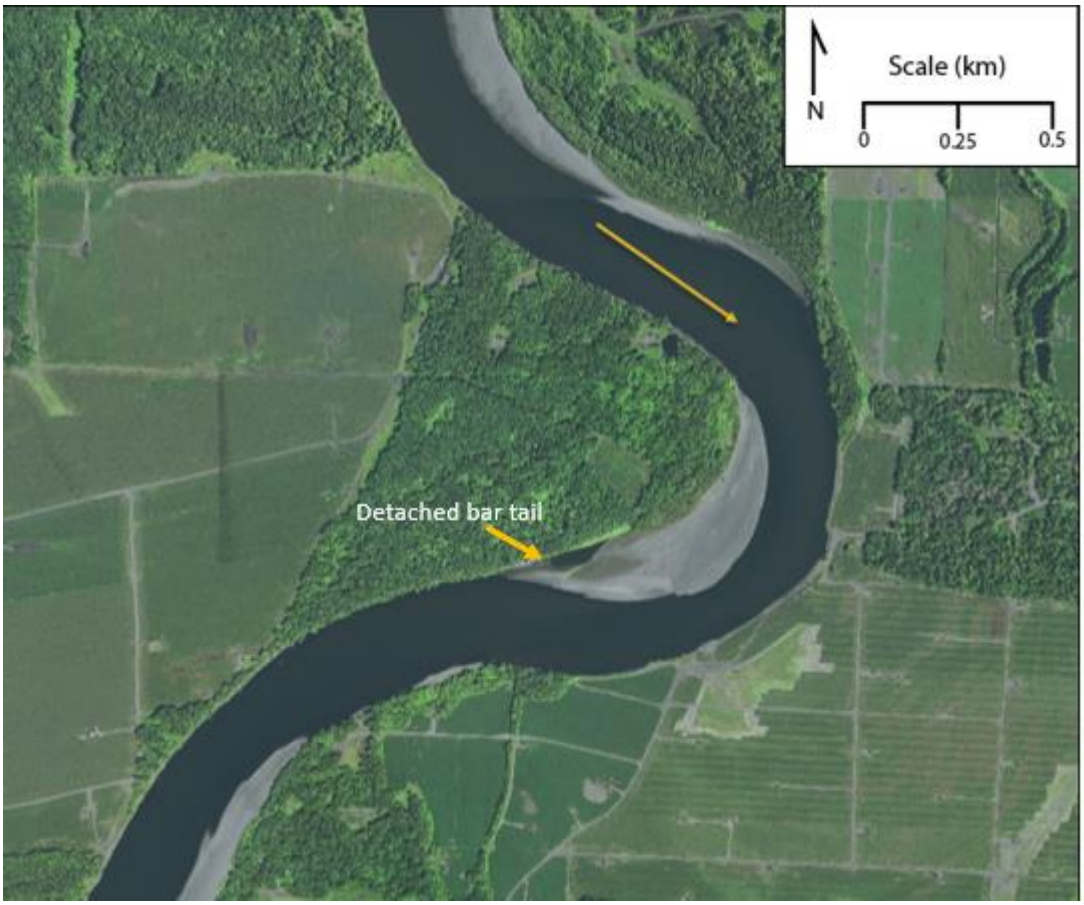

Figure 2.3: NAIP imagery of Bend TB3 from 2018. Orange arrow shows direction of flow.

2.1.2 Morphology

Within this specific stretch of the Wabash, TB3 and Maier Bend have the fastest migration rates (Table 2.1; Panel B, Figure 2.4) in comparison to the other bends since 1998 (Rowley, 2020). TB3 is undergoing rapid migration (Figure 2.4) at an average of $4.27 my^{-1}$ since 1998. The rate of migration from 1952 to 1998 was much lower at an average of $0.89 my^{-1}$. TB3 is developing through translation and expansion and has a detached bar tail (labeled in Figure 2.3; Rowley, 2020). Maier Bend also has had a rapid migration rate of $4.02\ my^{-1}$ with its 1998 apex about 1.4km upstream of the 2017 apex (Figure 2.4; Rowley, 2020). Maier Bend has two separate maxima of curvature that are indicative of a compound bend. However, Maier Bend

exhibits more distinctive characteristics of an expanding bend such as expansion occurring at the apex, and the point bar is wrapped around most of the bend (Rowley, 2020).

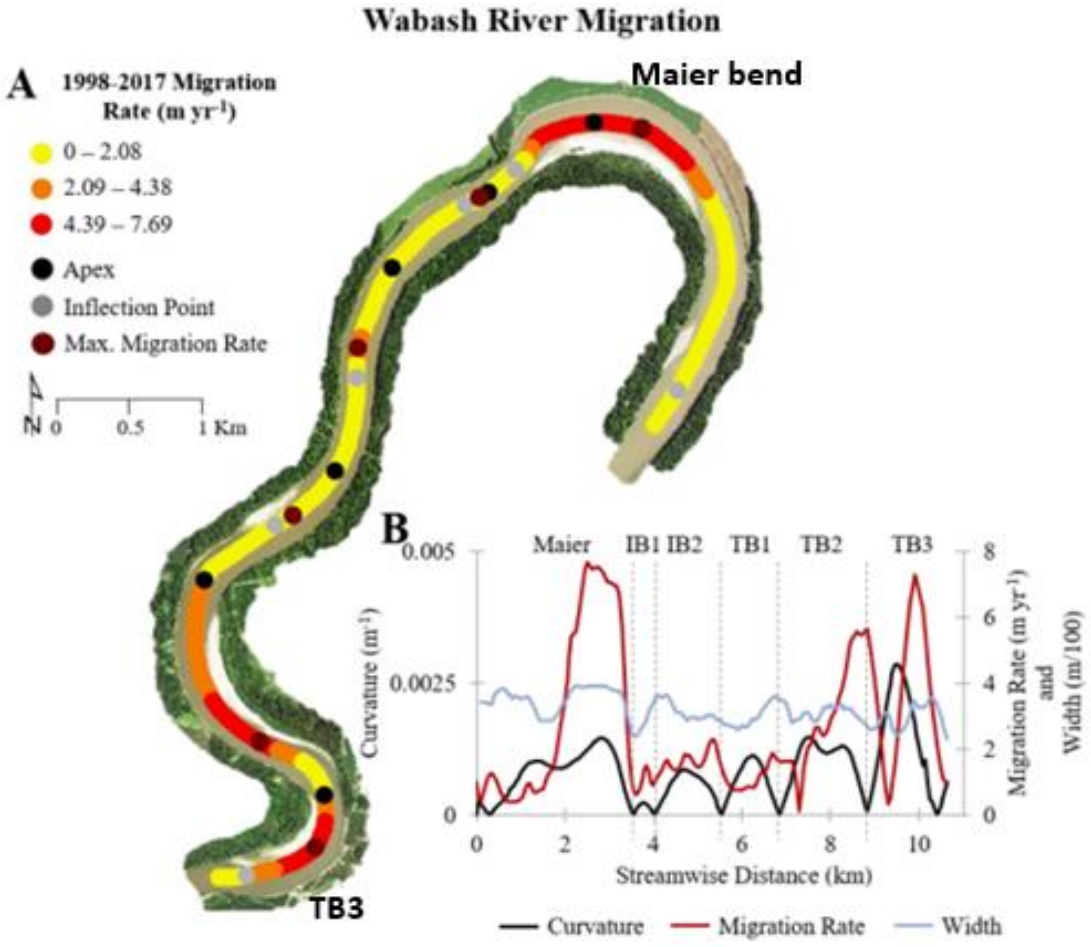

Figure 2.4: Migration rates along the 11km reach of the Wabash River. **A:** A map of classified migration rates through the reach at 50 m spacing with 2017 inflection and apex points, as well as point of maximum migration in each bend. **B:** 2017 curvature, migration rate, and width plotted where gray dashed lines indicate bends of interest separated at inflection points. Modified from Rowley, 2020.

Time period (Span)	Maier	IB1	IB2	TB1	TB2	TB3
(1) 1952 - 1998 *(46)*	4.04	0.38	0.93	2.45	3.19	0.89
(2) 1998 - 2011 *(13)*	4.5	0.31	0.61	1.68	3.19	4.61
(3) 2011 - 2017 *(6)*	3.52	0.51	1.33	0.67	2.27	4.27

Table 2.1: Migration rates (m yr^{-1}) for the six meander bends along the Wabash near Grayville, IL from 1952-2017. The locations of each of these bends are labeled in Figure 2.1. The two bends that are of interest in the present research are Maier Bend and TB3. From Rowley, 2020.

In order to calculate slopes for the Wabash River, Rowley (2020) extracted elevations from digital elevation models (DEMs) taken of the reach that were then converted to a mesh of points with the values in the longitudinal (S) and transverse (N) direction. The spacing for the points for the Wabash River were 50m in the S and 15m in the N direction (Rowley, 2020). Longitudinal elevation profiles were created along the S values at the centerline (S_{CL}) and 75m from the centerline (S_{75}) for the Wabash (Figure 2.5) to account for the transition from one side of the river to the other (Rowley, 2020). After the elevation profiles were extracted, Rowley (2020) calculated the slope using the first and last 250m of the point bars for S_{CL} and S_{75} and the elevation change along that distance (Table 2.2). For the present thesis, the slopes calculated for S_{75} are closer to the slopes seen in the GPR profiles that will be introduced later in this chapter and discussed thoroughly in chapter 3.

Rowley (2020) divided Maier Bend into two regions in her study (locations labeled in Figure 2.5) because the profiles act as if the sections were separate bars. $Maier_1$ is the gravel section of the upper bar. $Maier_2$ is the larger bar just downstream. For the present thesis, $Maier_2$ is the area of focus because this is the area surveyed by GPR. $Maier_2$'s longitudinal slope is low angle at 0.07° for S_{75} in the upstream section (Table 2.2). Towards the downstream end of $Maier_2$, the slope is -0.44° (Table 2.2; Rowley, 2020).

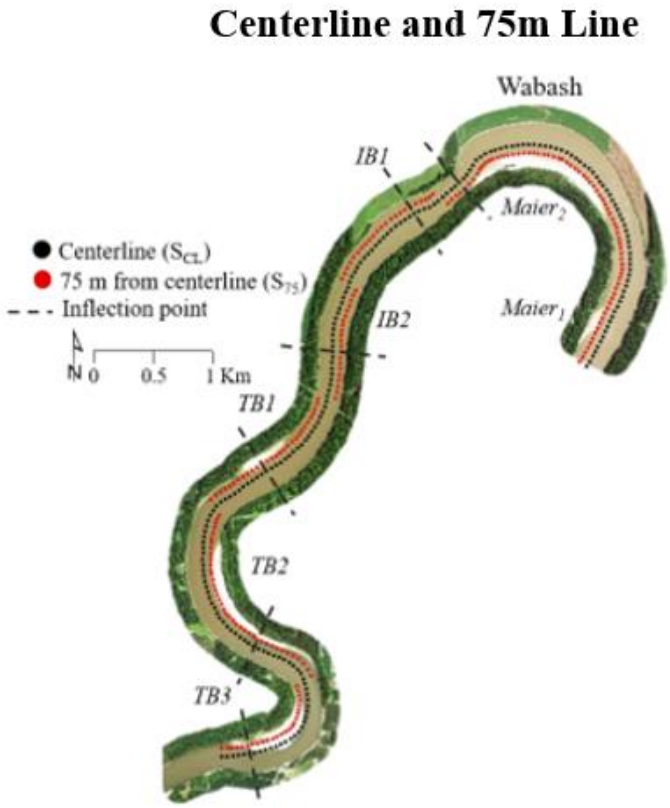

Figure 2.5: Centerline (S_{CL}) and 75m (S_{75}) inward position for extraction of elevation data along the Wabash River. Modified from Rowley, 2020.

	Bar Head		Bar Tail	
	Slope (°) at S_{CL}	Slope (°) at S_{75}	Slope (°) at S_{CL}	Slope (°) at S_{75}
Maier$_1$	-0.01	0.07	-0.16	-0.13
Maier$_2$	0.08	0.22	-0.01	-0.44
IB1	0.49	0.37	-0.28	-0.24
IB2	0.02	0.23	-0.28	-0.20
TB1	0.16	0.42	-0.17	-0.56
TB2	0.10	0.64	-0.27	-0.59
TB3	0.47	1.12	-0.42	-0.97

Table 2.2: Wabash River longitudinal slopes along the first and last 250m of the bar at S_{CL} and S_{75}. Maier$_1$ is the gravel section of the upper bar, and Maier$_2$ is the larger bar downstream of Maier$_1$. Locations of S_{CL} and S_{75} are shown in Figure 2.5. Highlighted on Table 2.2 are the two point bars of interest: Maier$_2$ and TB3. Modified from Rowley, 2020.

TB3 has the highest slope of 1.12° at S_{75} and at the bar tail, the slope is -0.97° (Table 2.2; Rowley, 2020). Slopes on the bar tail are greater along TB3 but are smaller for $Maier_2$. Additionally, the peak of the TB3 point bar occurs downstream of the apex (Figure 2.6). For the $Maier_2$ point bar, the peak (Figure 2.6) occurs upstream of the apex (Rowley, 2020).

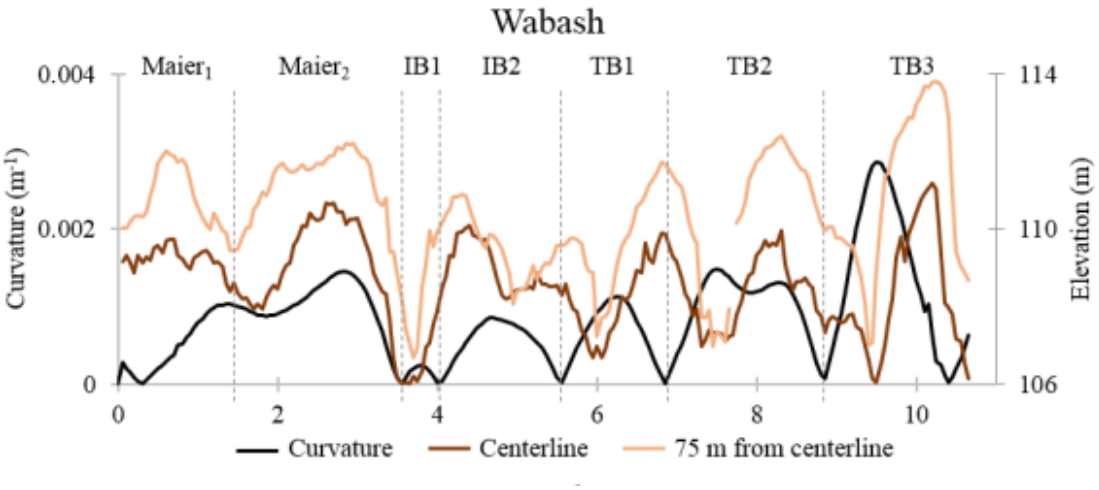

Figure 2.6: Longitudinal elevation profiles at the centerline and 75m inward from the centerline on the Wabash River (S_{CL} and S_{75}). $Maier_1$ is the gravel section of the upper bar (labeled on Figure 2.5). $Maier_2$ is the larger bar downstream of the upper bar (labeled on Figure 2.5). TB3 and $Maier_2$ bends are the focus of the present thesis. Modified from Rowley, 2020.

2.1.3 Flow

For Maier bend, depth-averaged velocity measurements were taken during two different flood events in the spring and summer of 2011 (Table 2.3; Konsoer et al., 2016a). The first set of measurements (labeled as Campaign 1 in Table 2.3) were taken on May 9-10, 2011, during a receding flood with a peak discharge of *c.*7650 m^3s^{-1} that reflects a recurrence interval (R.I.) of 15 years (Konsoer et al., 2016a). The discharge during the time of acquisition had substantial overbank flow (Konsoer et al., 2016a). The second set of measurements (Campaign 2 in Table 2.3) was obtained on June 28-29, 2011 when the Wabash River was near peak flow with a max discharge of *c.*2450m^3s^{-1} and an R.I. of 1.2 years (Konsoer et al., 2016a). This event was

approximately bankfull discharge for the lower Wabash River (Konsoer et al., 2016a). The three-dimensional flow velocity measurements were collected along pre-established cross-sections that were perpendicular to the channel centerline by using a boat-mounted Teledyne RDI 1200 kHz acoustic Doppler current profiler (ADCP) and the GPS was collected with an integrated Trimble dGPS antenna that was directly above the ADCP (Konsoer et al., 2016).

Site	Survey Campaign	Date	Q (m^3s^{-1})	Q_{av} (m^3s^{-1})	% Diff Q
Maier Bend	Campaign 1	May 9-10, 2011	6031-5805	5918	-3.75
	Campaign 2	June 28-29, 2011	2339-2398	2369	2.52

Table 2.3: Summary of hydrologic conditions during Konsoer et al. (2016a) field campaigns. *Q* is range of discharge, Q_{av} is average discharge for measurement campaign. Modified from Konsoer et al., 2016a.

Between the two campaigns of Konsoer et al. (2016a), the overall spatial patterns of the depth-averaged velocities were similar. In the upstream section of Maier Bend (cross-sections 135-141), the cross-stream pattern of depth-averaged velocities is highly asymmetrical. The highest velocities occurred near the inner bank and lowest velocities were adjacent to the outer bank (Figure 2.7; Konsoer et al., 2016a). At the bend apex (cross-sections 146-151; Figure 2.7), the maximum velocity shifts toward the outer bank and the cross-stream pattern of depth-averaged velocity becomes asymmetrical, with the highest velocities along the outer bank and lowest velocities over the point bar (Konsoer et al., 2016a). At the bedrock outcrop (cross-sections 152-153; Figure 2.8), flow is deflected away from the outer bank. However, flow velocities along this bank remain high above the bank platform (Konsoer et al., 2016a). Downstream of the bedrock outcrop (cross-section 154-156), the channel narrows and the depth-averaged velocities reach their highest values (>2ms^{-1}; Konsoer et al., 2016a). The zone of

maximum velocity in this section is relocated away from the outer bank as the channel widens downstream. At cross-sections 153 and 154 (Figures 2.7 and 2.8), the inward-directed secondary velocity shows that the bedrock platform and constriction of the channel immediately downstream causes the flow to be deflected away from the outer bank (Konsoer et al., 2016a). Downstream of the constriction (cross-section 155, Figures 2.7 and 2.8), there is a strong gradient in streamwise velocities that separates the core of the maximum velocity (~2.25ms^{-1}) from a zone of flow recirculation (Konsoer et al., 2016a). This is defined by negative (upstream) streamwise velocities (-0.35ms^{-1}; Konsoer et al., 2016a). Along the outer bank, outward secondary velocity vectors occur, and the flow expands toward the flow separation zone downstream of the constriction (cross-section 156; Figure 2.8; Konsoer, et al., 2016a).

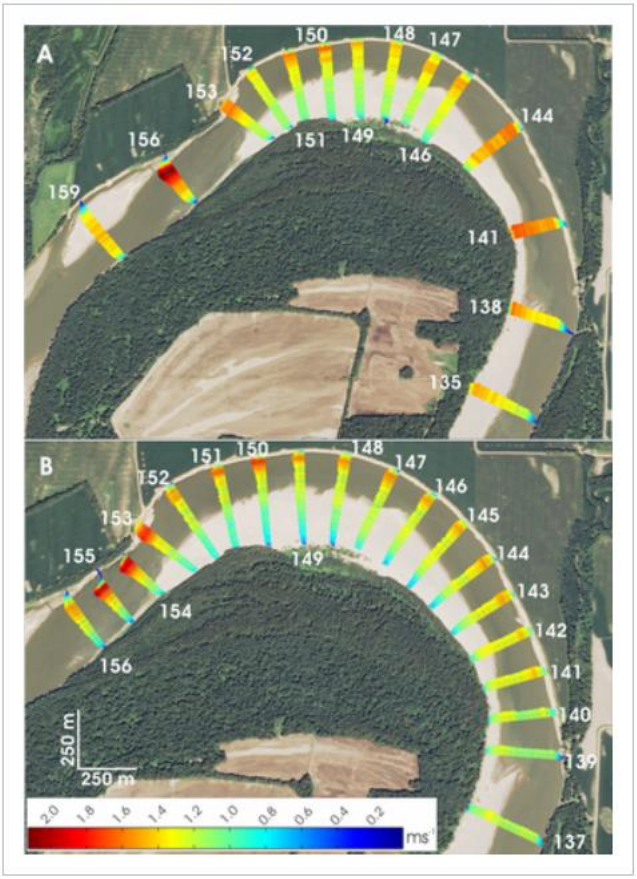

Figure 2.7: Depth-averaged velocity vectors along Maier Bend for (a) Campaign 1 (Q ~ 5660 m^3s^{-1}) and (b) Campaign 2 (Q ~ 2450 m^3s^{-1}). Campaign 2 was at nearly bankfull flow stage. From Konsoer et al., 2016a

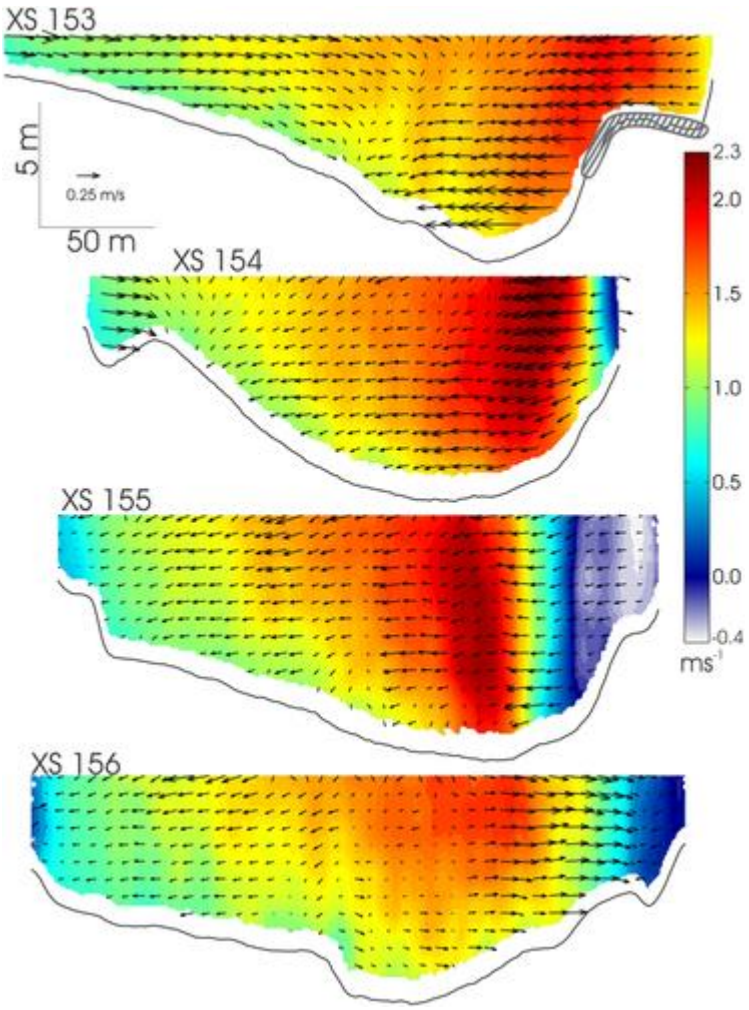

Figure 2.8: Cross-sectional flow fields at Maier Bend for June 2011 (Q ~ 2450 m^3s^{-1}), using a cross-section frame of reference, showing streamwise (contours) and transverse (vectors) velocities. Cross-section 153 shows bedrock platform exposed within the channel (grey-hatched region) directing flow away from the outer bank. Downstream of the bedrock, flow separation occurs, and a zone of recirculating fluid is present along the outer bank as shown by negative streamwise velocities. From Konsoer et al., 2016a

For TB3, depth-averaged flow velocities were measured in March 2018 also using an ADCP mounted to a boat similarly to the Konsoer et al. surveys taken in 2016 (Rowley, 2020). During the survey, the Wabash River was at a stage of 8.23m, had a discharge of 4049m^3s^{-1} (data was obtained from the USGS Mt. Carmel gauging station), and all of the point bar tops were submerged (Rowley, 2020).

In cross-sections 191-193 (Figures 2.9 and 2.10), velocities have higher magnitudes (up to 1.77ms^{-1}) along the inner (right) bank at the entrance to TB3 (Rowley, 2020). Velocities decrease as the channel widens (cross-sections 195-199) over the bar, but the high velocity core (HVC) maintains the same position along the outer banks with the velocities being 1.15-1.3ms^{-1}. Over the point bar, the lowest velocities are from 0.04-0.25ms^{-1} (Rowley, 2020). Some of the velocity vectors are oriented upstream (cross-sections 198-199; Rowley, 2020). The flow converges (cross-sections 200-201) as the channel narrows downstream of the bar tail, and the HVC increases in magnitude (1.75ms^{-1}) along the outer bank (Rowley, 2020). The magnitude of flow velocity is still asymmetrical (cross-section 203), but the HVC shifts toward the center of the channel and its highest velocity is 1.55ms^{-1} (Rowley, 2020).

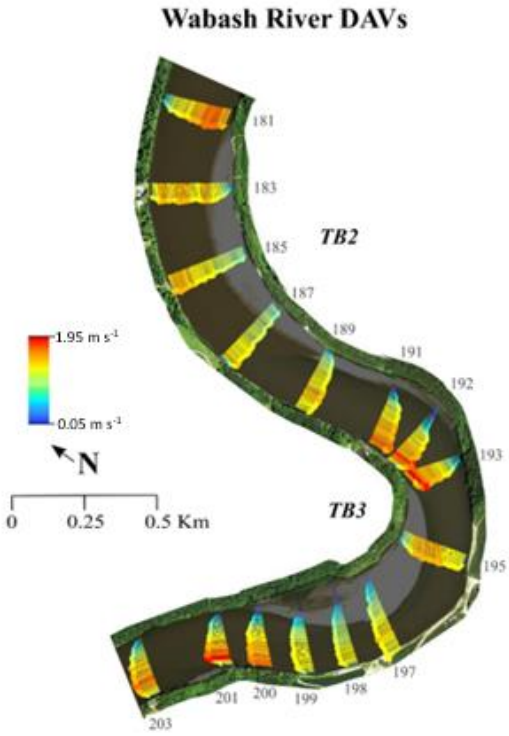

Figure 2.9: Depth-averaged velocities (DAVs) collected in 2018 along the Wabash River TB3 study reach. Arrows indicate direction of flow at each 3 m increments over the cross-section. Numbers indicate the cross-section. Modified from Rowley, 2020.

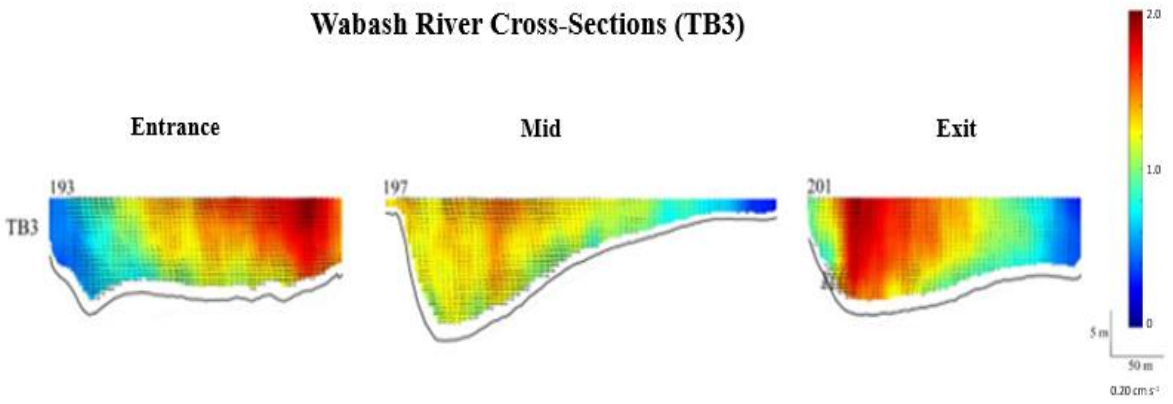

Figure 2.10: Cross-sections at the entrance, middle, and exit of each bend along TB3, Wabash River. Color indicates streamwise velocity magnitude and arrows indicates transverse velocity direction and magnitude. Modified from Rowley, 2020.

2.2 Aerial Imagery, Topographic Surveys, and Multibeam Echo Sounder Surveys

2.2.1 Aerial Imagery

Aerial imagery was collected from Planet and the National Agriculture Imagery Program (NAIP). The Planet imagery includes imagery from 2017 and 2018. The NAIP imagery for TB3 includes 1959, 1988, 2003-2009, 2011-2012, and 2014-2018, whereas for Maier Bend the NAIP imagery was for 1988, 2004, 2008, 2010-2012, and 2014-2018.

In order to show changes in these bends, the criteria of the imagery was based on whether they were georeferenced, show the bends at low flow, and that the imagery had good resolution (c. 3.7m for Planet image resolution and 5-6m ground resolution for NAIP). After applying these criteria, the images chosen for Maier were the NAIP imagery from 2004, 2008, 2011, 2012, 2016, and the Planetscope imagery from 2018. For TB3, the images that met the criteria were from NAIP 2004, 2005, 2007-2009, 2011, 2012, 2015, 2016, and 2018. Once the images were chosen, the point bars and cut banks were digitized manually and overlain on the latest image to show how much the point bar has migrated and how much the cutbank has eroded.

2.2.2 Topographic Surveys

For the 2017 GPR data in the present study, GPS coordinates using an RTK-GNSS were taken along different points of the GPR survey and then applied to the data to correct for the topography. For the 2018 GPR data in this study, the GPR employed an inbuilt GPS, which automatically accounted for changes in topography along the survey lines (Rowley, 2020). An example of topographic correction is applied to image C in Figure 2.21.

2.2.3 Multibeam Echo Sounder Surveys (MBES)

For the present thesis, Multibeam Echo Sounder Surveys (MBES) were collected by Dr. Kory Konsoer (Louisiana State University) in 2019 to characterize bed elevation along the point bars. MBES surveys are typically collected at bankfull flood stage in order to be able to measure the morphology of the entire channel (Rowley et al., 2021). MBES uses a transducer that is mounted to a boat to send out multiple, simultaneous sonar beams in a fan-shape and then as the sonar beams reflect back, the depth can be calculated based on the time it takes for the sonar beams two-way travel time and knowing the speed of sound in water (Konsoer et al., 2016a; Rowley et al., 2021). The data is collected as a point cloud (a group of data points), but the point cloud data was exported as an ASCII file to a GIS platform and converted to a digital elevation model (DEM; Rowley et al., 2021). Any sections of the river that could not be reached by boat due to the water being too shallow were supplemented with structure from motion elevation data (Rowley et al., 2021). This data was then used for the current thesis to measure the longitudinal and transverse slopes of the point bars. Additionally, the MBES data was also used to support the interpretations of bedforms from GPR data.

2.3 GPR Overview

2.3.1 Principles of GPR

GPR is a shallow, nondestructive geophysical method used to map the subsurface, by using electromagnetic (EM) pulses that are transmitted into the ground by a transmitter (labeled as 2 in Figure 2.11) and reflected to a receiver (labeled as 3 in Figure 2.11) to be stored as digital data (Neal, 2004).

Figure 2.11: Basic GPR setup: 1) controller; 2) transmitter; 3) receiver; 4) Encoder wheel **f**or measuring distance; 5) GPS. Edited Image from Sensors and Software (2021).

Figure 2.12 illustrates a basic GPR survey arrangement, demonstrating how an EM wave is reflected in the subsurface. As the EM signal propagates through the ground, if the dielectric property (the ability of a material to transmit electrical currents) of the ground material changes, this changes the velocity of the EM signal (Neal, 2004). When the velocity of the signal

changes, some of the energy is reflected and scattered, and travels back to the surface. These reflections are captured by the receiver and then stored as data. The energy that is not reflected at the interface is refracted through the interface into the material below, and continues to travel downward until it encounters another interface with different dielectric properties. The energy thus reflects/scatters at subsequent interfaces and returns to the surface. This continues until the signal dissipates with depth (Baker et al., 2007). Once the data is collected, it can then be processed to produce a 2-D radar profile (Figure 2.14; Neal, 2004).

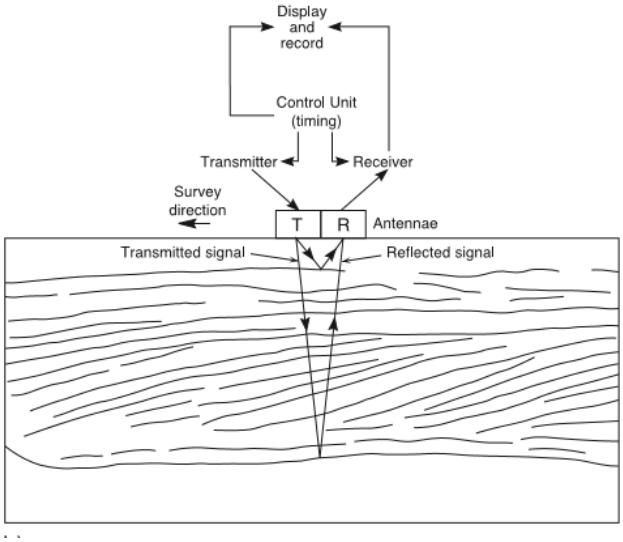

Figure 2.12: Example of a GPR survey. A GPR consists of a transmitter (T) and receiver (R). The survey direction moves to the left as the transmitter sends an EM wave into the material. If the dielectric property of the material changes, the signal is reflected to the receiver, where the data is then recorded and stored. From Neal, 2004.

Four main configurations are used in reflection surveys: common off-set, common midpoint (common depth point), common source, and common receiver. However, for this thesis, common off-set and common midpoint are the only two arrays that will be relevant. Common off-set is most typically used for GPR surveys (Neal, 2004) and usually consists of either a single transmitting and receiving antenna (monostatic) or two, separate transmitting and receiving antenna (bistatic) (Baker et al., 2007). When the transmitter and receiver are separate,

there is a fixed distance between them, and the two antenna are orientated in the same direction and perpendicular to the survey line. The transmitter and receiver are typically mounted on a cart that moves along the survey line and the EM signals are transmitted into the ground as the cart moves, with the receiver capturing the reflections of each interface. In offset surveys, instead of transmitting the EM signal directly downward, the signal is transmitted at an angle and then captured by the receiver at an angle (Figure 2.13).

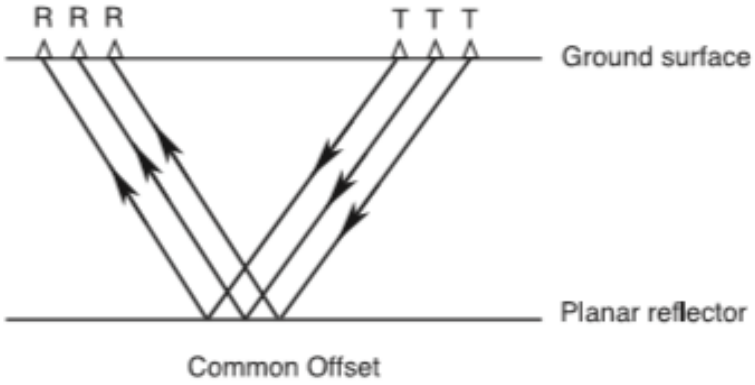

Figure 2.13: Example of a common off-set survey that is most commonly used for GPR surveys. The transmitter (T) and receiver (R) are at a fixed distance from each other. From Neal, 2004.

During a common off-set survey, the distance that has been surveyed can be determined one of several ways. One method is when horizontal distances are collected on a time-base (Neal, 2004). These time-base measurements can be converted to a distance-base measurement through manual marking (Neal, 2004). Another method is the step-wise method where the antennae are moved in steps along the line while maintaining a separation distance between the transmitter and receiver (Neal, 2004). The step-wise method allows for more coherent and higher amplitude reflections because the antennae are stationary when the data is collected (Neal, 2004). These two methods are only used when the transmitter and receiver are being moved without a cart. For this thesis, the transmitter and receiver were moved on the cart shown in Figure 2.11.

On this cart, there is a pedometer attached on the right rear wheel that helps keep track of the distance that the cart travels and can be supported by GPS measurements.

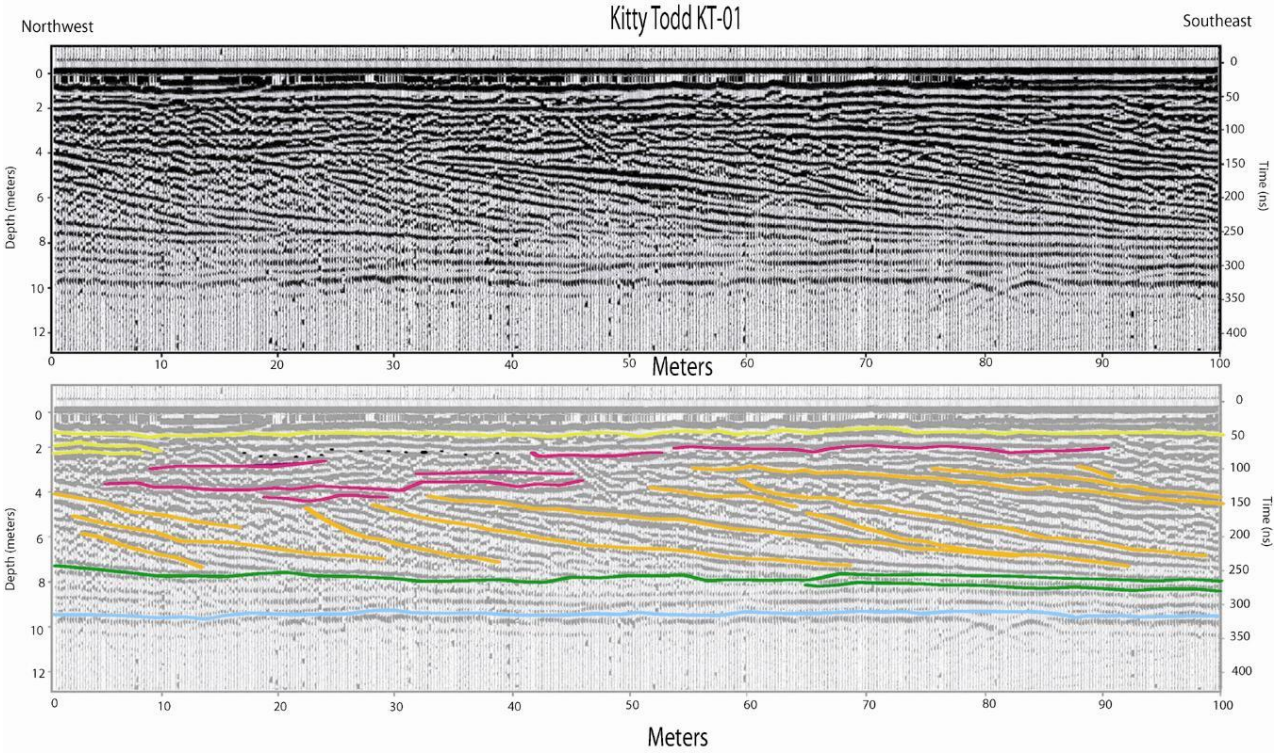

Figure 2.14: Example of a GPR 2-D radar profile of the subsurface. The bottom image includes an interpretation of the different layers in the subsurface. The x-axis shows the distance of the survey in meters, and the y-axis represents the two-way travel time, as also converted to vertical distance here. From Stierman et al., 2005.

While the survey is recorded, horizontally sequential reflection traces form a radar reflection profile (Figure 2.14). The x-axis of the radar profile is the horizontal distance, and the y-axis represents the two-way travel time (TWT), which is measured in nanoseconds. The TWT is a function of depth, the spacing between the transmitter and receiver, and the radar wave velocity within the overlying material (Neal, 2004).

Common midpoint (CMP) or common depth point arrays are also used for GPR surveys, but less frequently than common off-set. However, CMP surveys are useful for determining the velocity at which the EM waves travel through the subsurface material if a flat reflector is present. In CMP surveys, the transmitter and receiver are progressively moved greater distances

apart (Figure 2.15; Neal, 2004). CMP surveys result in an increase in TWT collected and are used to calculate average radar-wave velocities to a given reflection (Neal, 2004). After the average velocities are determined, the TWT can be converted to depth estimates (Neal, 2004).

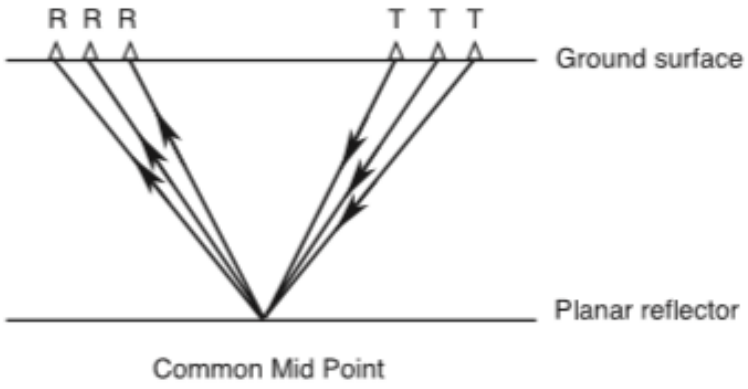

Figure 2.15: Common mid-point or common depth point array. All the reflections share a common point of depth. From Neal, 2004.

For the present research, common midpoint surveys were not collected. Therefore, in order to determine the depth of the surveys, another method had to be applied. During processing of the GPR profiles, the hyperbole that are indicators of point reflectors (buried objects or large clasts) in the study area were measured with a tool in Ekko Project V5. By measuring the slope of the hyperbole, they can be used to determine the velocity that the signal moves through the subsurface and as a result, the depth can be calculated. After determining the velocities based on the hyperbola for the GPR profiles, an average velocity (0.093m/ns for Maier Bend and 0.080 m/ns for TB3) was taken for each point bar in the bends. Then this average velocity was then used to determine the depth of each of the 2-D GPR profiles.

2.3.2 Determining Depth and Resolution in GPR Surveys

The depth and resolution of the radar profile are dependent on the subsurface material and the frequency of the GPR antenna (Neal, 2004). Since GPR functions in the electrical

conduction wavelength of the electromagnetic spectrum, it responds to electromagnetic properties of the subsurface materials. These properties include the dielectric permittivity, magnetic permittivity, and electrical conductivity (Neal, 2004). Dielectric permittivity is a function that has both real and imaginary components. The real component is the dielectric constant, which is the ratio of the electric-field storage capacity of a material or how much a type of material can store an electrical field to that of the total area (Neal, 2004). The imaginary portion is known as dielectric loss that accounts for attenuation and dispersion. The dielectric constant is important because it controls: i) the velocity of the EM waves through the material, ii) the imaging resolution, both vertically and horizontally, and iii) the reflection coefficients at the interfaces (Neal, 2004). The dielectric constants of different materials determine the velocity of the EM wave, with different materials possessing different bulk dielectric constants, (Table 2.4 Martinez and Byrnes, 2001; Neal, 2004).

The magnetic permeability is the magnetic field divided by the magnetic field strength and is the product of the permeability of free space and relative magnetic permeability (Martinez and Byrnes, 2001). The effect that magnetic permeability exerts on GPR is negligible for materials with a relative magnetic permeability of m_r=1 (Martinez and Byrnes, 2001). This value for relative magnetic permeability is common for materials such as sediment (Martinez and Byrnes, 2001).

Electrical conductivity is the scale at which a material conducts electricity, or the ratio of the current density in the material to the electric field that causes the flow of the current (Martinez and Byrnes, 2001). Together, these three factors are reliant on the wave frequency. The dielectric constant decreases with an increase in the frequency while the dielectric loss increases (Martinez and Byrnes, 2001). However, the behavior of those three factors are more

consistent when the GPR antenna frequency is between 25-1500MHz (Martinez and Byrnes, 2001).

Material	ε_r (Davis and Annan, 1989)	ε_r (Daniels , 1996)
Air	1	1
Distilled water	80	
Fresh water	80	81
Sea water	80	
Fresh water ice	3–4	4
Sea water ice		4–8
Snow		8–12
Permafrost		4–8
Sand, dry	3–5	4–6
Sand, wet	20–30	10–30
Sandstone, dry		2–3
Sandstone, wet		5–10
Limestone	4–8	
Limestone, dry		7
Limestone wet		8
Shales	5–15	
Shale, wet		6–9
Silts	5–30	
Clays	5–40	
Clay, dry		2–6
Clay, wet		15–40
Soil, sandy dry		4–6
Soil, sandy wet		15–30
Soil, loamy dry		4–6
Soil, loamy wet		10–20
Soil, clayey dry		4–6
Soil, clayey wet		10–15
Coal, dry		3.5
Coal, wet		8
Granite	4–6	
Granite, dry		5
Granite, wet		7
Salt, dry	5–6	4–7

Table 2.4: Dielectric constants of common earth materials (measured at 100 Hz). From Martinez and Byrnes, 2001.

Frequency also greatly affects the resolution of the GPR profile, and it is key is to optimize the frequency to obtain the tradeoff between signal resolution and depth of penetration for the subsurface features being imaged. If the frequency is high, a higher resolution is obtained, but the signal cannot propagate very deep. If a low frequency is used, the signal penetration is greater, but the resolution will be lower (Woodward et al., 2003). In order to select the correct frequency, it is important to consider factors such as the subsurface material and antenna size. When considering the subsurface material, electrical conductivity is an important factor to consider because it will determine how far the EM signal will transmit

through the material. If the conductivity of the material is higher, the EM waves will be absorbed into the material more easily (Daniels, 2009). The size of the antenna also determines frequency, with the rule of thumb being that the width of the antenna is about half of the wavelength (Utsi, 2017). The equation to determine the best antenna frequency to use for a survey is:

$$\lambda = V/f ,$$

where λ is wavelength, V is velocity that the wave moves through the material, and f is the frequency of the antenna (Robinson et al., 2013).

2.3.3 Issues and Limitations with GPR

Before the GPR data is processed, there are inherent issues and limitations that can affect data quality. One of these issues is time-zero drift that occurs when the airwave changes position in different traces (Neal, 2004). This results in misalignment of not only the air and ground waves, but also the primary and secondary reflections beneath it (Neal, 2004). The air wave is the EM signal that goes directly from the transmitter to the receiver and never touches the ground (Figure 2.16; Blindow, 2007). The ground wave is the EM signal that moves from the transmitter, moves along the surface of the ground, then reflects towards the receiver (Figure 2.16; Blindow, 2007). This error occurs typically when the electronics of the system are warmer or colder than the surrounding temperature. It can also be a result of damaged cables (Neal, 2004).

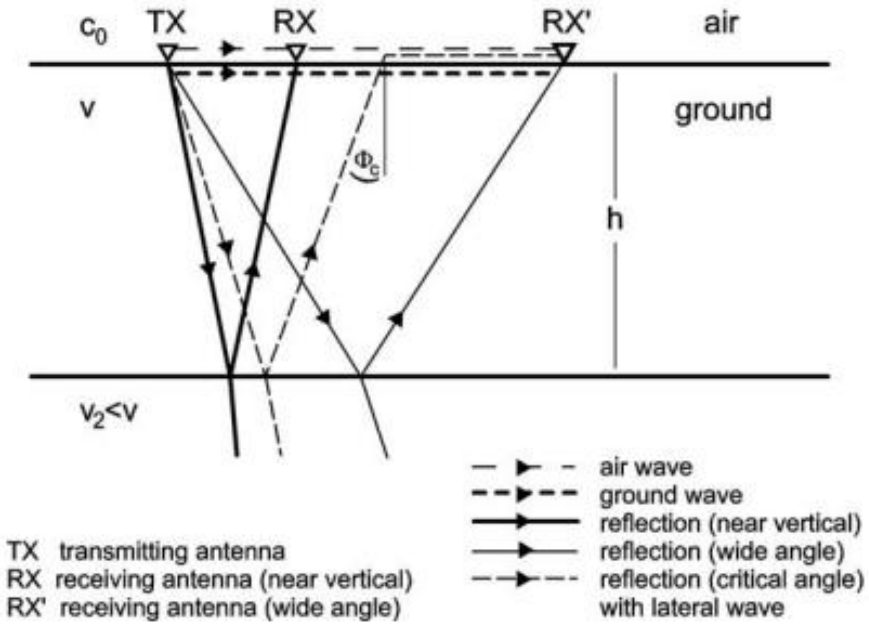

Figure 2.16: GPR ray paths for the horizontal two-layer case, displaying an example of how ground waves and air waves move in relation to the transmitting antenna and receiver. From Blindow, 2007.

Another inherent limitation occurs during common off-set surveys. Since the antenna are not coincident, image distortion will occur because the reflection travel times will be too long with respect to depth of the reflector that created the reflection (Figure 2.17; Neal, 2004). In other words, as a consequence of antenna separation, the reflections appear at a greater depth than their true (zero-offset) location the farther apart the antenna are set (Neal, 2004). The difference between the travel time at a given offset and at zero offset is known as normal moveout. Its effect decreases as the travel time or depth increases because the TWT approaches, but never quite reaches, zero-offset time (Neal, 2004). However, if there are velocity variations or dips in the reflections, it does make the issue more complex (Neal, 2004).

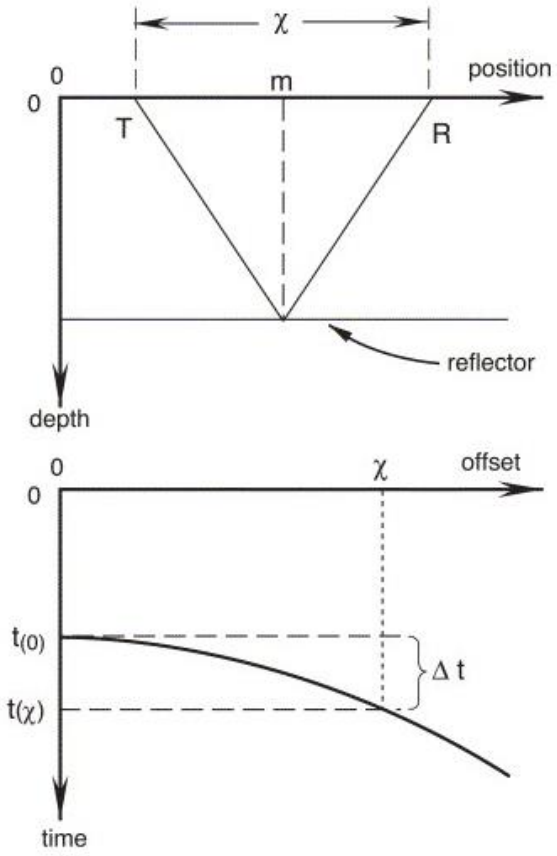

Figure 2.17: Normal moveout resulting from a separation (represented by *x*) between the transmitter (T) and the receiver (R). The time $t_{(x)}$ for a reflection with a transmitter-receiver separation *x* is larger (by Δt) than $t_{(0)}$ which would be seen at zero offset (i.e. if the antennae were coincident). As the antenna separation increases, the reflection from the horizontal reflector displays a hyperbolic moveout. From Neal, 2004.

Signal saturation can also cause problems with the data profiles and occurs when the receiver becomes signal saturated because there is too short a time between transmitter shots during surveying. In this situation, there is a large amount of energy contributed from the airwave, ground wave, and near-surface reflections. As a result, a low frequency signal is produced and is superimposed on the higher frequency reflections (Neal, 2004).

The depth to which the EM wave penetrates is an issue or limitation was discussed above. As the EM wave propagates through the subsurface material, attenuation and energy loss occurs (Neal, 2004), with the amount of loss and the depth to which the EM wave propagates dependent on the signal frequency and the subsurface material (Martinez and

Byrnes, 2001). When conducting a GPR survey, it must be decided what balance of penetration depth or resolution are required with respect to the features of interest within the materials and aims of the GPR survey.

Vertical and horizontal resolution are two important factors that affect the raw GPR data. Vertical data resolution determines the position of reflectors in space or time, and as discussed above as frequency increases then the vertical resolution increases, but the depth to which the EM waves penetrate decreases (Neal, 2004).

Horizontal resolution is controlled by the width of the first Fresnel zone, which is a function of wavelength and depth to a given reflector (Figure 2.18; Neal, 2004). As the EM wave moves deeper, horizontal resolution decreases. Horizontal resolution is important within sedimentary research because if the horizontal resolution decreases with depth, stratification in lower layers may not be visible (Neal, 2004).

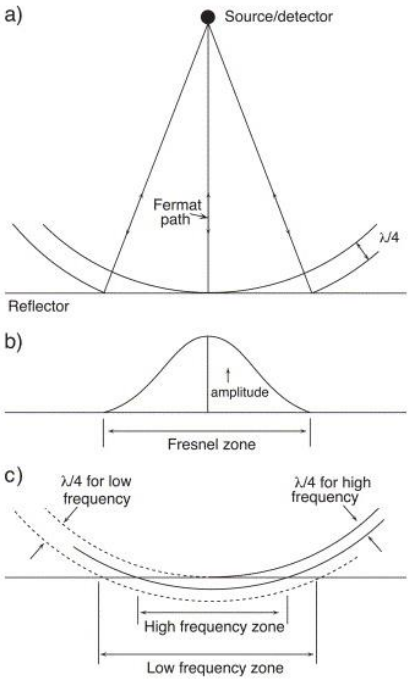

Figure 2.18: Horizontal resolution as determined by Fresnel zone width:

A: Electromagnetic waves propagate through the ground in an ever-expanding cone, with the cone's apex at the transmitting antenna. All reflections within one-quarter of the dominant wavelength will interfere constructively to form a single reflection.

B: Waves closest to the Fermat path contribute most to a reflection's amplitude.

C: Fresnel-zone width is a function of reflector depth and frequency-dependent wavelength. The higher the frequency (and shorter the wavelength) the higher the horizontal resolution.

From Neal, 2004.

Since the reflections are recorded as a 2-D profile, a series of issues also occur because these reflections are not directly beneath the survey point. The antennae transmit and receive EM energy in a complex 3-D cone, and therefore a reflection on a trace can come from anywhere on the radar wave front (Neal, 2004). This issue causes several different effects. First, down-dip reflectors can appear to be shallower than they actually are (Fig. 2.19; Neal, 2004).

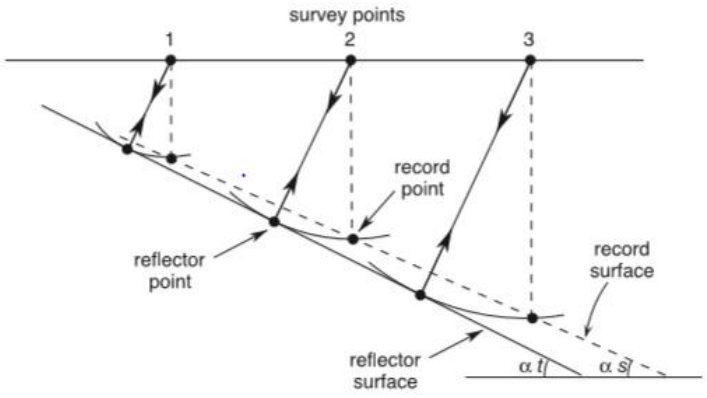

Figure 2.19: Example of the recorded down-dip compared to the actual down-dip. α_s is the dip of the record surface. α_t is the true dip of the reflector. From Neal, 2004.

Secondly, objects that are perpendicular to the survey line, or rounded objects that are large in respect to wavelength, act as isolated reflector points and can create hyperbolic-shaped diffractions (Figures 2.20 & 2.21) that obscure primary reflections (Neal, 2004). These objects can be anything from human-made materials like pipes and cables to objects found in nature such as sedimentary clasts or tree branches. Diffractions can also be caused in fluvial sediments by lateral truncation of heterogeneities (Neal, 2004).

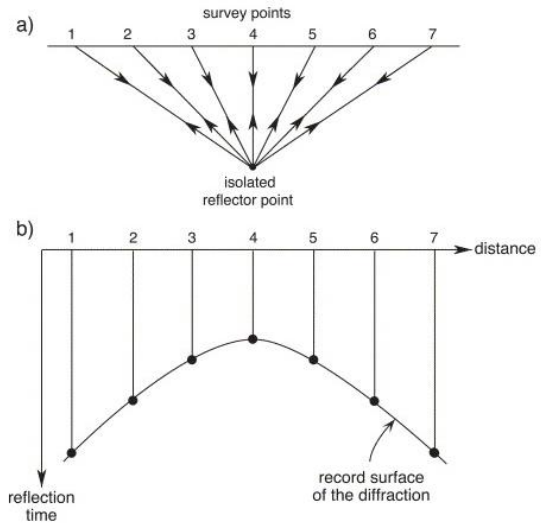

Figure 2.20: Formation of a diffraction on an unmigrated reflection profile from an isolated reflector point.

A: Reflection paths to and from a point reflector at survey points 1-7.

B: Diffraction on the resulting unmigrated radar reflection profile. This is caused by mapping record points that are directly beneath each survey point.

From Neal, 2004

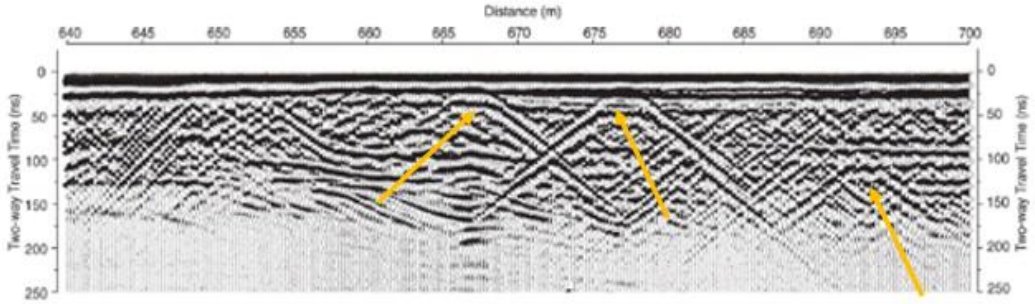

Figure 2.21: Example 2-D GPR profile showing hyperbola (marked by yellow arrows) caused by buried objects. This example is an unmigrated 100 MHz radar reflection profile showing a complex sequence of cross-cutting diffractions. These have resulted from communication cables and pipes (associated with a sprinkler system) both buried in the shallow subsurface (ca. 1 m) at the Royal Birkdale Golf Club, Sefton, northwest England. Modified from Neal, 2004.

Lastly, when concave-up, curved bedding is present (i.e. trough cross-bedding), its ability to be imaged in unprocessed data will be dependent on its relationship to wave front curvature (Neal, 2004). If the bedding curvature exceeds the wave front curvature, then the recorded surface pattern will look like a bow-tie pattern (Figure 2.22), making the identification of curved subsurface features difficult (Neal, 2004). This is because the reflections originate from at least three discrete reflector points.

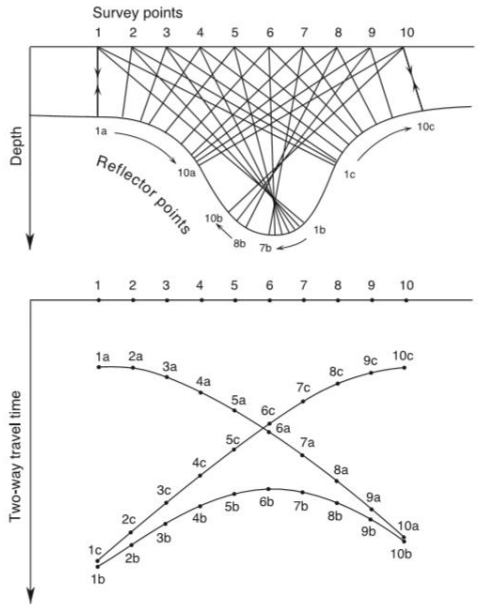

Figure 2.22: The top image shows the reflections hitting a curved feature in the subsurface. The bottom image shows the "bow-tie" feature caused by three curved record surfaces. From Neal, 2004.

GPR surveys not only encounter issues from the subsurface, but also from outside sources such as FM radio transmitters, cell phones and their transmission towers, and other types of radio communication. These external sources of noise affect the individual traces in the reflection profile. Noise can also occur in profiles where there are multiple reflection events that obscure the primary reflections. This is called "ringing" and has multiple potential causes, primarily due to radar signals bouncing back and forth between a highly-conductive reflector (Neal, 2004).

Furthermore, GPR can also be compromised by surface reflections, where the electromagnetic energy from the GPR antenna in the air bounces off of objects with high electrical contrast (Neal, 2004). Part of the signal is then reflected and detected by the receiver. Common causes of the surface reflections are power lines, trees, large boulders, and metallic fences. Since GPR is recorded on a time basis, changes in surface topography are not taken into account (Neal, 2004). This can lead to major distortions in the subsurface image if

not corrected (Neal, 2004). Figure 2.23 shows an example of this distortion by illustrating a broad diffraction caused by a large dune hillock adjacent to the survey line.

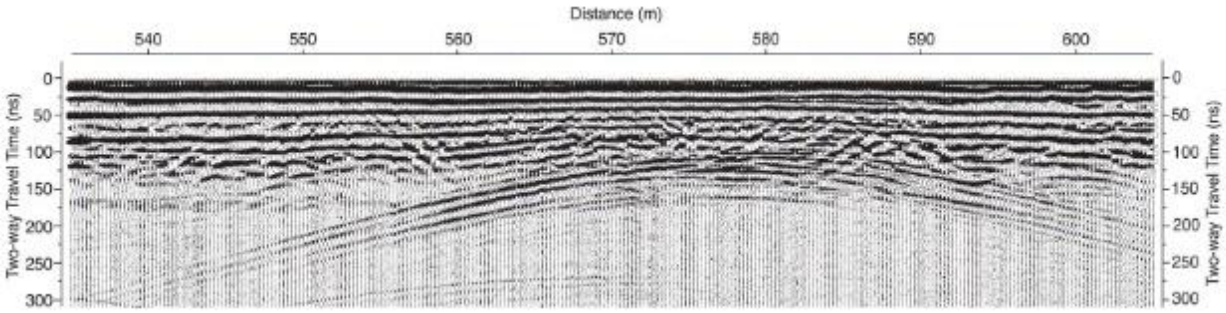

Figure 2.23: Example of surface reflection. Broad diffraction beneath two-way travel time of 100ns across the whole profile shown above. This example was caused by a large dune hillock adjacent to the **transect line** on the Hillside Golf Club, Sefton, northwest England. No migration has been applied to this profile, but AGC gain was applied. From Neal, 2004.

A different limitation that is seen is vertical and lateral variation in the subsurface materials (Neal, 2004). Since GPR is recorded on a fixed time base, depths can only be approximated on a radar profile if the velocities of the radar wave are known. If the layers in the subsurface are relatively heterogeneous, then the depth is simple to determine with a linear conversion from the TWT (Neal, 2004). However, if there is much variation in the subsurface between layers, then the radar profile will become distorted (Neal, 2004). For sedimentary environments, this issue is encountered when radar waves reach the water table (Neal, 2004). As radar waves move through the water table and saturated sediment, the waves slow down. This results in the depth scale on the GPR profile having to expand to take account of the velocity of the radar waves slowing down (Neal, 2004). Additionally, the profile becomes distorted visually (e.g. reflection dips appear to increase below the water table; Neal, 2004).

2.3.4 GPR Data Collection

For the present study, GPR surveys were conducted in 2017 and 2018 using a PulseEkko Pro SmartCart GPR unit (similar to the system shown in Figure 2.11) with 100

MHz antennae. The survey lines were taken along predetermined transects that were roughly perpendicular to the river centerline. The spacing between these transects was roughly 200-300 m. In addition to the perpendicular transects, three longitudinal transects were also collected parallel to the river centerline (Rowley, 2020). The depth of penetration was calculated using an average velocity calculated from using hyperbola within the transects as known depth points.

2.3.5 Data Processing

Despite the issues and limitations discussed above, there are methods to either take them into account and/or correct them to create an improved radar profile. Some of these issues require action to take place at the study site, but others that can be implemented later during data processing. GPR data from each transect were post-processed herein using Ekko Project V5.

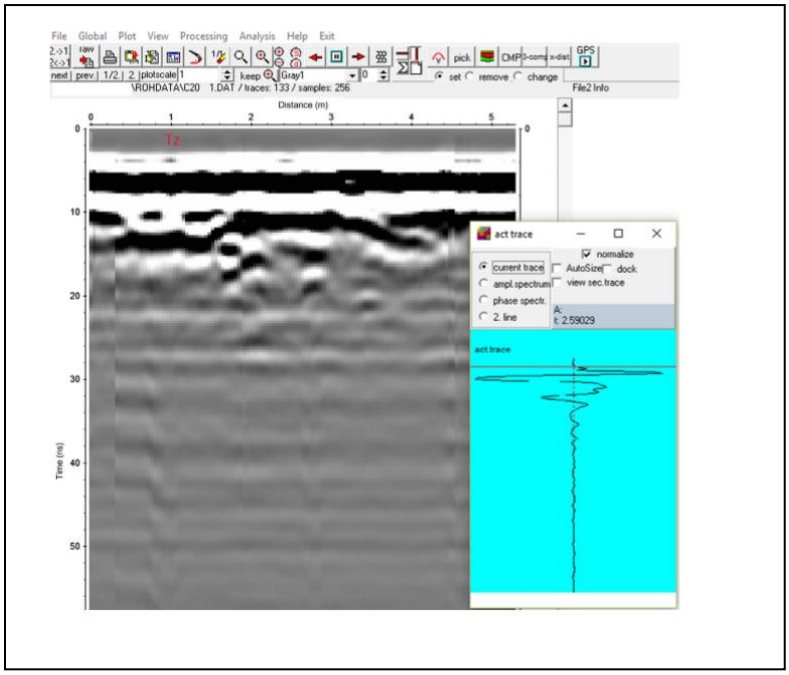

Figure 2.24: Example of correcting for the Tzero by using an individual wiggle trace. From Utsi, 2017.

Before processing the rest of the data, the time zero drift (Tzero) must first be corrected, which can be accomplished in two ways. Depending on the GPR system, this drift can be automatically corrected for as the data is collected, manually corrected in the operating software, or corrected using processing software after the data has been collected (Figure 2.24). For the GPR system used for the present thesis, Tzero drift was automatically corrected for during collection (Sensors and Software, 2018).

To correct for high saturation, a 'dewow' filter can be applied after the data has been collected (Neal, 2004). This filter is a high-pass filter that allows for the spectral peak for the specific antenna center-frequency to pass with fidelity, while suppressing the low-frequency 'wow' noise (Neal, 2004). Care is required as this method can sometimes create two artifacts: an artifact as a precursor to the first break (creates a false starting point on the GPR trace), and another artifact when the signal exceeds the clipping level of the electronics that causes large, blank areas in the trace (i.e. leaves behind large blank spaces on the profile after the 'dewow' has been applied; Neal, 2004).

The EM signal weakens as depth increases due to signal being lost due to attenuation with depth, or after being reflected back to the receiver. To compensate for the loss of signal, gain can be applied in post-processing to strengthen the weaker signal at depth (Utsi, 2017). The gain that is applied to data is typically called "time-based" or 'time-varying" gain (Utsi, 2017). There are several types of gain that can be applied to GPR data including the following: constant gain, exponential gain, exponential gain compensation (SEC), and automatic gain control (AGC; Robinson et al., 2013). The two most popular types of gain that are used in processing are SEC and AGC. SEC (Panel A, Figure 2.25) is a combination of a linear time gain and an exponential time gain and attempts to compensate for the exponential ohmic

dissipation of energy (Sensors and Software, 2018). AGC gain (Panel B, Figure 2.25) aims to equalize the amplitudes of all GPR signals by applying a gain that is inversely proportional to the signal strength (Sensors and Software, 2018). AGC gain is the best type of gain for defining the continuity of reflections (Sensors and Software, 2018).

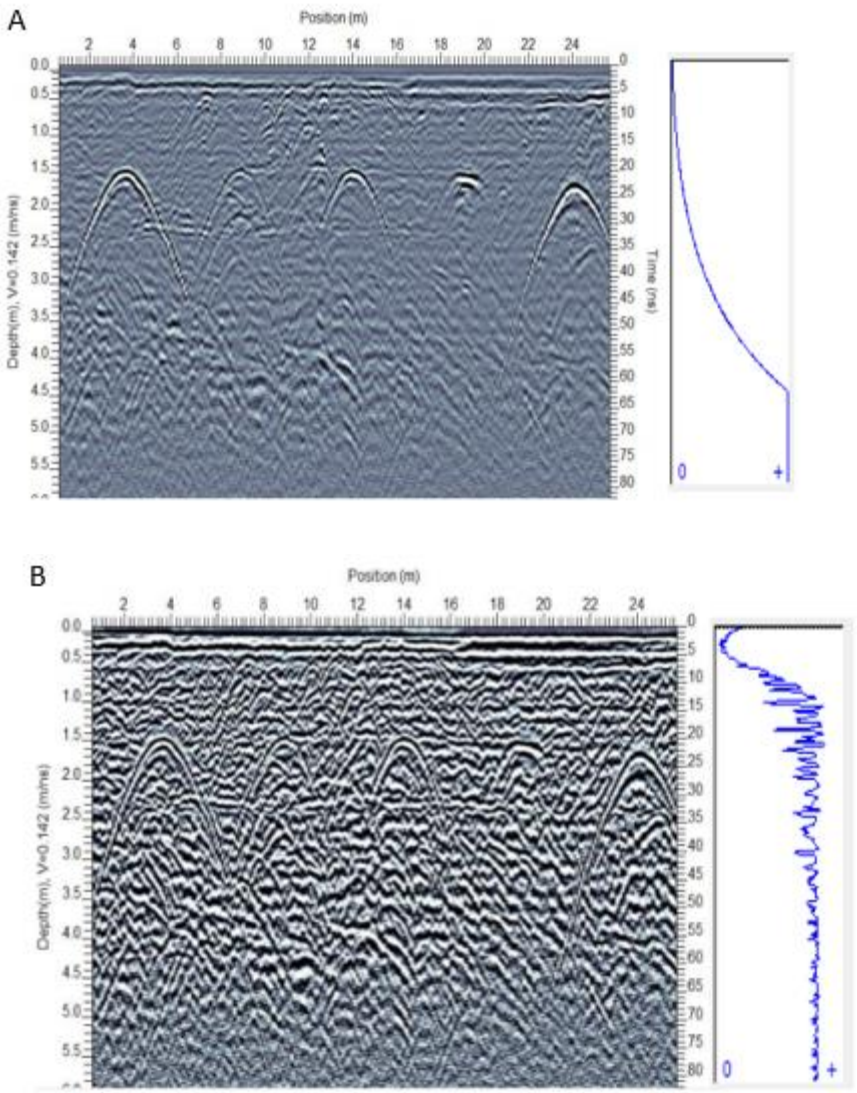

Figure 2.25: Examples of gain being applied to GPR profiles**. A:** GPR profile with SEC gain applied and an SEC gain function on the right. This type of gain is the closest to reality because it compensates for the attenuation of the signal with depth**. B:** GPR profile with AGC gain applied with the AGC gain function shown on the right. AGC applies a gain inverse to the signal strength. The gain for this function varies for each trace. Modified from Sensors and Software, 2018.

The goal of applying gain is to allow all of the targets to be visible without increasing the noise too much in the profile. One method that can be used to apply gain is to observe the effect of gain on an individual trace, and then increase the gain until the target is more visible before the very lowest part of the signal rises to an unlikely level (Utsi, 2017).

Another method that is useful in data processing is known as trace stacking and involves averaging multiple GPR traces to improve the signal to noise ratio, and thus creating a clearer profile. Stacking is used to reduce noise and make the targets clearer but stacking of too many traces can reduce the detail visible. In certain systems, stacking is offered as an option during data collection, but it is often applied in post-processing (Utsi, 2017).

In order to obtain an approximate depth of features in a profile by converting the TWT to depth, information is needed regarding the subsurface-radar-wave velocity. There are several ways to estimate this velocity. One option is using the TWT to a reflection interface, or a buried object, that is at a known depth. Another is to use direct laboratory measurements of your field samples, although this method is difficult due to sampling and also remove the sample from its environment. A third method uses the travel time between two wells using borehole radar (Neal, 2004). For the current thesis, depth was approximated by using a tool in EKKO Project (a GPR processing software by Sensors and Software). This tool (Figure 2.26) measures the size of hyperbola within the GPR profiles and then calculates a velocity. An average of all the velocities calculated from each GPR profiles for a specific point bar was calculated, and this average velocity was then applied to all the profiles for a single point bar. Thus, all the depth approximations were based on the same velocity measurement.

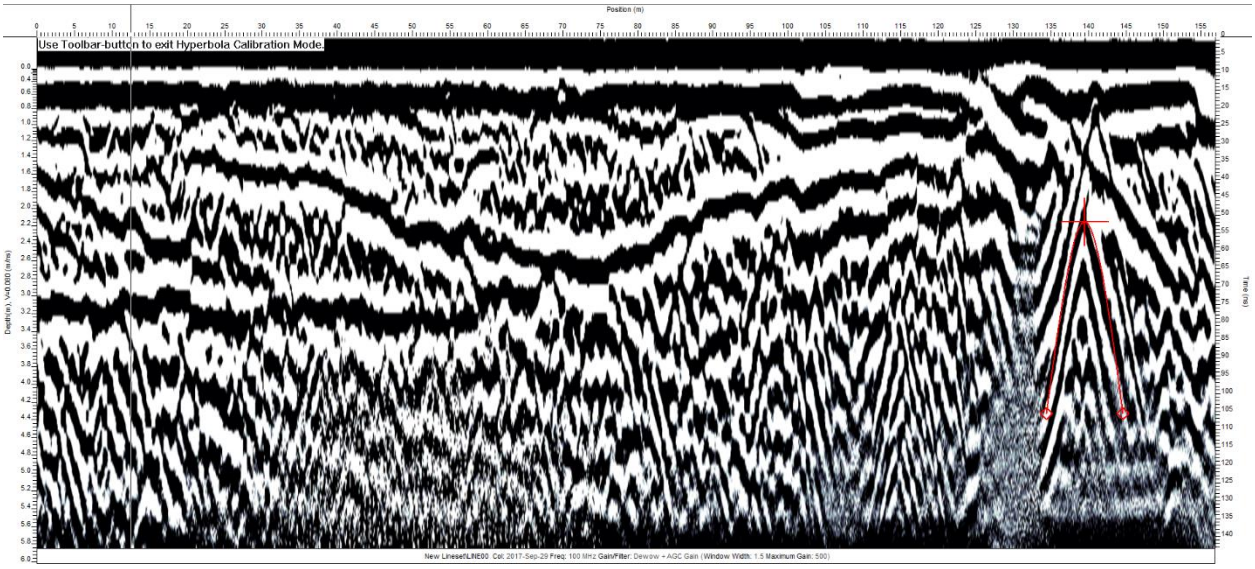

Figure 2.26: Example of a GPR profile from TB3, showing a hyperbola being measured with the Hyperbola Calibration Mode tool (red hyperbola on right side of the Figure).

Different surface features can cause reflections to be superimposed onto radar profiles that obscure the primary reflections of interest with ‘ringing’. This ‘ringing’ manifests in profiles in the shape of large hyperbola (Figure 2.23) and noise, and can be caused by surface objects such as trees, boulders, and metal fences (Neal, 2004). These surface reflections can be removed or addressed by several different methods. One method applied was to use geometrical modeling and synthetic radar profiles to separate surface reflections from the primary reflections. In some instances, migration, which is a processing technique that will be explained in the next paragraph, and careful interpretation can be used to distinguish the surface reflections from the primary reflections. However, if there are many surface reflections to the point it makes it difficult to distinguish them from the primary reflection, then a modified seismic processing stream can be used to remove surface reflections from a radar profile (Neal, 2004).

Migration is a processing technique that moves reflections from apparent locations to the true locations (Smitha et al., 2016). It can be used to correct for distortions, diffractions,

dip-displacements, and out-of-line reflections (Neal, 2004), and does this by mathematically collapsing hyperbole to single points that will represent a more accurate position of the targets (Utsi, 2017). There are different types of migration, but the two types that are commonly used are Kirchhoff migration and F-K migration. Both are good to use for GPR data processing and only have a small percent of error (Smitha et al., 2016).

Kirchhoff migration is a non-recursive method, meaning it uses a formula for a sequence that does not depend on any other terms in a sequence (Smitha et al., 2016). This type of migration applies an integral form of wave equation and is based on Huygens principle, which states that every point on a wave front may be considered as a source of secondary waves (Tkachenko, 2006). According to this principle, the seismic reflector is considered to be comprised of closely placed point diffractions and the apex of the diffraction curve to be the location of the true point reflector (Smitha et al., 2016). The Kirchhoff migration aims to sum up the energy created by Huygens secondary sources and focus it into a point of generation as seen in Figure 2.27 (Smitha et al., 2016). By using this migration method, each point in the migrated section is independent from the other points (Smith et al., 2016). Outside of the migrated sections, the points are created by adding all data values along a diffraction that is centered at that point (Smitha, et al., 2016).

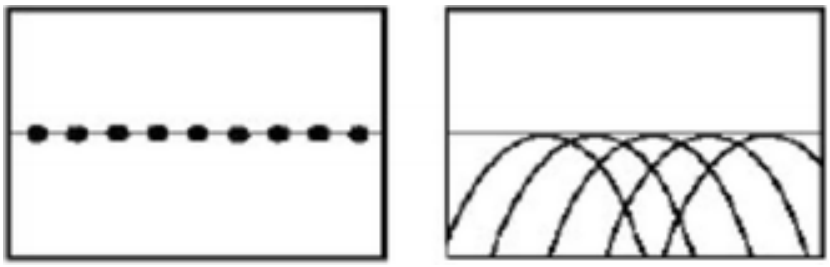

Figure 2.27: Collapsing diffraction hyperbola to its apex. From Smitha et al., 2016.

F-K migration applies a synthetic aperture image reconstruction process to the GPR profile (Sensors and Software, 2018), and reconstructs the image by Fourier-transforming the GPR data into plane waves at a single, constant frequency. Each wave is then processed individually so that the energy is superimposed at a source point (Sensors and Software, 2018). In other words, it acts as a spatial deconvolution designed to collapse hyperbola that are created from point-like targets back to points (Sensors and Software, 2018).

An example of migration applied to an aeolian setting (Panel b in Figure 2.28). In the radar profile, large diffractions caused by trough blowout can be seen in Panel a. In Panel b, the profile has been corrected by migration. For this thesis, migration was not applied, as it was found that when migration was applied, it obscured other GPR features within the profile, making them uninterpretable and did not improve the profile when applied. In Figure 2.29, an example of both migration methods discussed above are applied to a GPR line used in this thesis. In Panel A of Figure 2.29, no migration has been applied. For Panel B in Figure 2.29, F-K migration was applied, but it does not improve the GPR profiles much and also has the potential to obscure some of the data. Kirchhoff migration was applied to Panel C in Figure 2.29 and it is seen to have a negative effect on the data, reducing the resolution of the GPR profile.

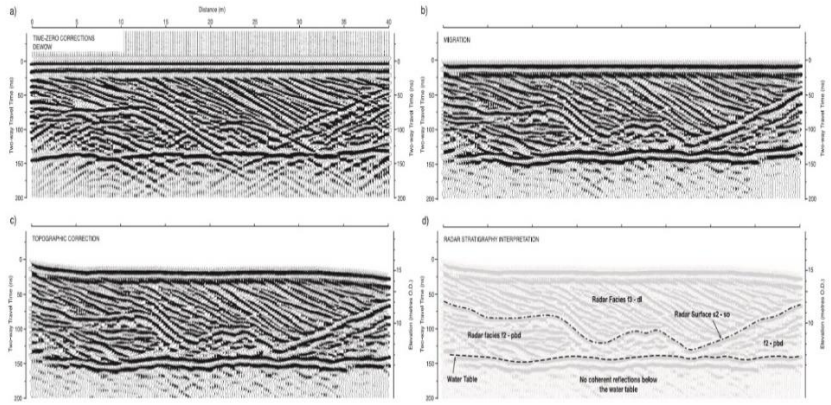

Figure 2.28: A: A radar profile (100MHz) of a large, coastal, trough blowout that occurred at Raven Meols, Sefton, Northwest England. Time-zero and 'dewow' filter applied. **B:** Migration applied using a velocity of 0.132m/ns **C:** Topographic correction applied **D:** Interpretation of the radar profile. From Neal, 2004.

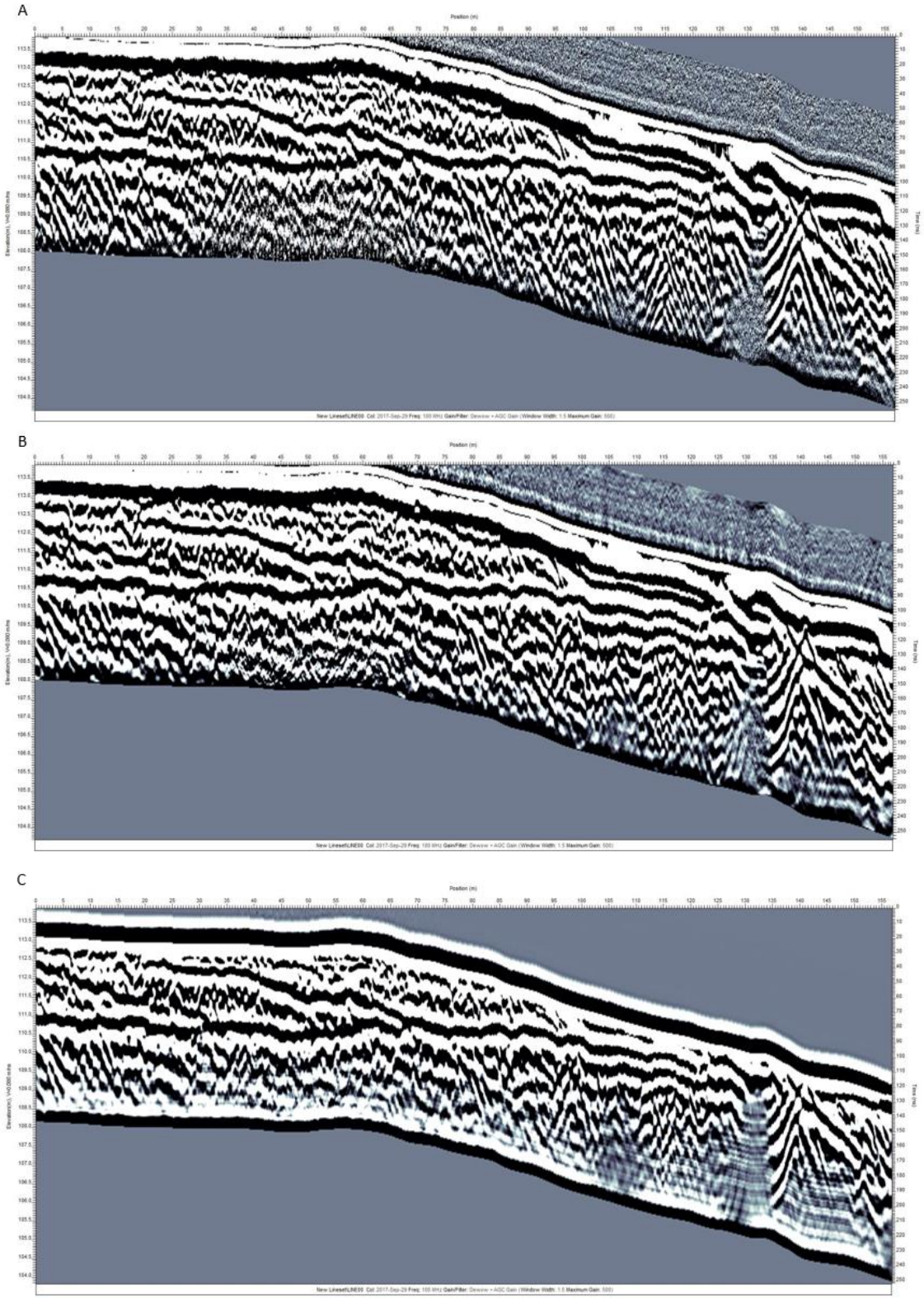

Figure 2.29: Displaying the application of migration to the GPR profiles from the current thesis. A-C are a GPR profile from the point bar of TB3. **A:** shows no migration applied. **B:** F-K migration was applied. **C:** Kirchhoff migration was applied.

2.4 Interpretation of GPR data

2.4.1 Facies Scheme Development

After processing the GPR profiles, the interpretation of the reflections allows a radar facies scheme to be developed. Facies are bodies of sediment that are recognizably distinct from adjacent sediments. Once the processing is complete, the radar facies are identified based on their geometrical characteristics. In other words, radar facies are classified on the shapes, sizes, angles and intensity characteristics of different reflections within the GPR profile. For example, a feature in the radar facies can be shaped such as troughs, low (below 15 degrees) or high angle slopes (15 degrees or greater), planar surfaces, or displaying onlap and offlap. The size of these reflectors or their truncation (a reflector being pinched out) are also characteristics considered. While interpreting the profile, it is helpful to mark the different layers and features with interpretive lines and colors (Figures 2.13 and 2.22) to make them easier to differentiate. After the radar facies are identified, the causes of these reflections should be considered. These reflections must be differentiated as those features created by sedimentary processes, or if they could be created due to noise and interference (Neal, 2004).

Based on sedimentary processes features, the sedimentary facies can then be interpreted from the radar facies. The sedimentary facies are bodies of sediment that are distinct from adjacent sediments that are formed by different depositional processes. In other words, when observing sedimentary GPR profiles, sediment is deposited chronologically, and the sediment deposits should relate to one another (Bristow and Jol, 2003). This will be very useful when determining what is happening geomorphologically in the point bar and within the channel overall. For example, troughs can be identified as erosional surfaces of bedforms

and the low angle surfaces may likely represent lateral accretion surfaces generated as a point bar migrates.

2.4.2 Quantification of the GPR Facies

After developing the facies scheme, the frequency of occurrence of the different facies throughout the GPR lines both transversely and longitudinally was determined, using a similar method as developed by Sambrook Smith et al. (2006). First, each GPR profile was broken into a grid, with the vertical spacing set at 0.5m. To determine the best horizontal spacing that would best quantify the grid, the GPR panel was sampled every 2m, 4m, and 8m. Using each of these horizontal spacings, the percentage of facies present was calculated, and expressed as the length of each facies in a given vertical profile divided by total depth. This resulted in quantification of the percentage of each facies present every 2m, 4m, and 8m. Another way of visualizing this is to think of these horizontal spacings as if cores were taken at every 2m, 4m, or 8m. Then, the amount of each sedimentary facies is calculated at a 0.5m resolution in each of the core samples. By using this method, it visualizes how the presence of certain facies not only change from upstream to downstream, but also how they from the interior of the point bar towards the thalweg.

After examining these results using the different horizontal sample spacings, it was determined that 4m best quantified the facies within the lines, which results in the final grid spacing as shown in Figure 2.30. This 4m spacing provided a detailed assessment of how the percentage of each facies changed throughout the 2-D GPR profiles. Additionally, the overall average percentage of facies was also calculated for each GPR profile, giving an approximation of how much of each facies is present in each 2-D profile (Sambrook Smith et al., 2006).

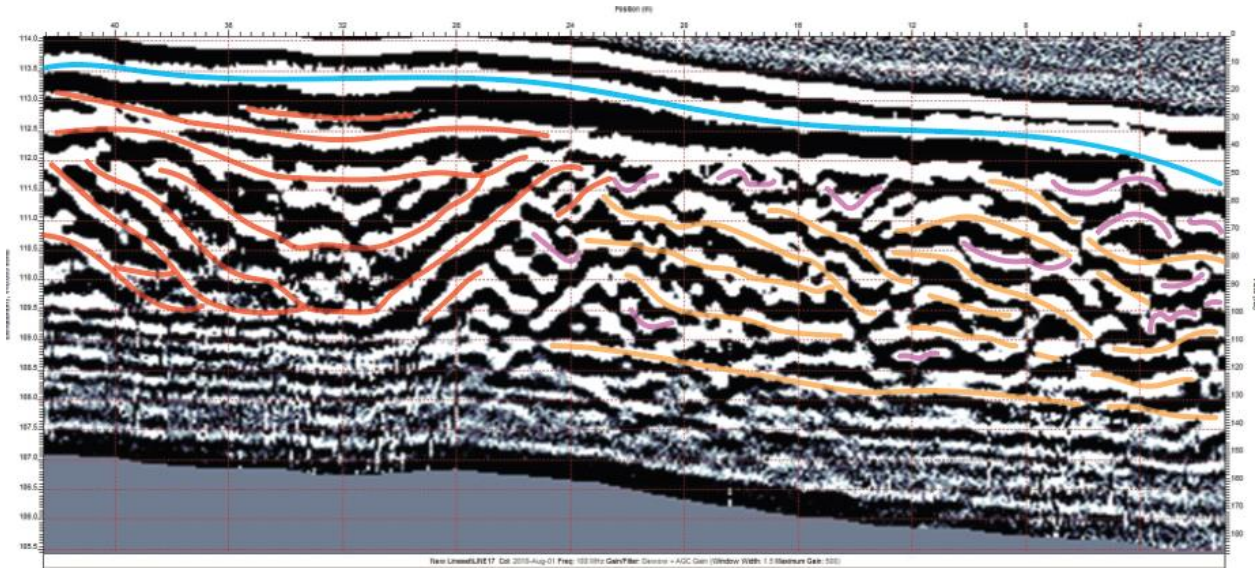

Figure 2.30: Example of grid spacing for GPR profile. Horizonal spacing is every 4m and vertical spacing is every 0.5m. This GPR profile shows a transverse line in TB3.

CHAPTER 3: RESULTS

3.1 Aerial Photo Interpretation

Maier Bend is characterized by an expanding point bar that is migrating northward. Figure 3.1 shows the progression of bend expansion between 2004 and 2018 using the position of the bar edge at low flow. These images show that deposition occurred along the mid-bar section of Maier Bend and as the bend expanded, the outer bank rapidly eroded at a rate of 3.52 m yr^{-1} (Rowley, 2020). The upstream section of the bar has the most deposition that reaches a maximum of 1.75m in height. The maximum erosion (0.75m in depth) occurs along the bar head with erosion along the bar tail reaching a maximum of 0.45m in depth. A small section of deposition (1.4m in height) occurs downstream and next to the erosion that is happening on the bar tail (Rowley, 2020).

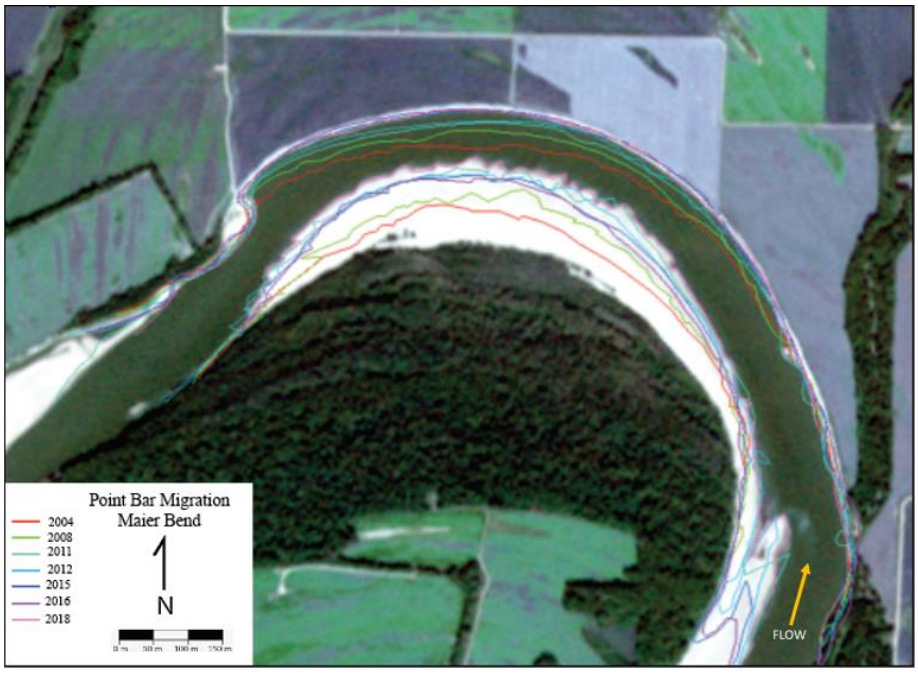

Figure 3.1: Digitized point bar lines showing the expansion of Maier Bend between 2004-2018, as cutbank erosion has shifted in this time period.

TB3 is a bend that is translating downstream, but also displays expansion in the southeastern direction (Figure 3.2). Along the bar head of TB3, a maximum of 1.15m of erosion occurred (between 2004-2018, Fig. 3.2; Rowley, 2020), and the minimum outer bank retreat was adjacent to the areas of maximum deposition. Additionally, the maximum outer bank retreat was adjacent to the maximum deposition along the bar, with the average migration rate for TB3 being 4.27m yr^{-1}. TB3 has shown more deposition compared to Maier Bend, with up to 3.8m along the bar tail. During 2011-2017, a large bar front moved across the bar and overall increased the area of TB3's point bar. If the extent of the 2017 TB3 bar tail is superimposed onto the DoD, the amount of growth along the bar tail since 2011 is apparent (Rowley, 2020).

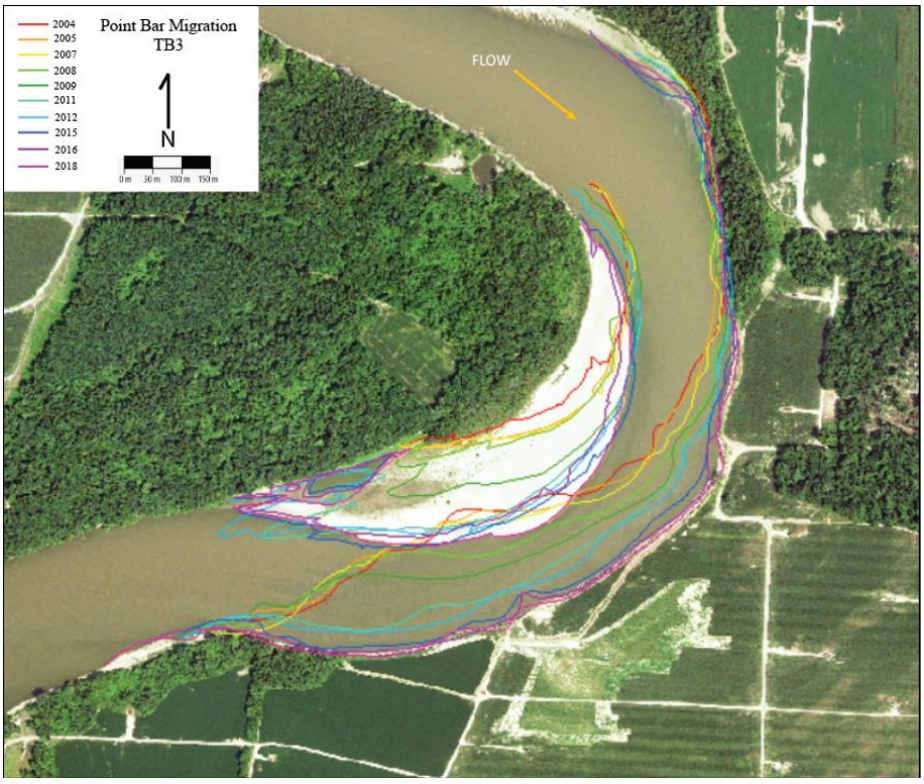

Figure 3.2: Digitized outlines of the point bar and cutbank for TB3 from 2004-2018, illustrating the bar has translation and expansion, together with the cutbank erosion.

3.2 Bend Morphology

3.2.1 Dunes

In 2019, MBES surveys were collected by Dr. Kory Konsoer (Louisiana State University) and show the bend morphology of both Maier Bend and TB3. These surveys can be used to identify the principal morphological elements of these bends. Dunes are one of the most abundant morphological features seen in the MBES surveys of both of these bends. The dunes vary in size; but on the Maier Bend point bar, they are *c.*3-5m in length (crest to crest), 1-3m in width, and 0.2-1m in height (Figures 3.4 and 3.5). The dunes are larger in greater flow depths.

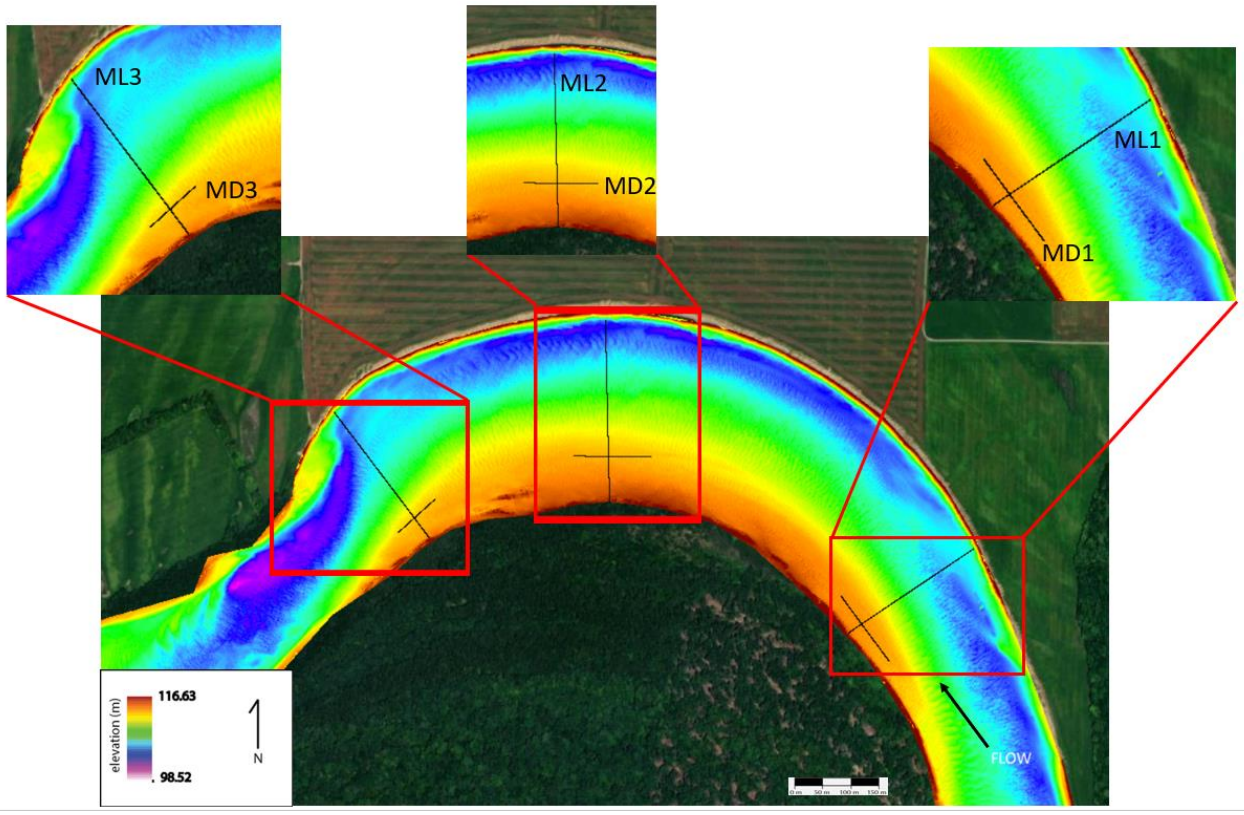

Figure 3.3: Location of point bar topographic lines for Maier Bend (charts is for these profiles in Figure 3.4 and 3.5).

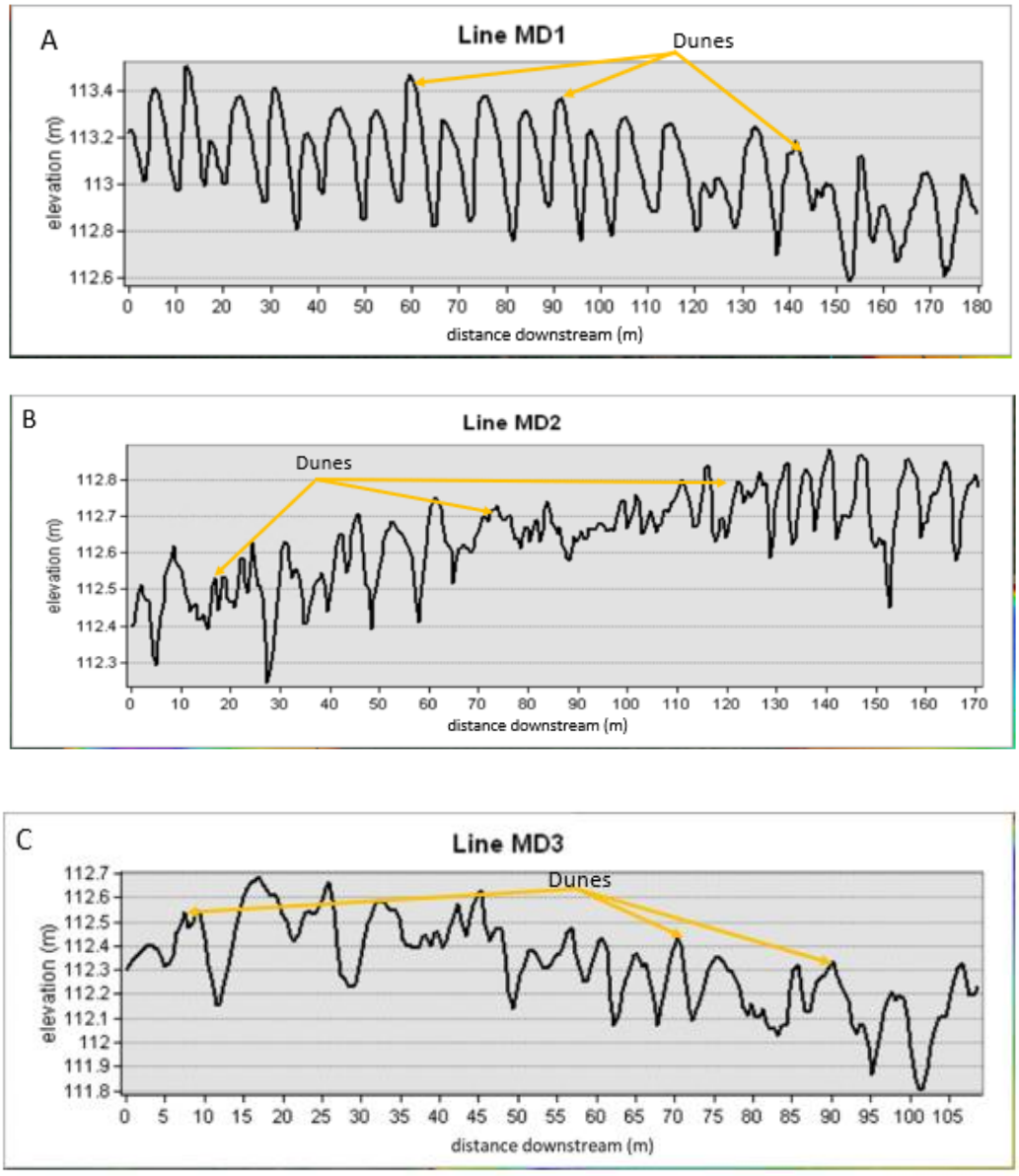

Figure 3.4: Longitudinal point bar topographical profiles for Maier Bend to show dune width and height. **A-C:** Left to right is upstream to downstream. Examples of dunes are marked by yellow arrows. **A:** Upstream point bar topography (Line MD1); **B:** Mid-bar point bar topography (Line MD2); **C:** Downstream point bar topography (Line MD3).

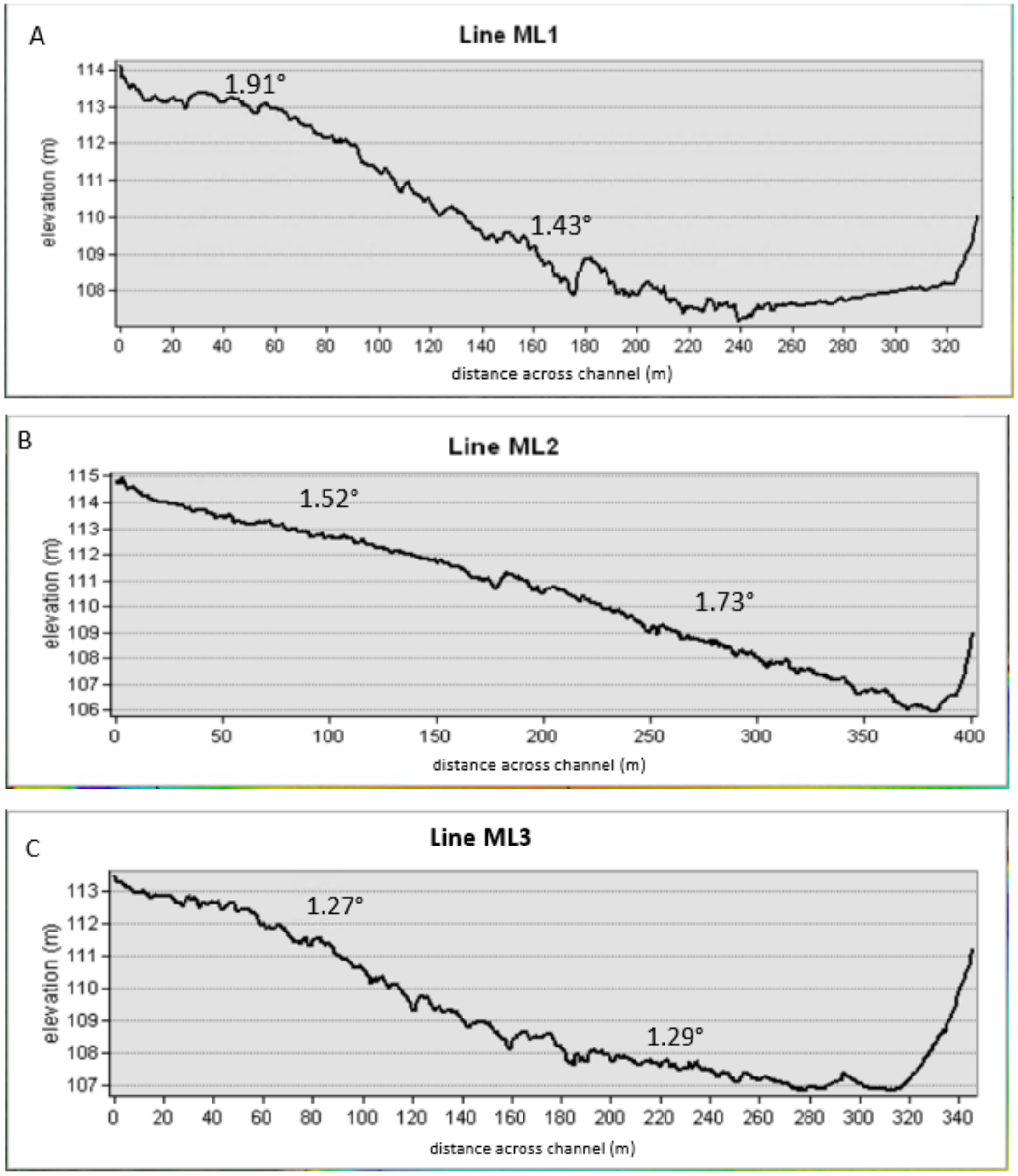

Figure 3.5: Lateral lines for Maier Bend, showing channel topography. **A-C:** Left to right is from interior of bar towards cutbank. Blue triangle shows upper point bar angle. Orange triangle shows lower point bar angle. **A:** Upstream, channel topography (Line ML1). **B:** Mid-bar, channel topography (Line ML2). **C:** Downstream, channel topography (ML3).

Dunes are also abundant throughout TB3. Figure 3.6 shows a close-up of the dunes seen in the mid-bar section of TB3. In Figure 3.6, the dunes within TB3 are smaller in scale closer to the interior of the bend and become larger as they increase into the thalweg (Figure 3.8). Dunes

on the point bar are roughly 5-6m in length (crest to crest), 1-3m in width, and 0.2-0.5m in height (Figure 3.7; Figure 3.8).

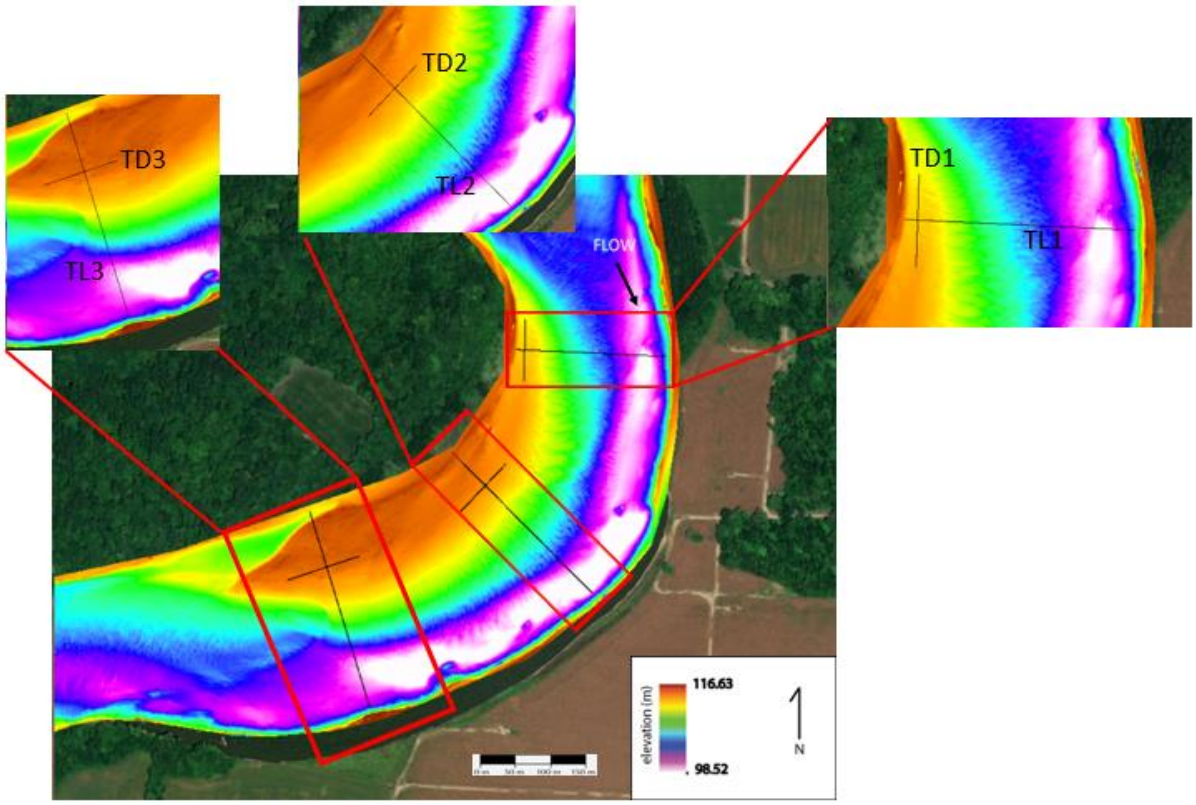

Figure 3.6: Location of point bar topography lines for TB3 Bend (charts is for these profiles in Figure 3.7 and 3.8).

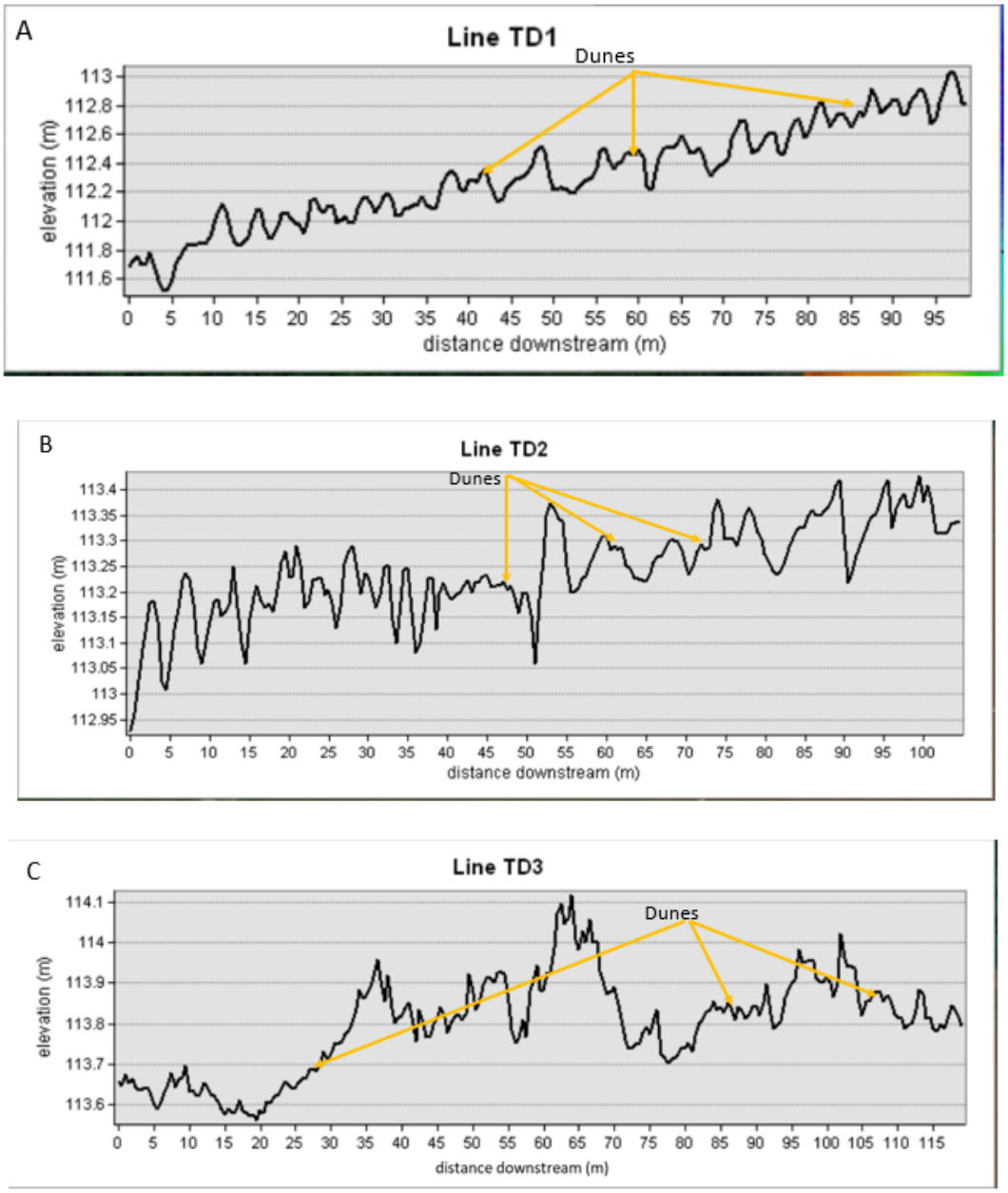

Figure 3.7: Longitudinal point bar topographical profiles to show dune width and height for TB3. **A-C:** Left to right is upstream to downstream. **A:** Upstream point bar topography (Line TD1). **B:** Mid-bar point bar topography (Line TD2). **C:** Downstream point bar topography (Line TD3).

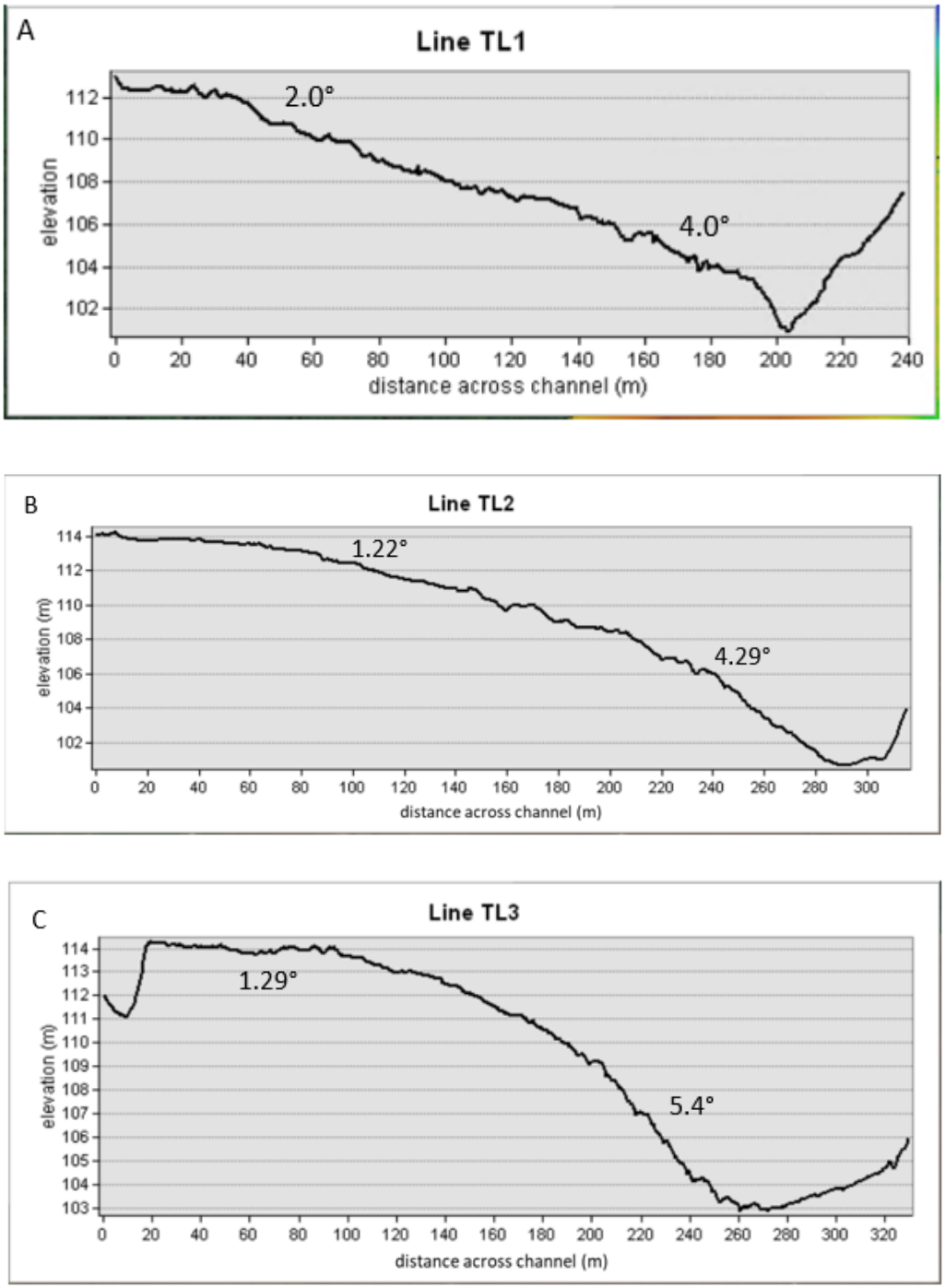

Figure 3.8: Transverse lines of point bar topography for TB3, showing dune length and height. Left to right is from interior of bar towards channel side. **A:** Upstream, transverse point bar topography (Line TL1). **B:** Mid-bar, transverse point bar topography (Line TL2). **C:** Downstream, transverse point bar topography (Line TL3).

3.2.2 Unit Bars

Unit bars are another morphological feature present in both Maier Bend and TB3 point bar. The unit bars are not clearly seen in the MBES surveys, but are visible in aerial imagery. Unit bars are typically present on the channel side of the point bar (Figure 3.9) and are *c.* 30-200m in length.

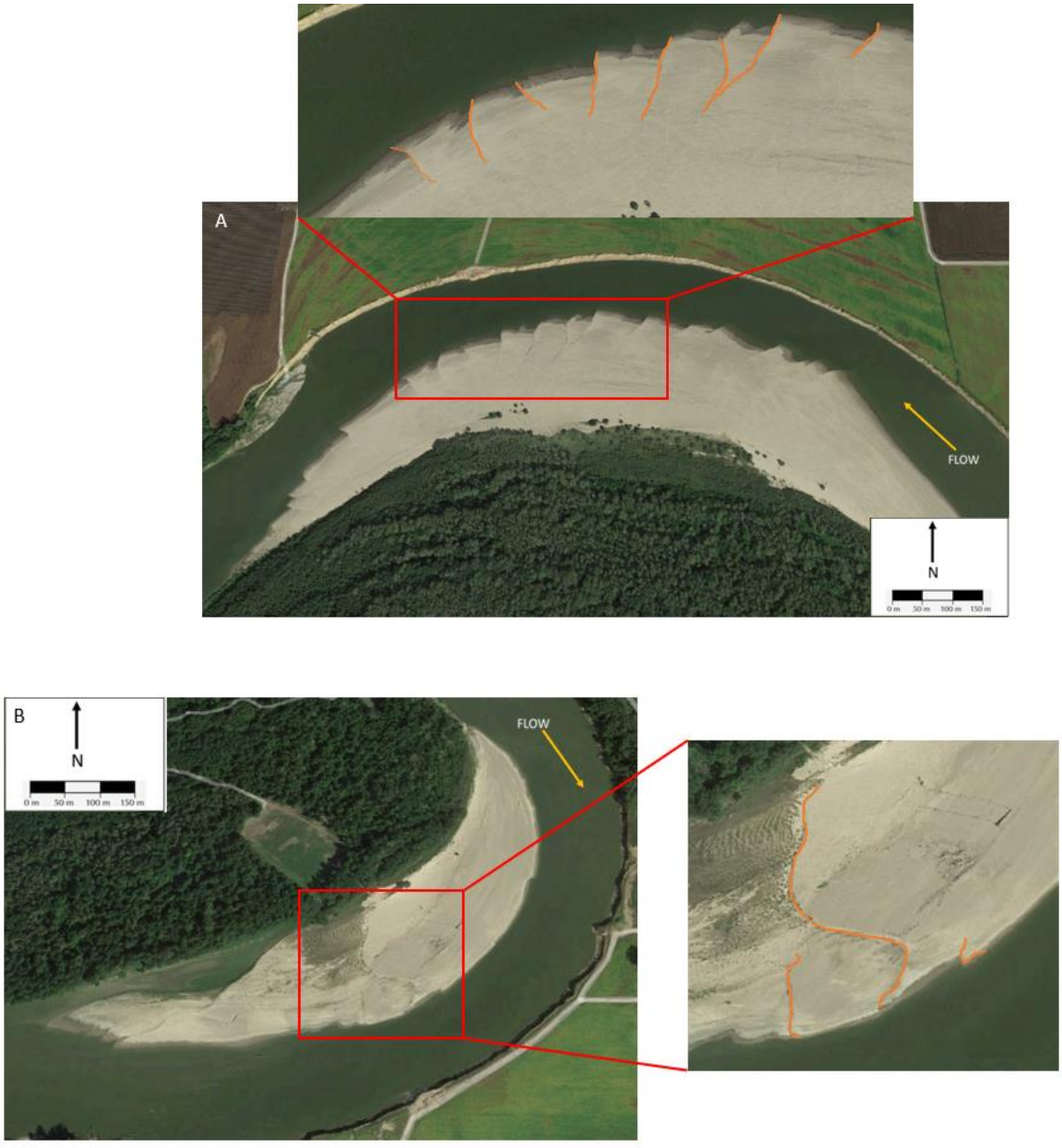

Figure 3.9: Examples of unit bars on both the Maier bend and TB3 point bars. Aerial imagery is from 2013. **A:** Maier Bend point bar. Unit bars marked by orange lines. **B:** TB3 point bar. Unit bars marked by orange lines.

3.2.3 Point Bars

Within Maier Bend, a series of pools and point bars are present (Figure 3.10; Konsoer, 2016a). The elevation change from the highest point (~114m) to the lowest point (~104m) is about 10m. Along the interior of the bend, the point bar possesses a relief of about 5-6m as it slopes towards the outer edge of the bend (northward). The point bar is approximately 1500m in length. On the outer edge of the bend, there is a pool in the thalweg and that is about 9m below the outer banks at its deepest point (Figure 3.10). The pool in the thalweg (blue area marked by the red box in Figure 3.10) is roughly 1350m in length.

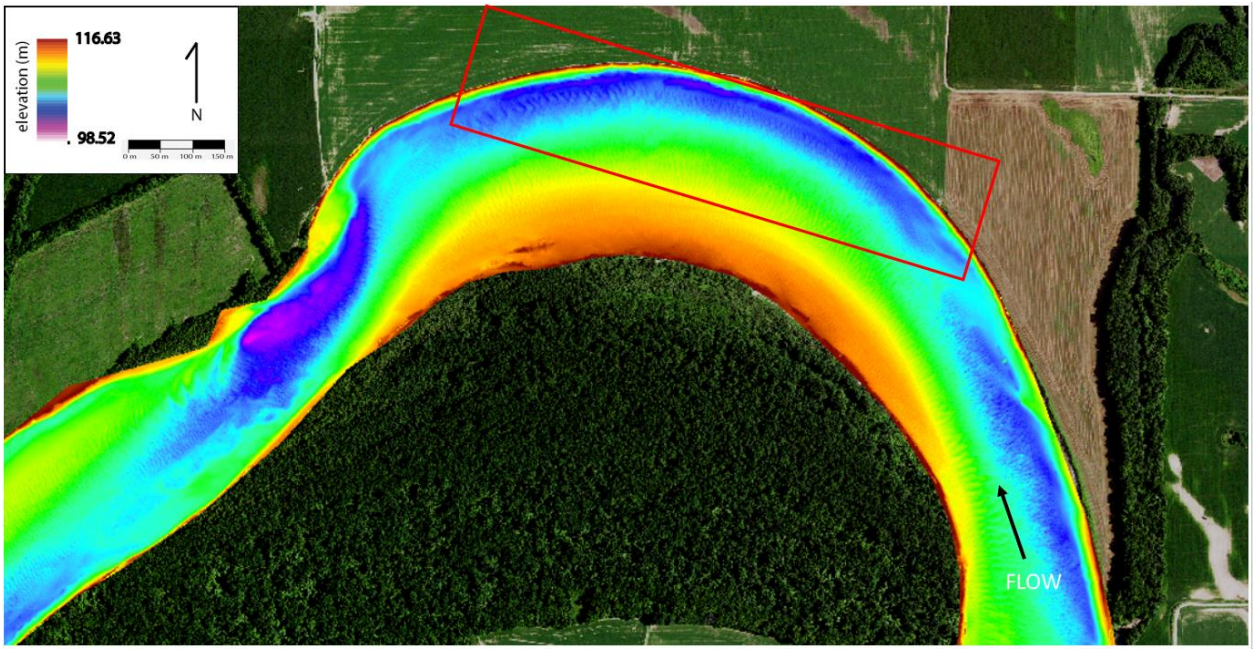

Figure 3.10: Bathymetric map of Maier Bend derived from 2019 multibeam survey. Red box marked pool in the thalweg.

The deepest part of Maier Bend is at the downstream end of the bend (labeled in Figure 3.11) due to scour caused by the narrowing of the channel at a bedrock outcrop (labeled in Figure 3.11), thus increasing the velocity of the flow. Just southwest of the bedrock outcrop, there is an area of deposition due to a decrease in flow velocity as water flows around the outcrop (Konsoer,

2016a). At the deepest point of the pool in Figure 3.11, the depth is *c.*10m below the outer bank with the pool being 525m in length and about 110m wide.

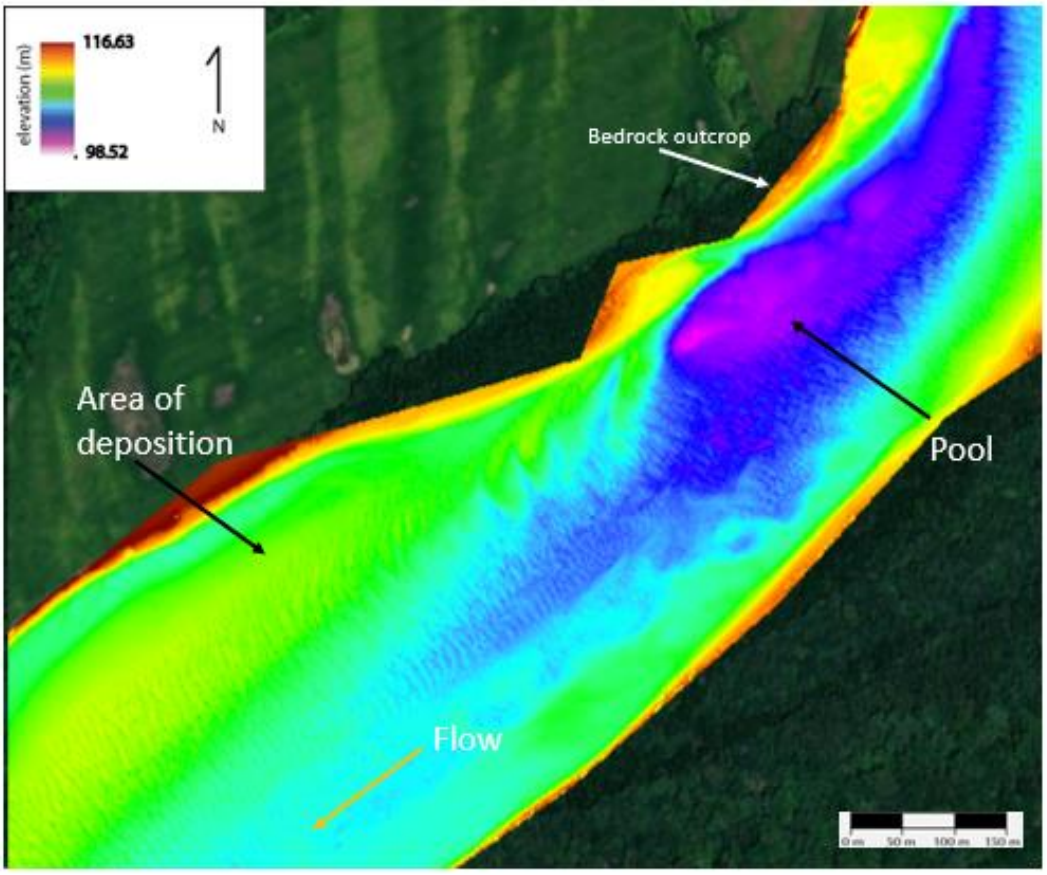

Figure 3.11: Bathymetric map of the downstream limb of Maier Bend showing the lowest point of the bend and the bedrock outcrop.

In TB3 (Figure 3.12), the relief of the point bar is *c.*5-6m and is *c.*1200m in length. Along the exterior of the bend, there is a large pool that is also the lowest part of the bend that is approximately 14m below the top of the outer bank, and approximately 1300m long and 80m wide.

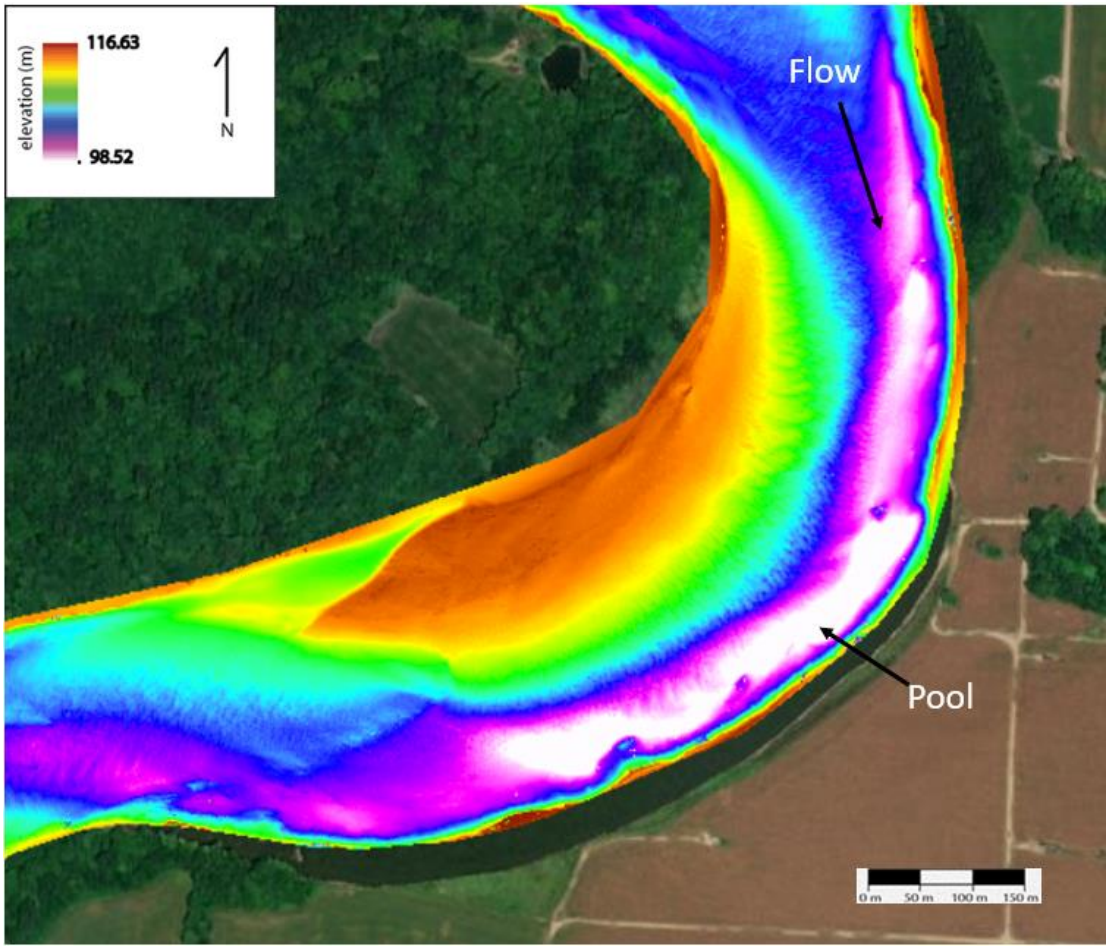

Figure 3.12: Bathymetric map of TB3 derived from a 2019 multibeam survey. Indicates deepest part of the bend.

3.2.4 Bar Top Hollow

In the downstream section of TB3 (Figure 3.13), a pool is present at the tail end of the point bar, likely forming as the unit bar in TB3 wrapped around the bend. As the bar-tail accretes, a horn shape forms and an isolated depression is left, similar to the bar top hollows described by Best et al (2006). Subsequently, this depression can be filled as the bar continues to migrate downstream. The bar top hollow is *c.* 60m wide, 290m in length and 2m deep.

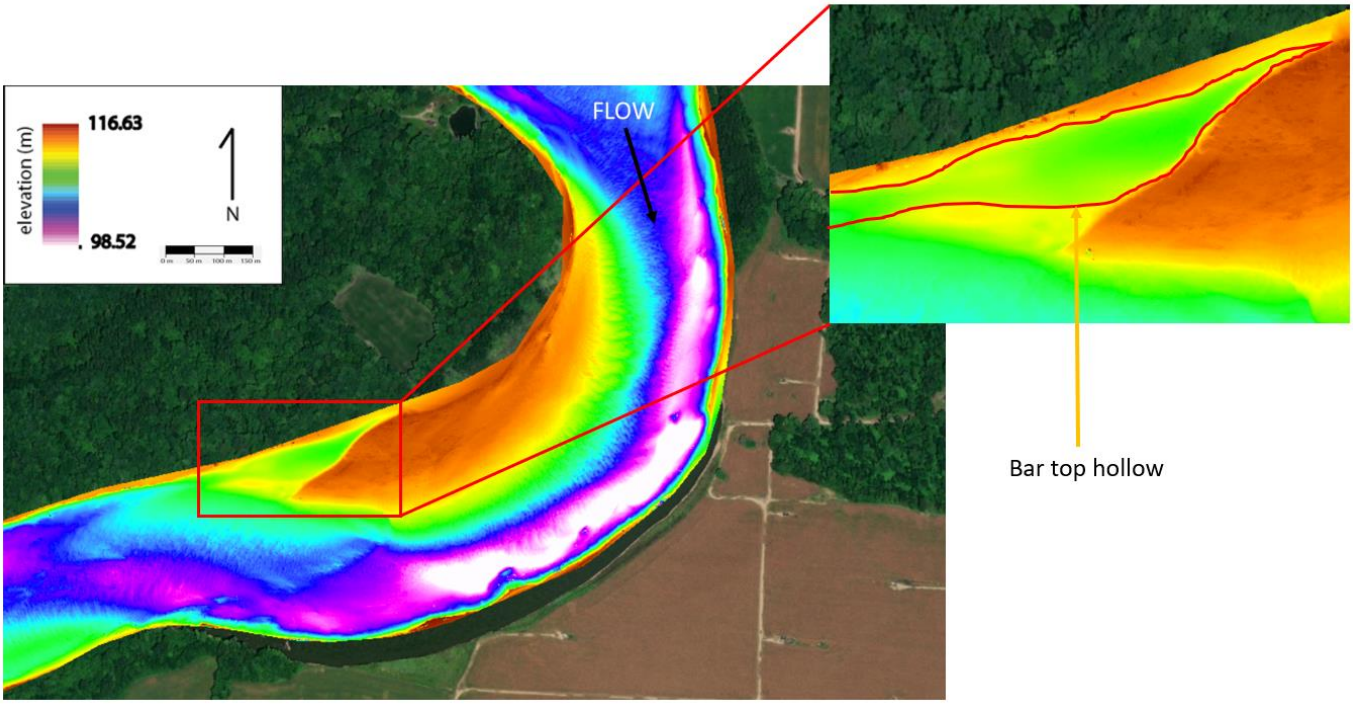

Figure 3.13: Bathymetric map of the downstream end of TB3 point bar. This image highlights the bar top hollow at the tail end of the point bar.

3.3 GPR Facies Interpretation

3.3.1 Description of Facies

After analyzing the transverse and longitudinal GPR profiles, six GPR radar facies were identified (Table 3.1). Table 3.1 shows an example of each of these radar facies and an example within the GPR line.

Facies #	Radar Facies	Morphological Interpretation	Example in GPR
1a	Low-angle slopes (5-13 degrees) with high-angle slopes (20-30 degrees) and/or troughs packaged in between. 2-5 m thick. 20-150m long.	Point bar lateral accretion surfaces with superimposed transverse bars or dunes	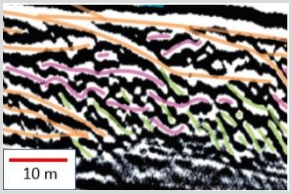
1b	Similar to facies 1a. Low angle slopes, but lacking other features packaged in between. 3-7m thick. 20-150m long.	Point bar lateral accretion surfaces migrating towards the cut bank	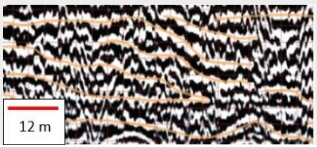
2	High angle slopes (15-32 degrees) in the transverse lines that are close to the thalweg. 0.2-2m thick. 0.5-5m in depth.	Unit bar migrating towards the thalweg	
3	Small-scale troughs (roughly 1-5m, crest to crest). 1-2m in thickness.	Dunes	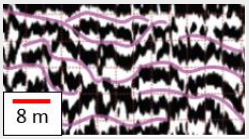
4	Large-scale troughs (10's of meters in size, crest to crest). 0.5-1m in thickness. Located at 0-2m in depth.	Bar top hollows.	
5	Planar surfaces. 0.5m thickness. 5-100m length	Sheets of gravel with any bedforms below the resolution of GPR	
6	Hyperbola. Found at any depth. 2-10m wide.	Tree branches, tree trunks, rocks, or gravel	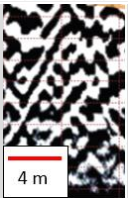

Table 3.1: Radar facies description, sedimentary facies description, and examples of the facies based on the features found within the TB3 and Maier point bars in the Wabash River.

Facies 1

Radar facies 1 was broken into two categories: 1a and 1b. Radar facies 1a (Figure 3.16) comprises low-angle sloping reflectors (5-13°) with high-angle slopes (20-30°) and/or trough-shaped reflectors packaged in between. Facies 1a is *c.* 2-5m thick.

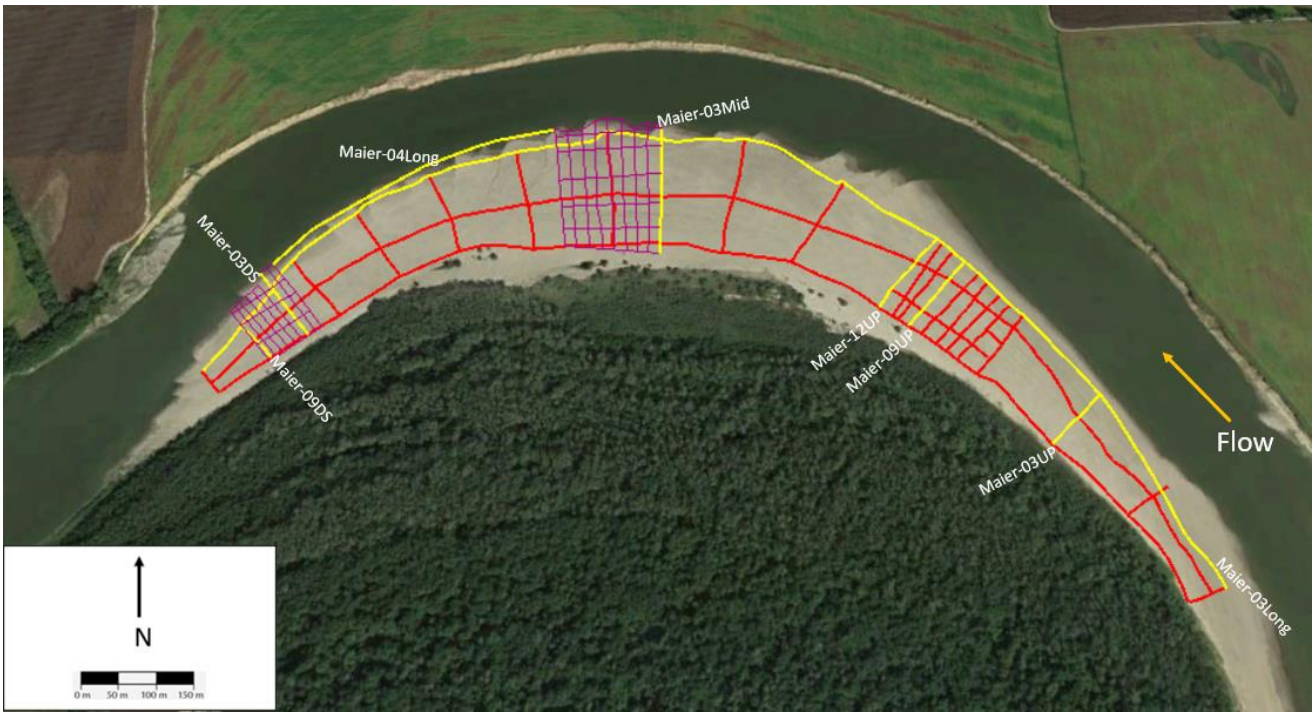

Figure 3.14: Red and purple lines represent GPR profiles taken in 2017 and 2018 for Maier bend. The highlighted yellow lines are the GPR profiles that will help highlight the facies discussed in the present thesis and be referenced when explaining the locations of the survey lines.

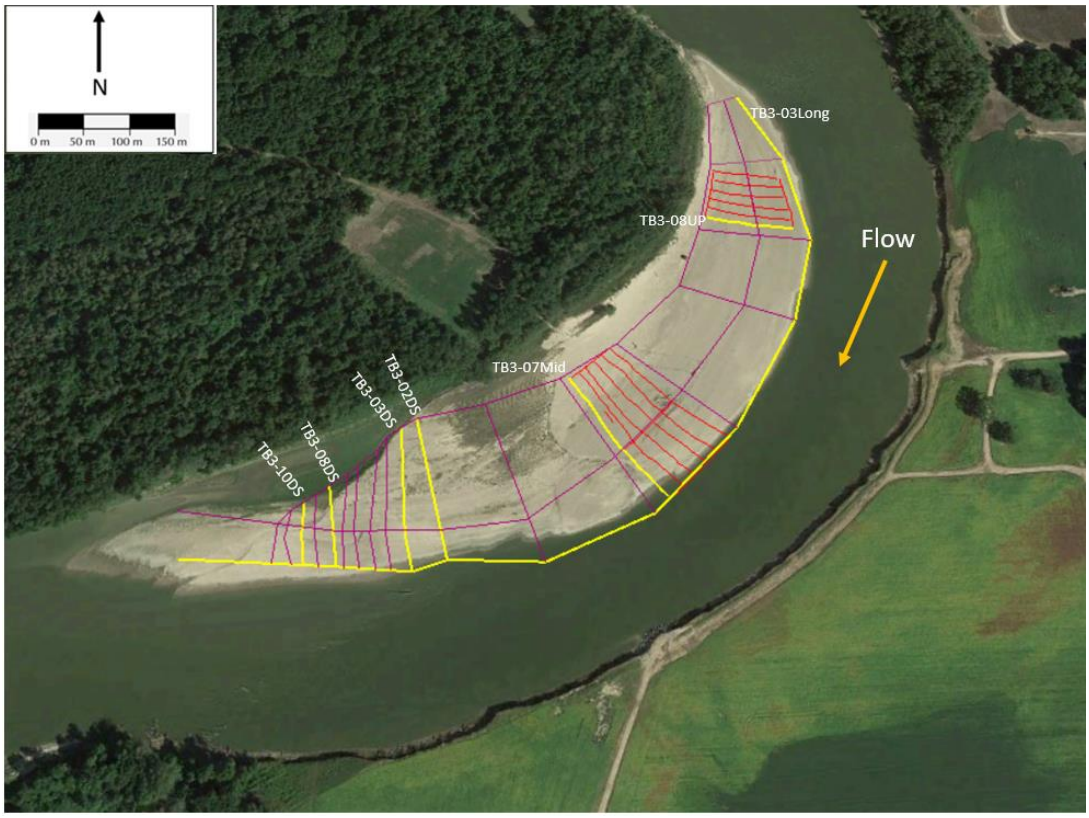

Figure 3.15: Red and purple lines represent GPR profiles taken in 2017 and 2018 for TB3. The highlighted yellow lines are the GPR profiles that will help highlight the facies discussed in the present thesis and be referenced when explaining the locations of the survey lines.

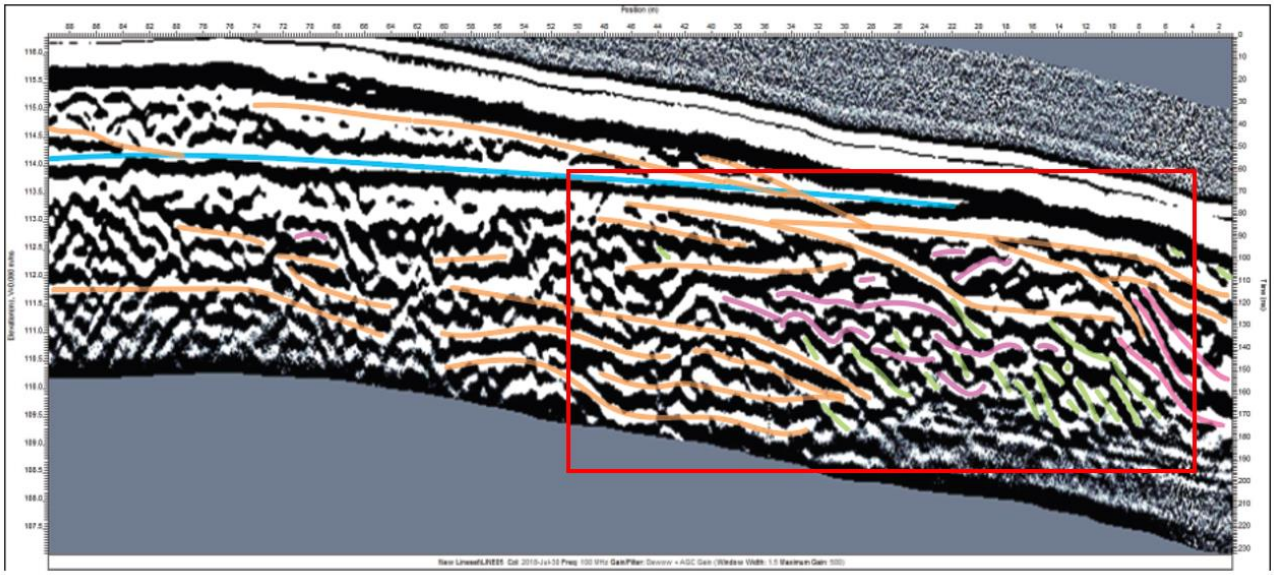

Figure 3.16: TB3-08UP: Upstream, transverse GPR profile from TB3. An example of radar facies 1a is marked by the red box. The orange lines represent the low-angle surfaces. In between the orange lines, the purple lines represent small trough features (radar facies 3) and the green lines represent high-angle surfaces (potentially radar facies 2 interbedded in between). Location of line labeled on Figure 3.15.

Radar facies 1b (Figure 3.17) also has low-angle slopes (5-13°), but is either lacking the small-scale features or they are too small to be seen as they are in radar facies 1a. The thickness of radar facies 1b ranges between 3-7m. For both radar facies, the length of the low-angle surfaces within radar facies 1a and 1b varies greatly. In the transverse lines of Maier Bend and TB3, the low-angled surfaces range from *c.*10-30 m in length whereas in the longitudinal lines, they range from *c.*20-150m in length.

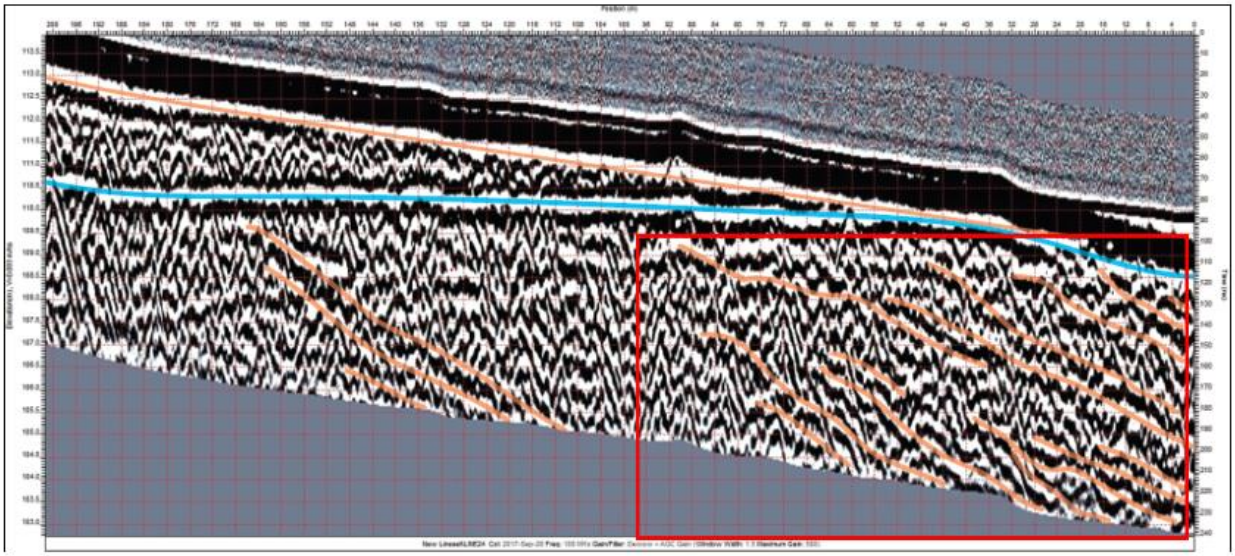

Figure 3.17: Maier-03Mid: Mid-bar, transverse line from Maier Bend. The orange lines represent low-angle surfaces (radar facies 1b). The blue line represents the water table.

Interpretation:

Facies 1a represents point bar lateral accretion surfaces, with superimposed transverse bars or dunes. Facies 1b are also point bar lateral accretion surfaces that are migrating towards the cutbank, but lacking superimposed smaller features. The best example of this can be seen in the Maier Bend transverse lines. In the upstream section of the Maier Bend point bar (Figure 3.18A), small scale features can be seen between the lateral accretion surfaces for the first few lines. However, in the transverse GPR lines closer to mid-bar, the amount of visible small-scale features decrease in abundance or are limited to the channel side of the point bar. This could be

due to the resolution of the GPR. Another possibility for this decrease in visible small-scale features is due to grain size in that the upstream section of Maier bend has a higher gravel content than the downstream section of the point bar (Rowley, 2020). Gravel tends to create point reflectors from the GPR electromagnetic signal and makes the imagery less clear. To corroborate this, facies 6 (hyperbole) are abundant within the upstream GPR profiles for the Maier point bar (Figure 3.18). Furthermore, another reason for a decrease in facies 1a may be from the angle at which the GPR profiles were collected. Because GPR profiles only represent a specific 2-D slice of the subsurface, the angle at which features are surveyed will affect their characteristics.

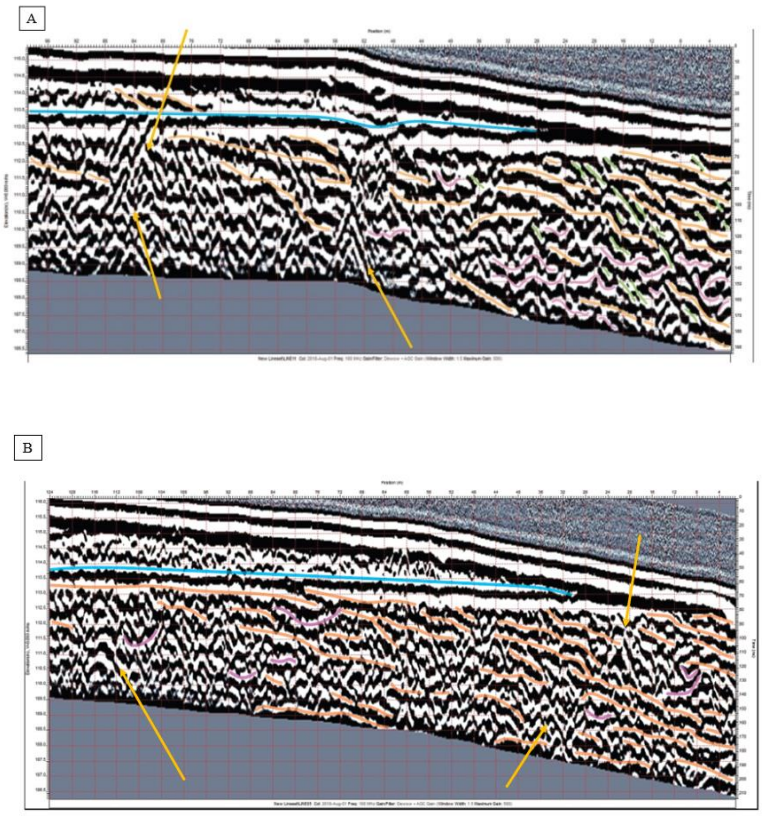

Figure 3.18: A (Maier-03UP) and B (Maier-09UP) are both upstream, transverse lines. The yellow arrows in the images show examples of the hyperbolic features that are seen in the upstream end of the bar that introduce interference in the GPR profiles. These hyperbola are likely caused by branches or tree trunks that are buried in the sediment or by the gravel that is present in the upstream section of the bar creating these reflections. Location of lines labeled on Figure 3.14.

Facies 2

Radar facies 2 (Table 3.1 and Figure 3.19) comprises of high-angle sloping (15-32°) reflectors that are close to the thalweg in the transverse GPR lines and *c.*0.2-2m thick. This facies has a length of roughly 5-10m in transverse lines and 10-20m in longitudinal lines. Radar facies 2 is found between ground level depth and to 5m in depth from the surface.

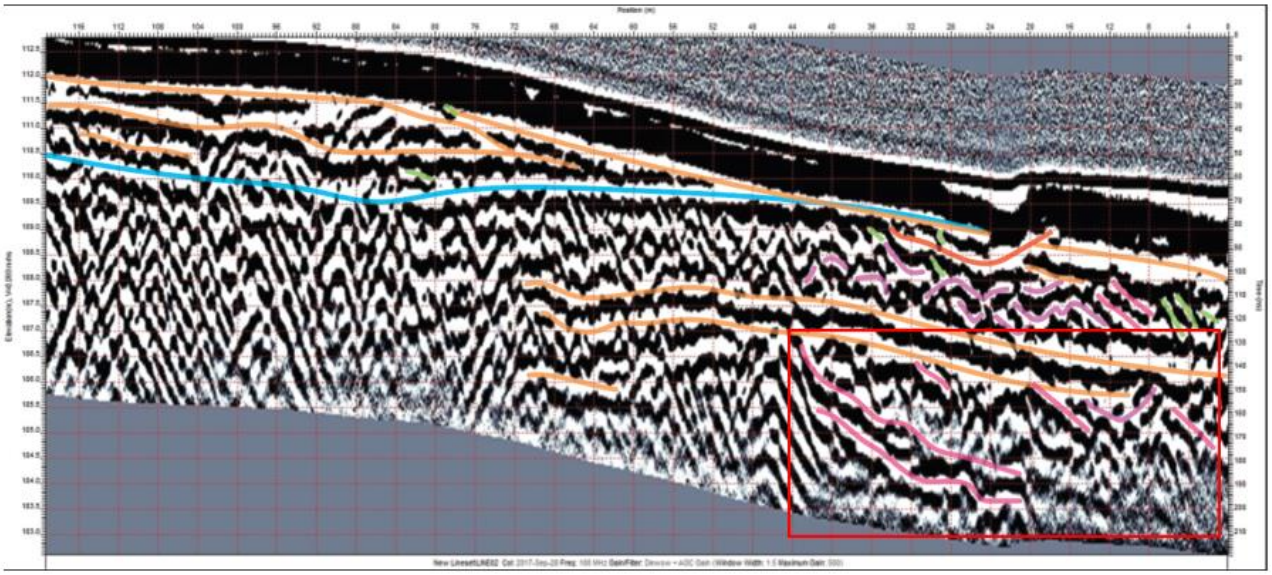

Figure 3.19: Maier-03DS: Downstream line, transverse GPR profile, showing an example of radar facies 2. Radar facies two is represent by high-angle surfaces indicated by pink lines. The location of this profile is shown in Figure 3.14.

Interpretation:

Facies 2 is interpreted as the product of unit bars migrating towards the thalweg (Figure 3.9). This facies is most easily seen in the transverse GPR lines and the longitudinal lines closest to the thalweg side of the bend. In the transverse lines, the unit bars can be seen on the channel side of the profile.

Facies 3

Radar facies 3 comprises small-scale trough-shaped reflectors that are roughly 1-5m in width. This facies is found from the surface to 4.5m deep. In the transverse lines, radar facies 3 can be found anywhere from the interior (Figure 3.20) to the channel side (Figure 3.21) of the point bar. In the longitudinal lines, radar facies 3 is most prevalent on the downstream end of the points bars for both Maier Bend and TB3. However, the facies can also be found in the mid-bar section of both point bars. Due to the small size of facies 3, the resolution and the angle at which the surveys are taken could affect whether these facies are detected within the profile.

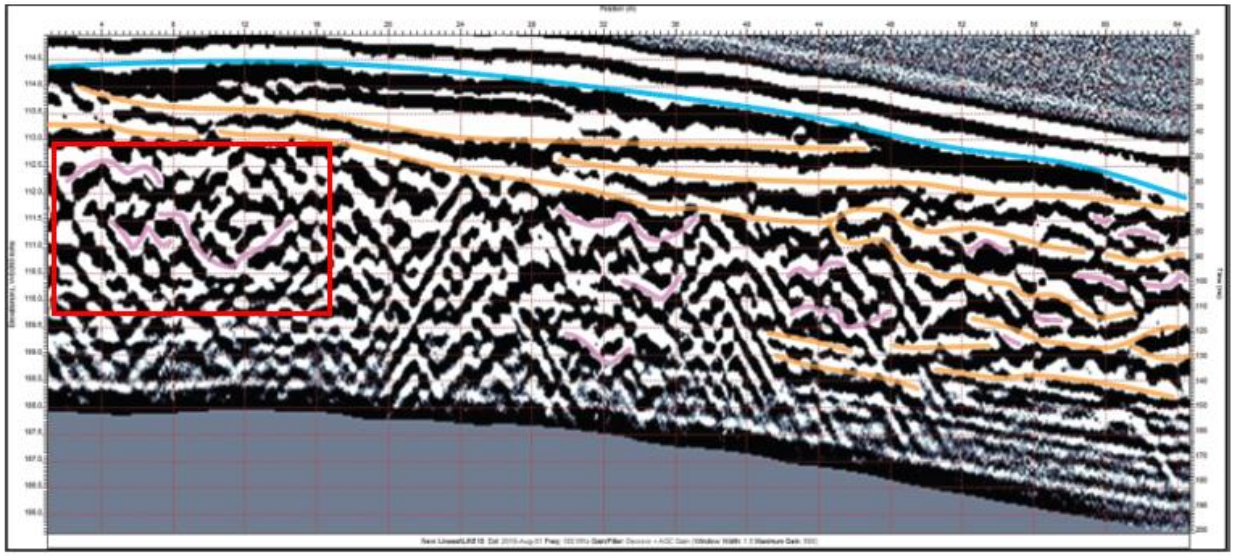

Figure 3.20: Maier-09DS: Radar facies 3, highlighted by red box and indicated by purple lines, on the interior of Maier Bend transverse line. Location of line labeled on Figure 3.14.

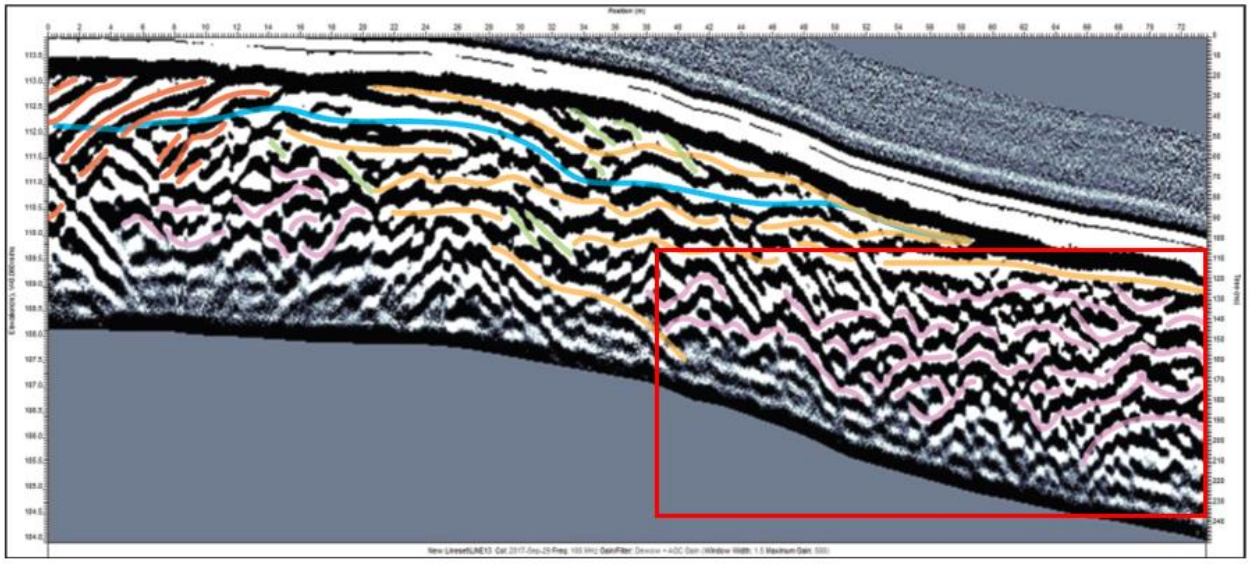

Figure 3.21: TB3-008DS: Transverse GPR line on TB3, illustrating radar facies 3 that is characterized by the purple lines and marked by the red box. Location of line labeled on Figure 3.15

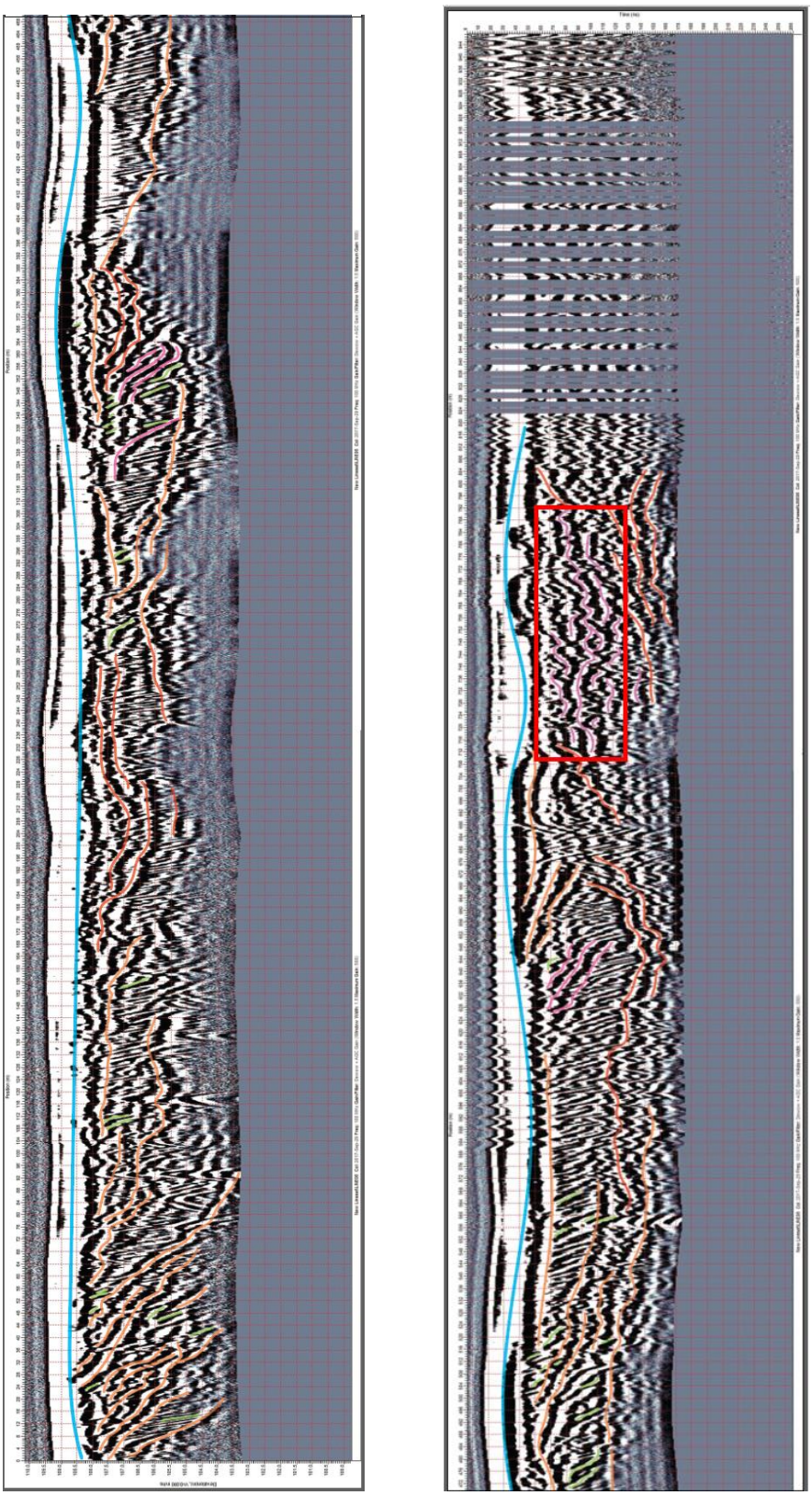

Figure 3.22: TB3-03Long: Longitudinal line on bend TB3 and showing radar facies 3 (trough-shaped reflectors marked in purple) the downstream end of the GPR profile. Location of line labeled on Figure 3.15.

Interpretation:

Facies 3 is interpreted as being produced by dunes. The dunes are most easily seen in the mid-bar to downstream sections. In the transverse lines, the dunes are commonly seen in the mid-bar to downstream profiles. As seen in the MBES (Figure 3.3; Figure 3.6), dunes are present in the interior of the point bar as well the thalweg side and are also present in the GPR profiles (Figure 3.20; Figure 3.21).

Facies 4

Radar facies 4 is characterized by large-scale trough reflectors that are *c.*10-20m in width. The troughs of facies 4 are found at *c.*1-2m depth and vary in thickness but are usually between 1 and 4 m in thickness. In transverse lines, radar facies 4 is seen on the interior section of the point bar (Figure 3.23)

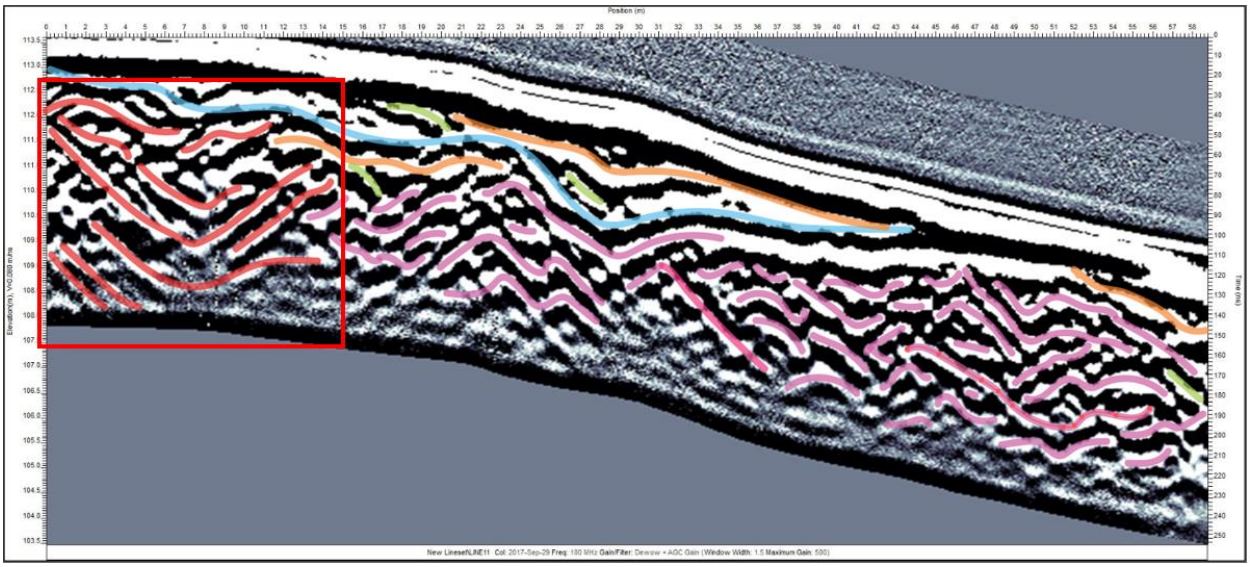

Figure 3.23: TB3-10DS: Downstream, transverse GPR profile on TB3. Example of radar facies 4 is marked by red trough-shaped reflectors. Location of the GPR profile is labeled on Figure 3.15.

Interpretation:

Facies 4 is interpreted to represent bar top hollows that form through bar-tail accretion and are found near the surface of the point bar (Figure 3.13; Best, et al., 2006). The bar top hollow located at TB3 can range from being 5-15m wide to 25m wide and 50-200m in length.

Facies 5

Radar facies 5 is 1-3m thick, consists of planar surfaces, and is present at thalweg depth or 0.5-1m in depth (Figure 3.25). The Radar facies 5 can also be seen filling in trough features (1-2m in depth) such as radar facies 4 (Figure 3.24).

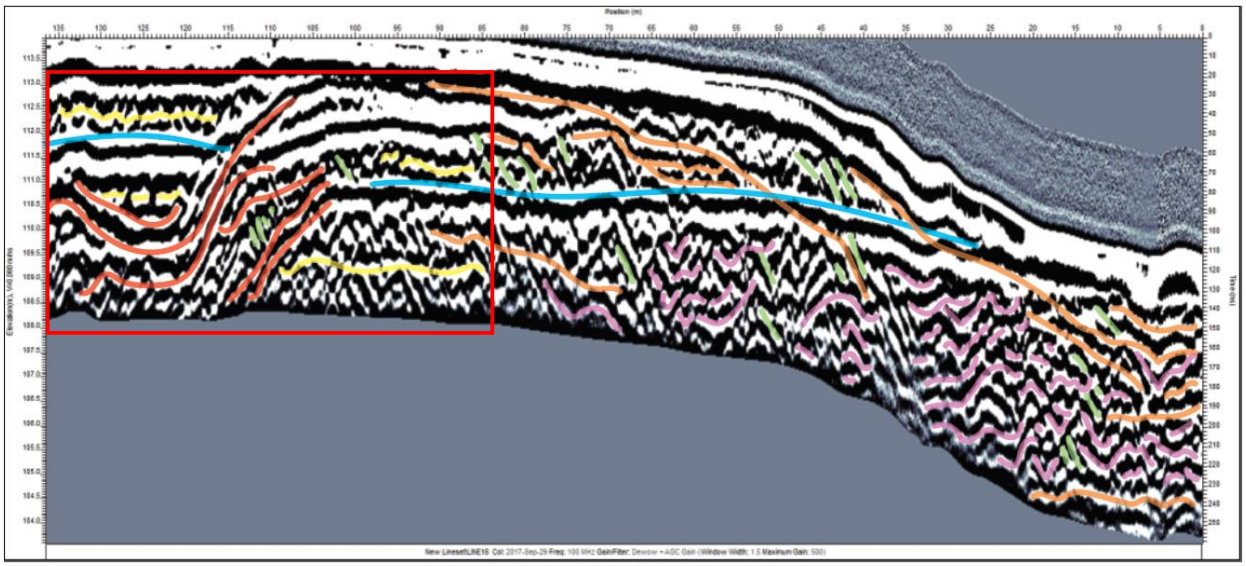

Figure 3.24: TB3-03DS: Downstream, transverse GPR profile on TB3. Example of radar facies 5, marked by yellow planar reflector. Location of GPR profile is shown in Figure 3.15.

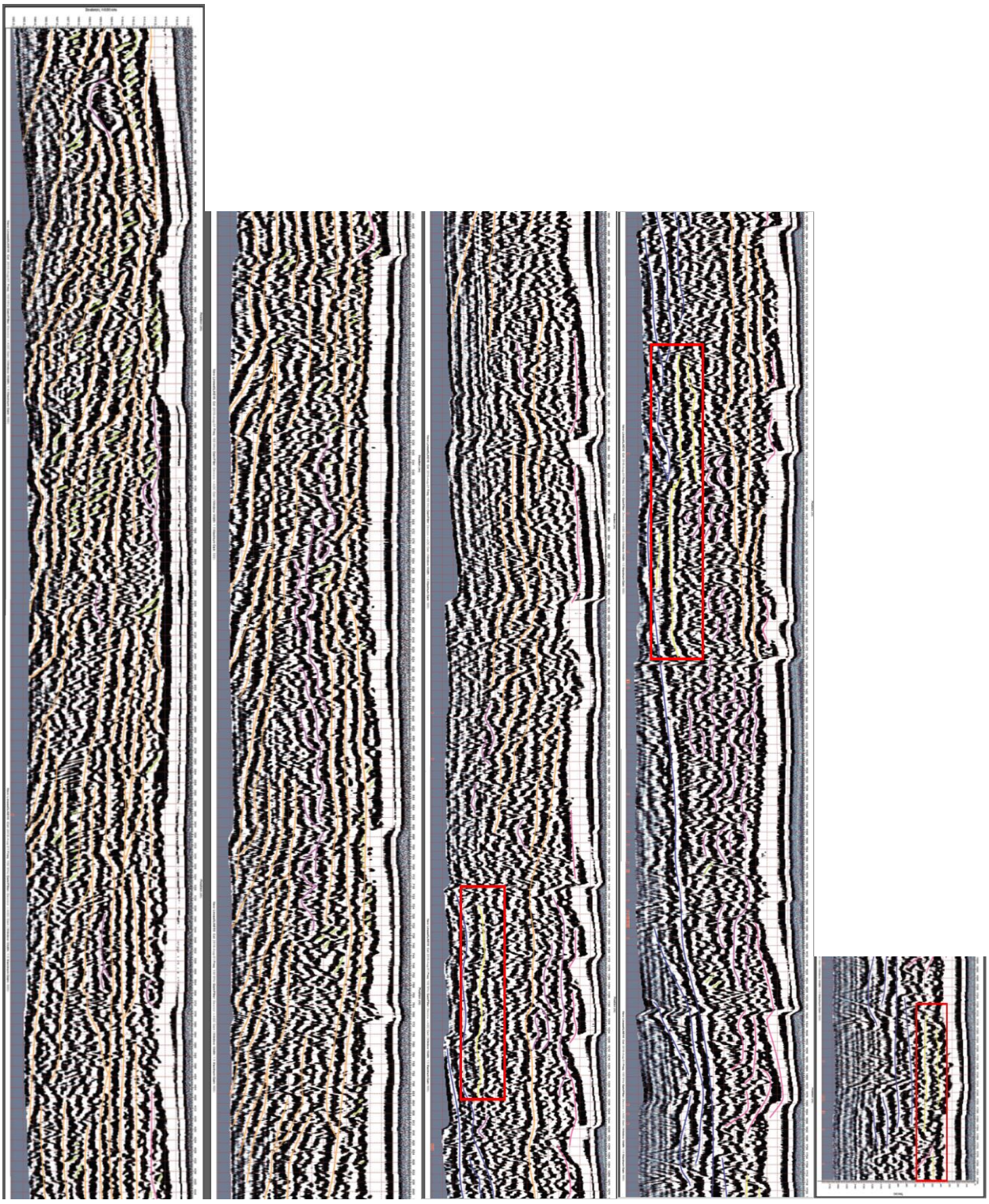

Figure 3.25: Maier-03Long: Longitudinal line from Maier showing radar facies 5 marked in yellow and highlighted by a red box, on the downstream end of the profile. Location labeled on Figure 3.14.

Interpretation:

Facies 5 are interpreted as sheets of gravel with any bedforms that are below the resolution of the GPR or planar depositional surfaces (Figure 3.25). This facies can be found at thalweg depth or at 0.5-1m (Figure 3.24).

Facies 6

Radar facies 6 comprises hyperbolae, which are hyperbolic arcs that represent reflective artifacts or buried objects in the point bar (Figure 3.18). The hyperbole are created by point reflectors, with the size of the arc depending on the size of the object. These features can appear at any depth of the profile and vary greatly in size.

Interpretation:

Facies 6 is interpreted as tree trunks, branches, rocks, or gravel that causes these hyperbolae to be present within the GPR profiles (Figure 3.18).

3.3.2 Geomorphological Interpretation of the GPR Data

Maier Bend is migrating and expanding northward, and shows very little translation downstream (Figure 3.1). This expansion of the point bar is reflected by the Facies 1 lateral accretion surfaces. When looking more closely at the transverse, upstream GPR profiles, the first few upstream lines show Facies 1a that is lateral accretion surfaces with small-scale features packaged in between the layers; but in transverse lines closer to the mid-bar, the small-scale features are no longer visible or limited to the channel side of the point bar (Figure 3.27). This could be because the upstream section of Maier Bend is medium gravel dominated (Rowley, 2020), causing the decrease in resolution of these smaller features

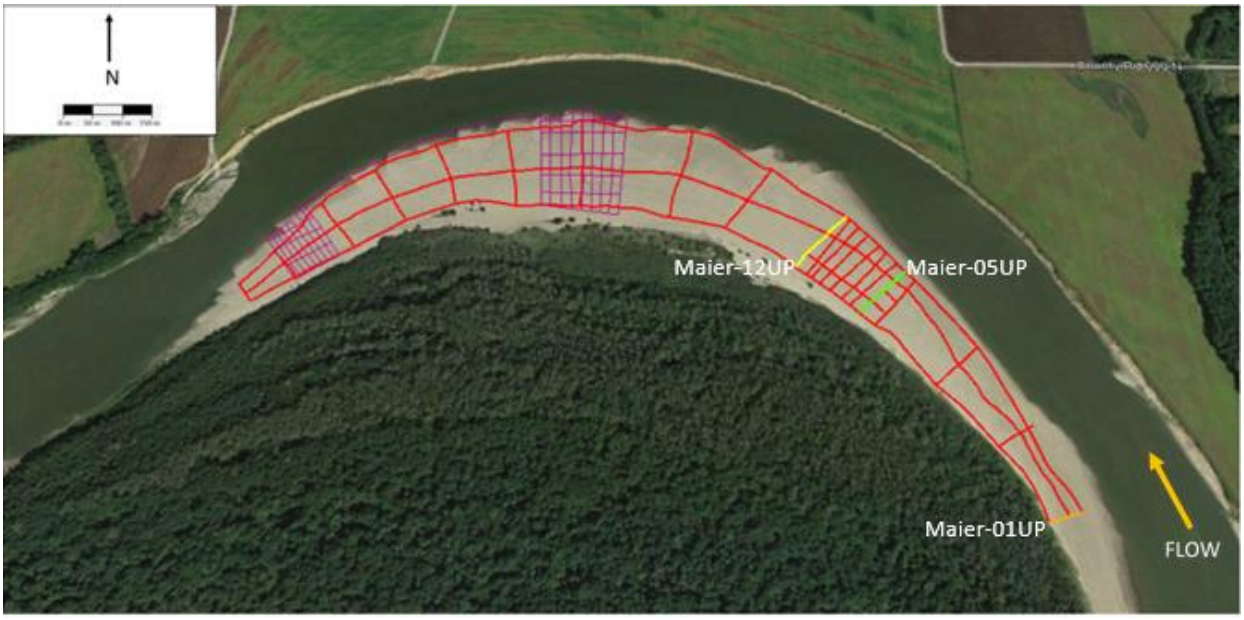

Figure 3.26: Location of the three following transverse lines for Maier Bend point bar: Maier-01UP (orange line), Maier-05UP (green line), and Maier-12UP (yellow line) in Figure 3.27.

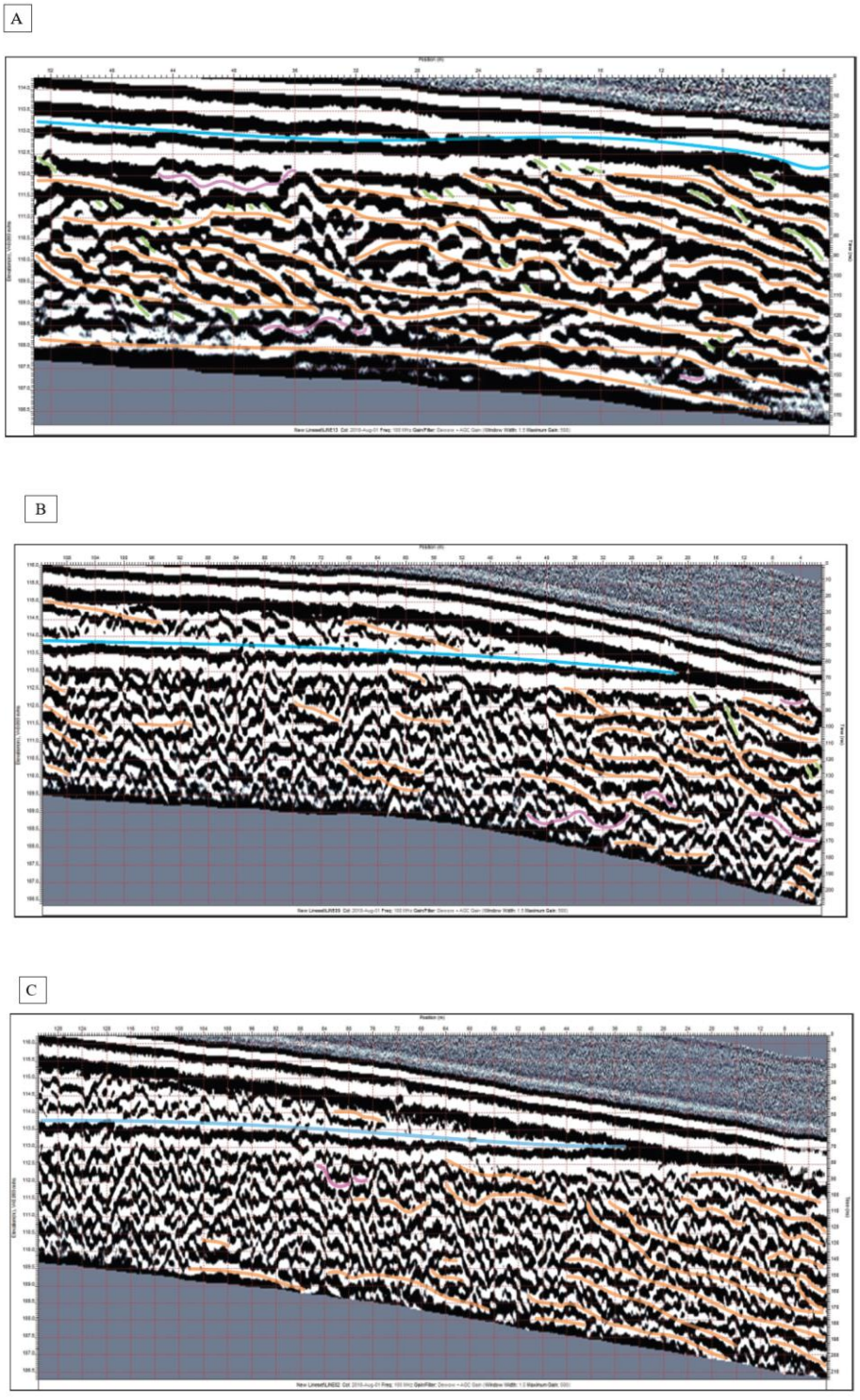

Figure 3.27: A (Maier-01UP), B (Maier-05UP), and C (Maier-12UP) all show Facies 1, lateral accretion. This lateral accretion allows the point bar to expand into the channel and the channel to migrate across the floodplain. Additionally, A, B, and C also show the decrease from Facies 1a (small scale features present) and the increase of Facies 1b (no small scale features). This is likely due to a decrease of resolution in the GPR because of the gravel present in the upstream end of the point bar. Location of these GPR profiles are labeled on Figure 3.26.

In addition to these low-angle lateral accretion surfaces, the GPR facies show high-angle unit bars that are migrating downstream. Such unit bars formed through several mechanisms. These unit bars (facies 2) are only seen at the downstream end of the Maier Bend at the transverse GPR lines (Figure 3.29). However, when the aerial imagery of the Maier point bar is examined (Figure 3.28), unit bars can be seen along the edge of the Maier point bar from approximately mid-bar to the downstream end of the bar. In longitudinal line Maier-03 Long (Figure 3.45), these unit bars are also visible within the mid-bar section. Maier-03Long (Figure 3.36) is the survey line closest to the thalweg side of the point bar. The reason that these are not visible in the transverse GPR lines is that these unit bars were not present when the GPR was conducted. Additionally, the unit bars are not seen on the interior of the bar in any of the profiles for Maier Bend. This could be due to the angle at which the surveys were taken. Another possibility is that these unit bars are eroded and are not well-preserved in the point bar.

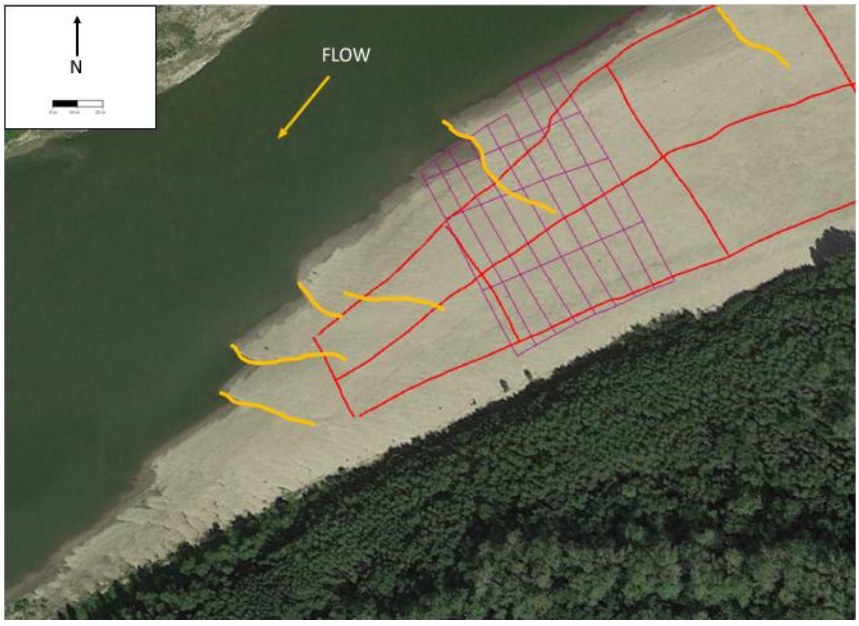

Figure 3.28: The base map is Maier Bend in 2013 from Google Earth. The red and purple lines represent GPR surveys taken on the point bar. The yellow lines outline unit bars that can be seen on the surface of the Maier Bend point bar.

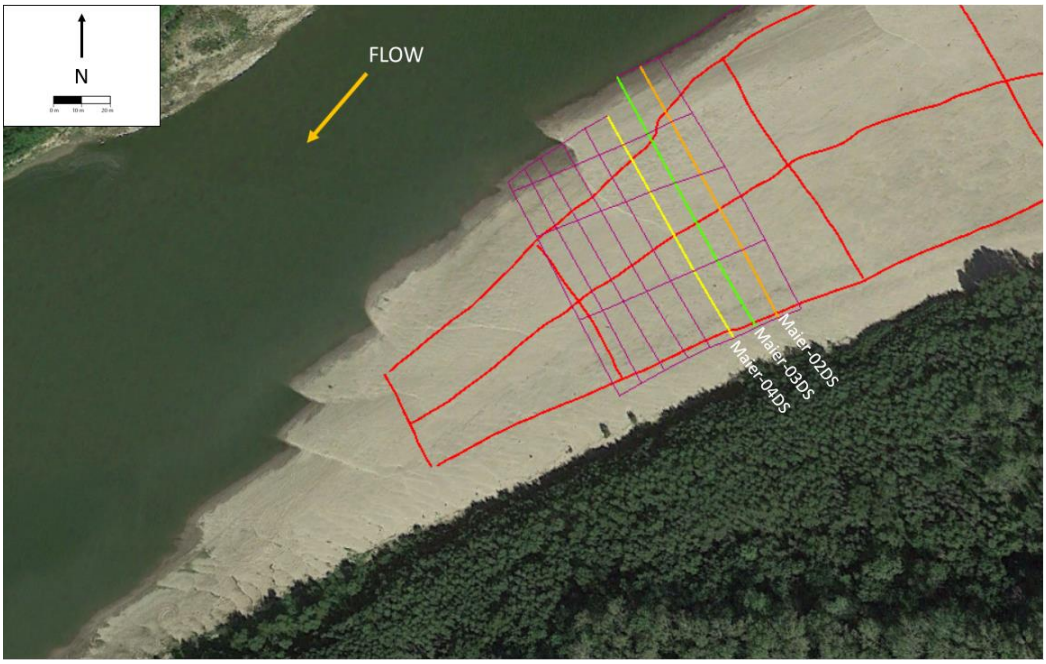

Figure 3.29: The base map is Maier Bend in 2013 from Google Earth. The orange (Maier-02DS), green (Maier-03DS), and yellow (Maier-04DS) lines represent the three transverse GPR lines that are displayed in the following figures. All three of these lines have Facies 2 present. These three GPR lines are all in close proximity to a unit bar.

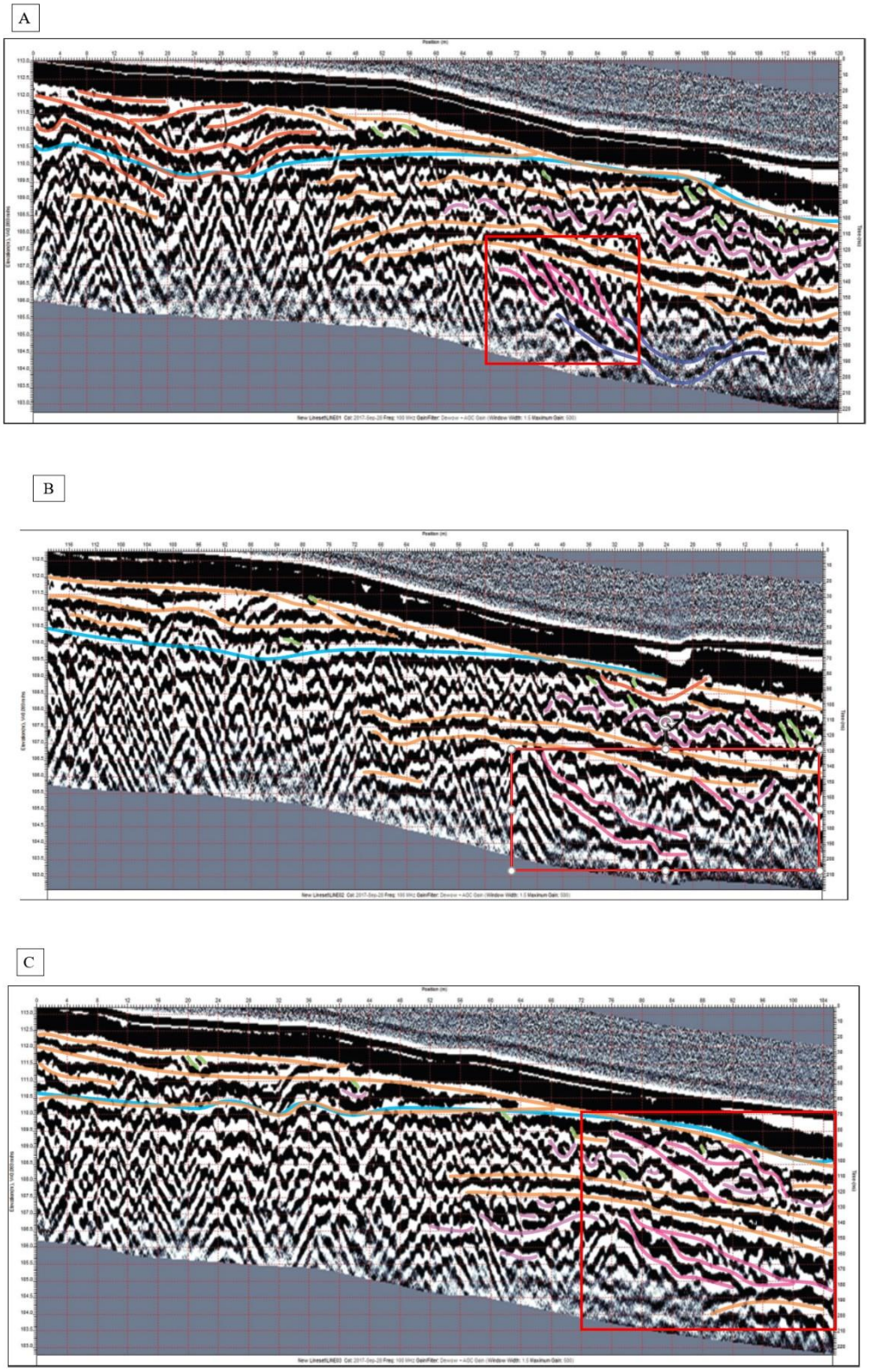

Figure 3.30: All three of these GPR profiles have unit bars present. Each are in close proximity of unit bars that were formerly present within the point bar. These unit bars are represented by pink lines in the profiles. **A:** GPR profile for orange line (Figure 3.29). Maier-02DS **B:** GPR profile for green line (Figure 3.29). Maier-03DS **C:** GPR profile for yellow line (Figure 3.29). Maier-04DS.

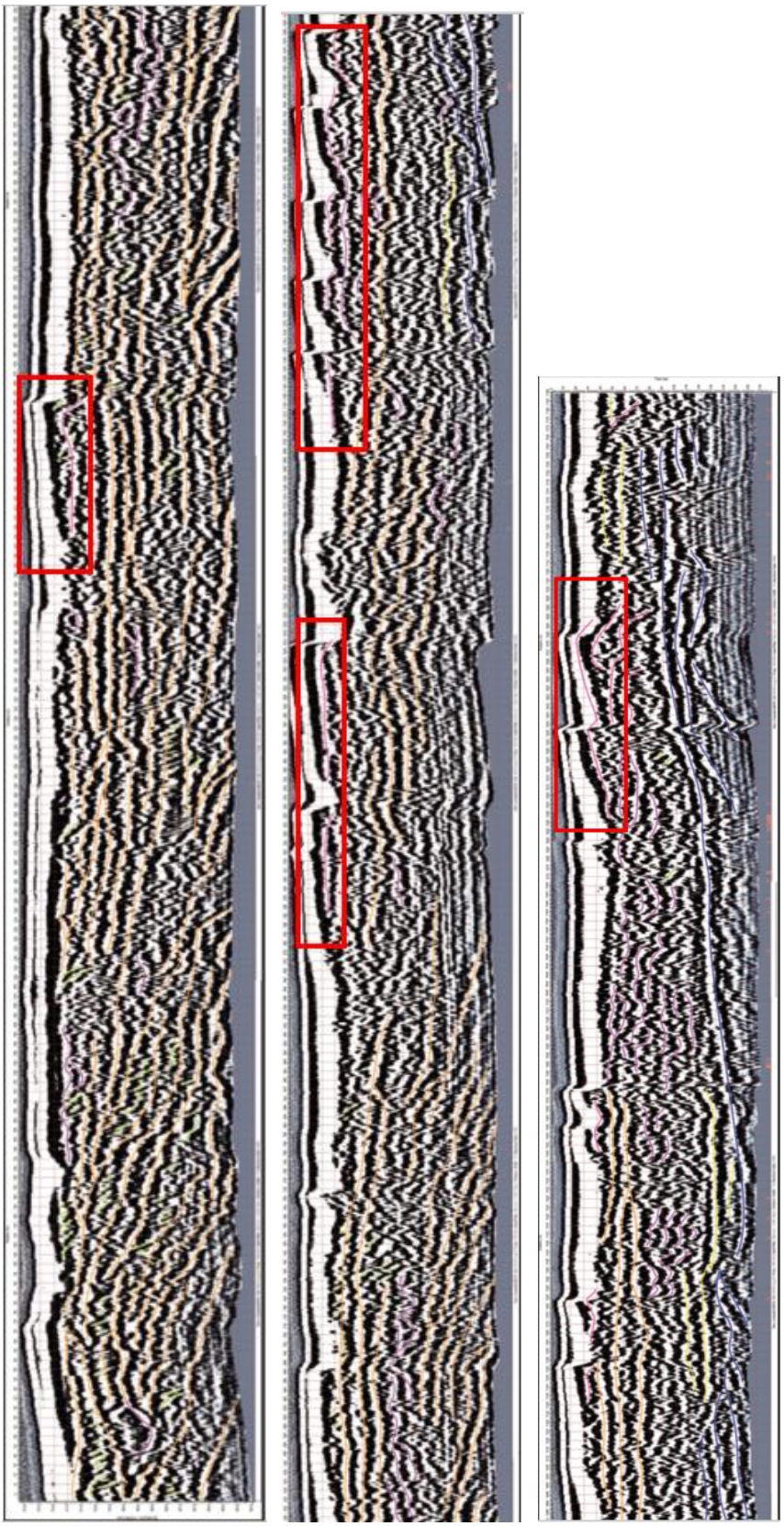

Figure 3.31: Maier-03Long: Longitudinal line from Maier Bend. Location marked in Figure 3.14. Marked by red boxes are unit bars seen at the surface of the point bar.

Dunes are abundant on the surface of the point bar as seen in the MBES survey taken in 2019 (Figures 3.3 and 3.6) within the channel. In the channel, the dunes are larger in size compared to the dunes on the point bar due to changes in flow depth (Figures 3.5; 3.8; 3.32). Within the GPR lines, dunes (Facies 3) are best seen in the mid-bar to downstream GPR lines (Figure 3.33). However, dunes are also seen on the upstream end of the Maier Bend point bar, but due to the upstream end of the point bar being gravel rich, the resolution of the GPR may not be sufficient to image these dunes. The dunes may also be incorporated between the lateral accretion surfaces described in Facies 1a (Figure 3.18).

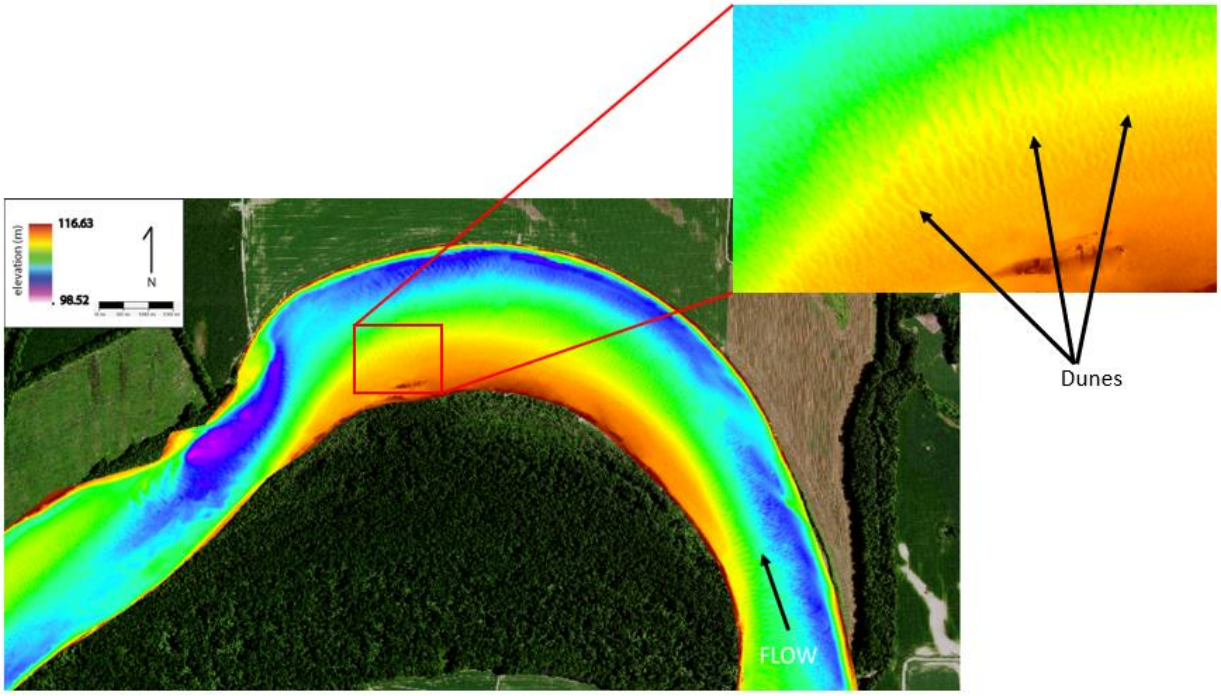

Figure 3.32: MBES taken in 2019, showing dunes present on the downstream end of the Maier Bend point bar. The dunes (Facies 3) are seen mostly in the downstream end of the GPR lines (both transverse and longitudinal). The dunes increase in size from the point bar to the channel.

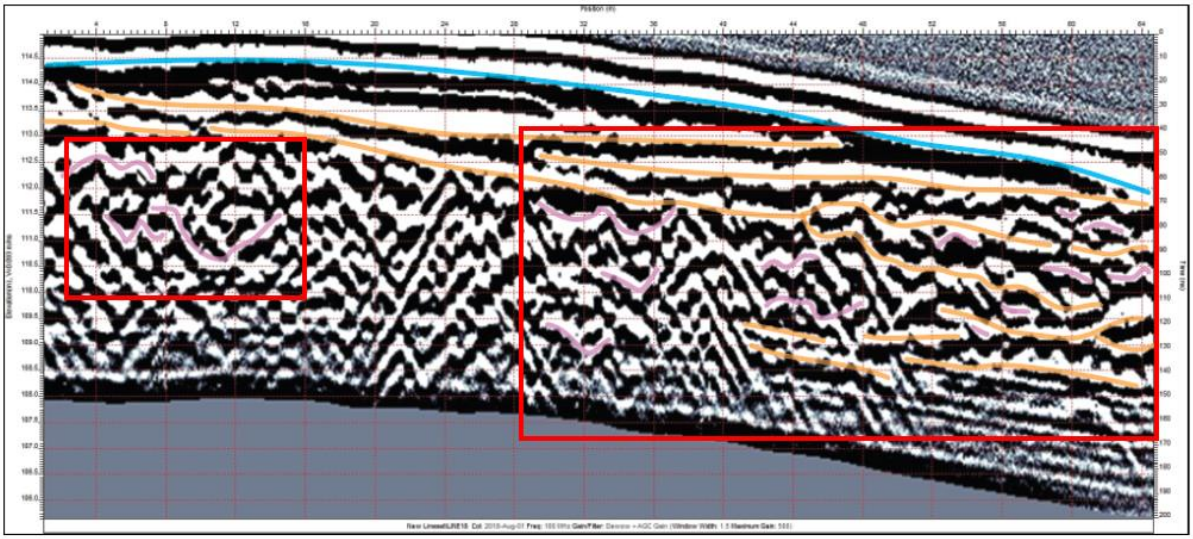

Figure 3.33: Maier Bend downstream line (Maier-09DS), showing dunes found in the interior of the bar and closer to thalweg (red box on the left). Additionally, there are dunes are also seen packaged in between lateral accretion surfaces (refer to box on the right. Orange lines are interpreted as lateral accretion surfaces and the purple are interpreted as dunes).

In the downstream transverse lines, trough features seen near the surface of the point bar (Facies 4; Figure 3.36) are interpreted as a bar top hollow. Bar top hollows form as bar-tail accretion occurs as the point bar wraps around the bend during migration. As a result, a 'hollow' is created due to a lack of deposition closest to the inner bank of the point bar (Best et al., 2006). In Maier bend, the bar top hollow is no longer visible, but can be seen in aerial imagery in 2008 (Figure 3.34). At some point before 2011, this hollow was subsequently filled by deposition.

Figure 3.34: Maier Bend point bar in 2008. At the downstream end, there is a bar top hollow visible and that was later filled sometime before 2011. The bar top hollow can be seen preserved in the GPR profile (Maier-11DS).

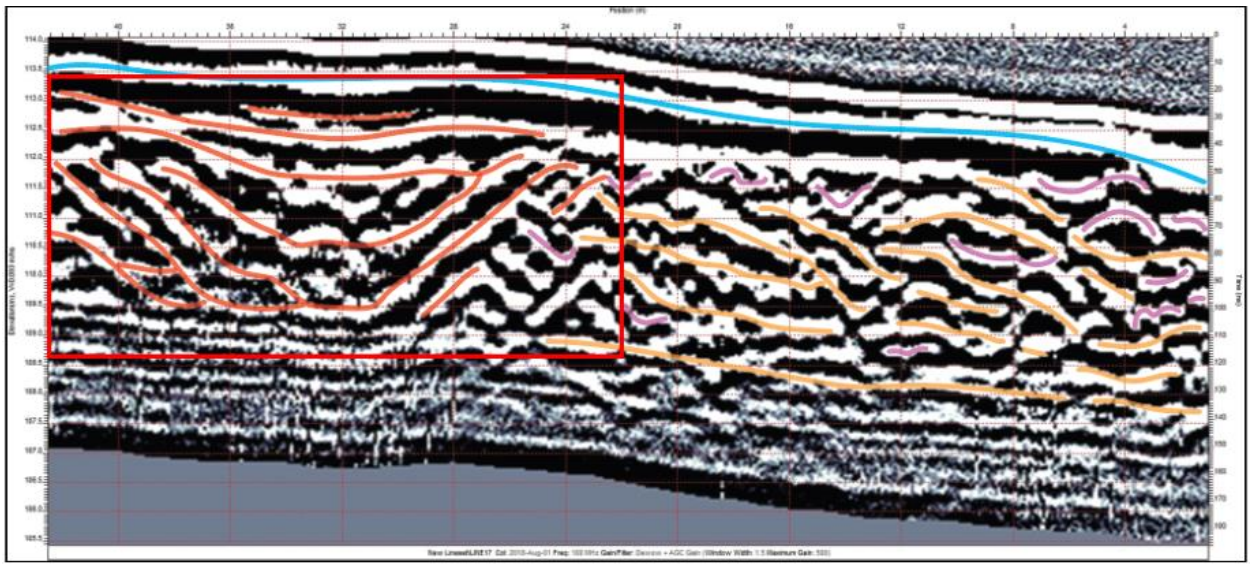

Figure 3.35: Bar top hollow within the GPR profile (Maier-11DS) on the downstream end of the Maier Bend point bar. The bar top hollow is on the interior side of the point bar in the transverse line [refer to red lines within red box on left].

TB3 also exhibits all six facies described in Table 3.1, with the most abundant facies being Facies 1 that represents lateral accretion surfaces. Figure 3.2 shows TB3 is translating downstream as well as expanding into the floodplain, and that larger increments of point bar deposition are produced on the downstream part of the point bar. At the mid-bar and downstream end of the bar, lateral accretion surfaces and/or unit bars are present as the TB3 point bar has migrated downstream.

Similar to Maier Bend, the TB3 point bar also has unit bars migrating downstream, and are also absent on the interior of the bar despite having been present from the interior to the channel side in the aerial photos (Figure 3.36). In transverse lines, unit bars are only visible on the thalweg side of the point bar (Figure 3.37). Furthermore, the unit bars are only present in the longitudinal line closest to the thalweg on TB3 (Figure 3.36), and may become interbedded with the lateral accretion surfaces over time.

Figure 3.36: Unit bars located on TB3 marked in red. Image is from 2013.

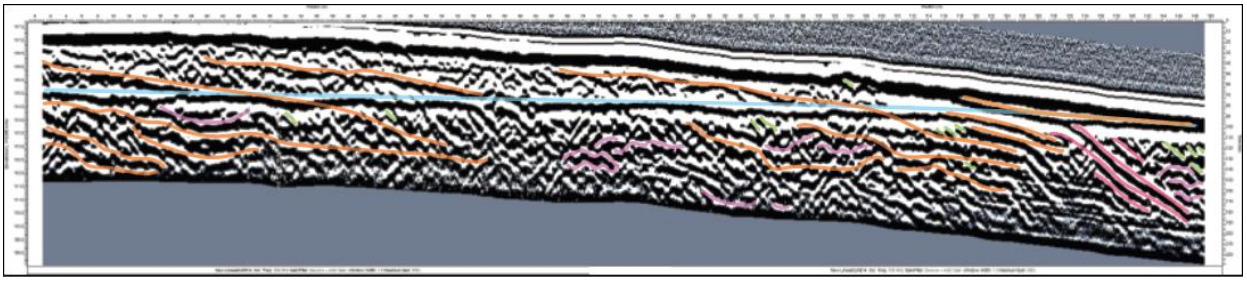

Figure 3.37: TB3-07Mid: Mid-bar, transverse GPR profile. Interpreted unit bars (Facies 2) marked in pink on the thalweg (right) side of the transverse GPR profile. Location of the GPR profile is labeled on Figure 3.15.

Within the transverse lines on TB3, dunes are primarily present at the downstream end of the point bar (Figure 3.38). However, the MBES bathymetry of TB3 (Figures 3.6) reveals dunes can be seen throughout the point bar, although they may be too small for the resolution of the GPR. Another possibility is that these dunes are in between the lateral accretion surfaces and are incorporated into Facies 1a. In addition to the dunes on the point bar, dunes can also be seen within the channel. When looking at the GPR profiles, the dunes can be seen on the channel side along with the interior of the point bar (Figure 3.32).

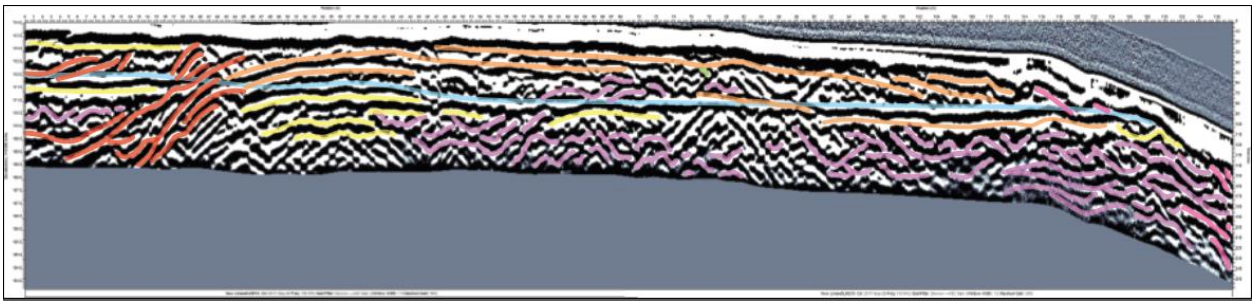

Figure 3.38: TB3-02DS: The dunes (marked in purple) are seen on both the interior and thalweg side of the GPR profile. On the interior of the point bar, a bar top hollow (marked in red; Figure 3.13) that has been filled with both planar bedding (marked in yellow) and dunes. Location of the GPR profile is labeled on Figure 3.15.

At the tail end of the TB3 point bar, there is a depression that can be seen on both the surface (Figure 3.13) as well as within the transverse GPR profiles (Figure 3.38). As the TB3 point bar continues to translate downstream, this bar top hollow is filled with planar deposition (Facies 5; Figure 3.38) and/or subsequent lateral accretion.

3.4 Facies Quantification

3.4.1 Quantification of Facies within GPR Lines

After identifying the radar facies and their geomorphic/sedimentological interpretation, they were quantified by creating a 4m by 0.5m grid for the profiles and averaging the total percentage of facies at every 4m interval. The most abundant facies for both point bars is Facies 1, with Facies 1a and 1b comprising 50% or more of the total facies. However, the quantification shows a decrease in abundance of Facies 1 from upstream to downstream (Figure 3.39), but there is an increase in all other facies. This also appears to correspond to the change in grain size (Rowley, 2020) from upstream section to the downstream end of the point bar.

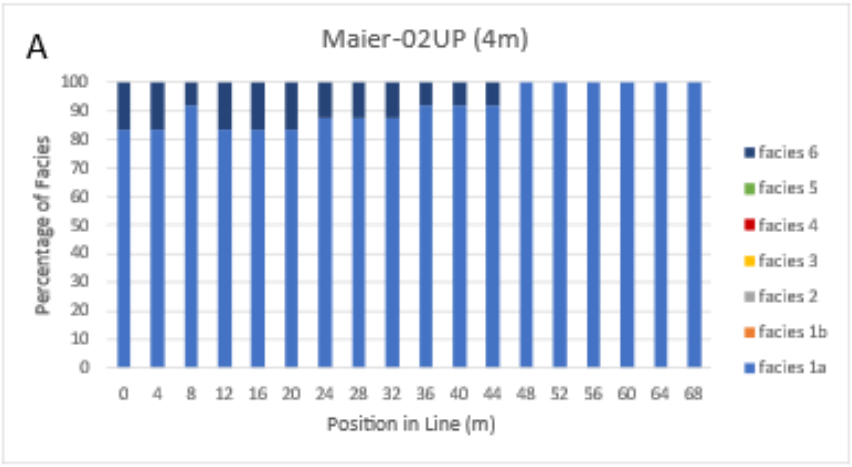

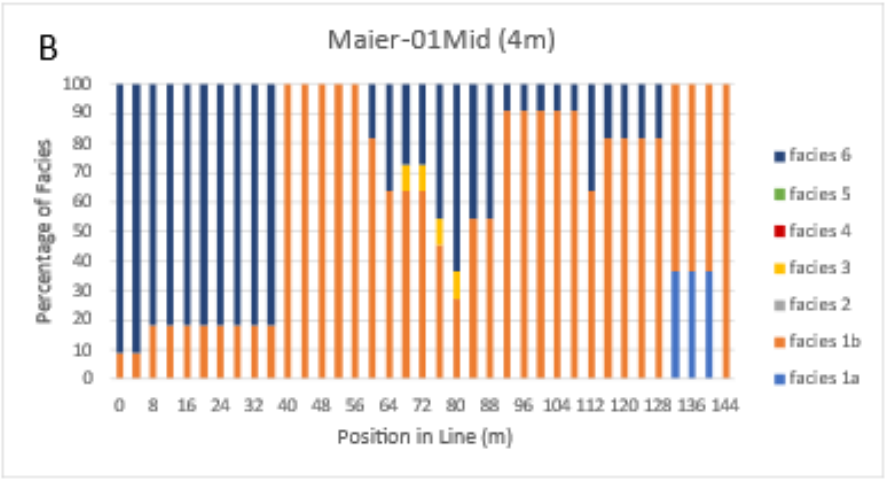

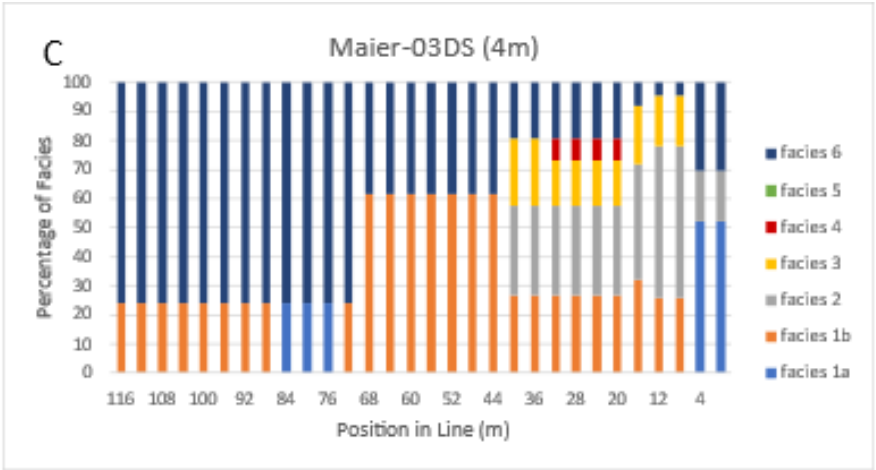

Figure 3.39: Transverse profiles of Maier and TB3 point bars. Left to right is interior of bar to thalweg side. **A-C:** Maier Bend point bar facies percentage profiles from upstream to downstream to show decrease in Facies 1 and an increase of the other facies. **D-F:** TB3 point bar abundancy profiles from upstream to downstream to show decrease in Facies 1 and an increase of the other facies. TB3 does not see a significant change until the profiles reach the downstream end.

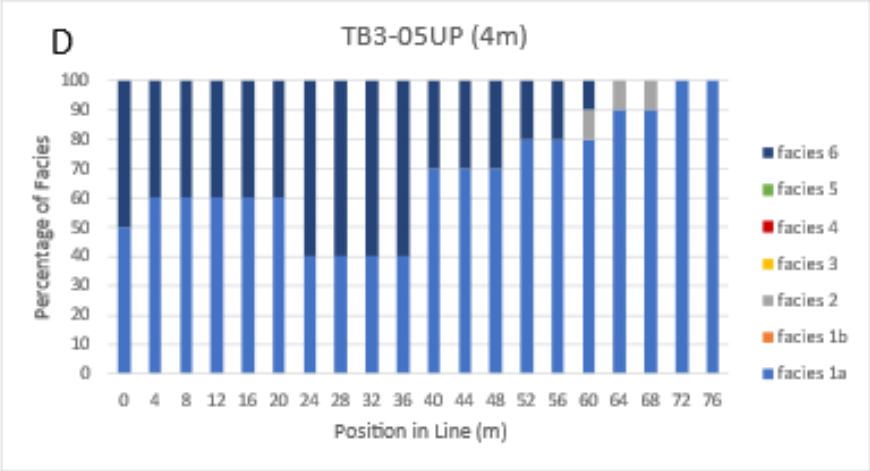

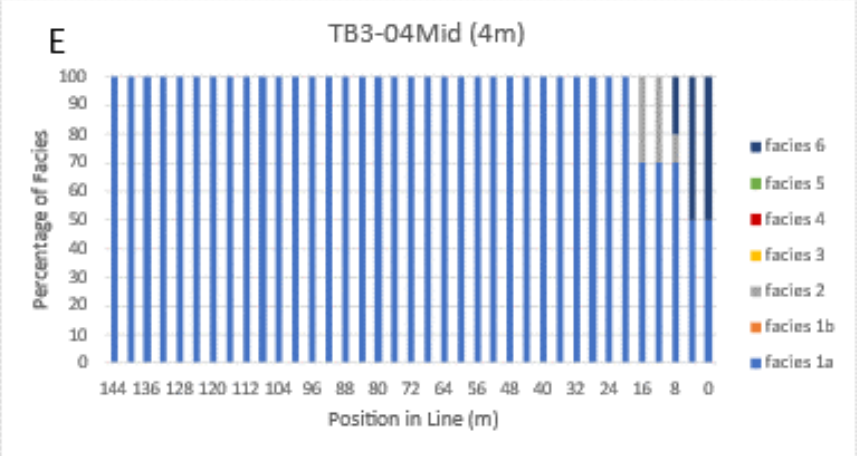

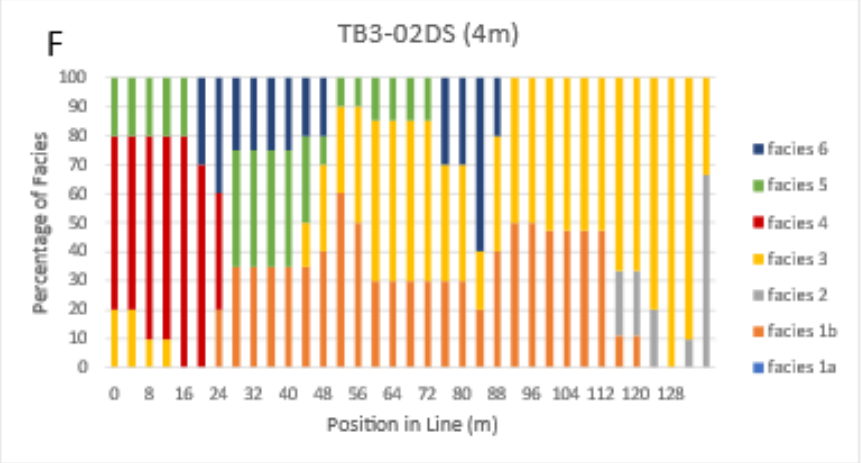

[Figure 3.39 cont.]

Facies 6 is also abundant, especially in the gravel-dominated upstream section of the point bar that would cause the abundance in hyperbola. Facies 6 abundance ranges from 10-50%, depending on the point bar (Figure 3.39). This variation can be due to several factors. One reason is likely due to a decrease in gravel from upstream to downstream. The abundance of hyperbola is also caused by the resolution and quality of the GPR surveys. Lastly, the amount of tree debris present within the bar will also affect the abundance of Facies 6 within the profiles.

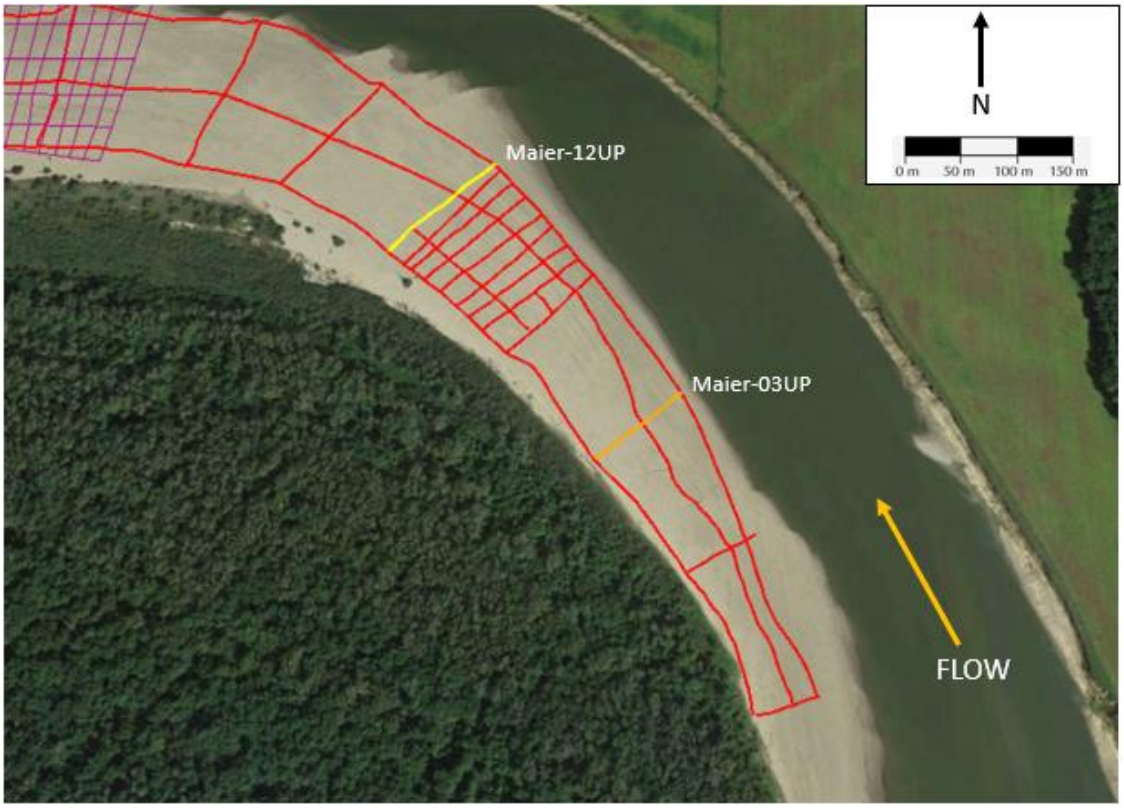

Figure 3.40: Location of the percentage profiles on the upstream end of Maier. Maier-03 UP is marked by the orange line. Maier-12UP is marked by the yellow line.

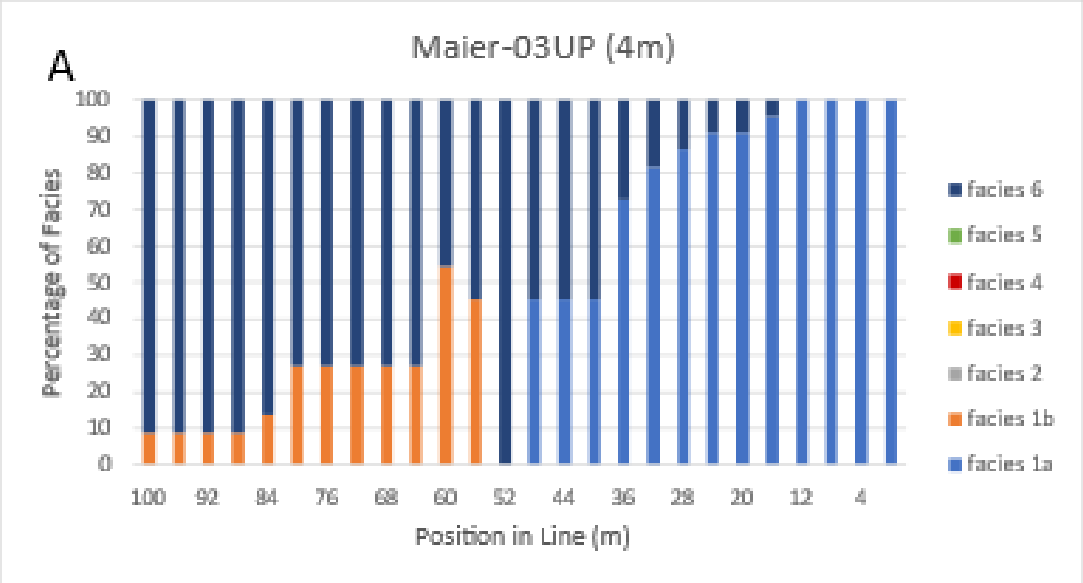

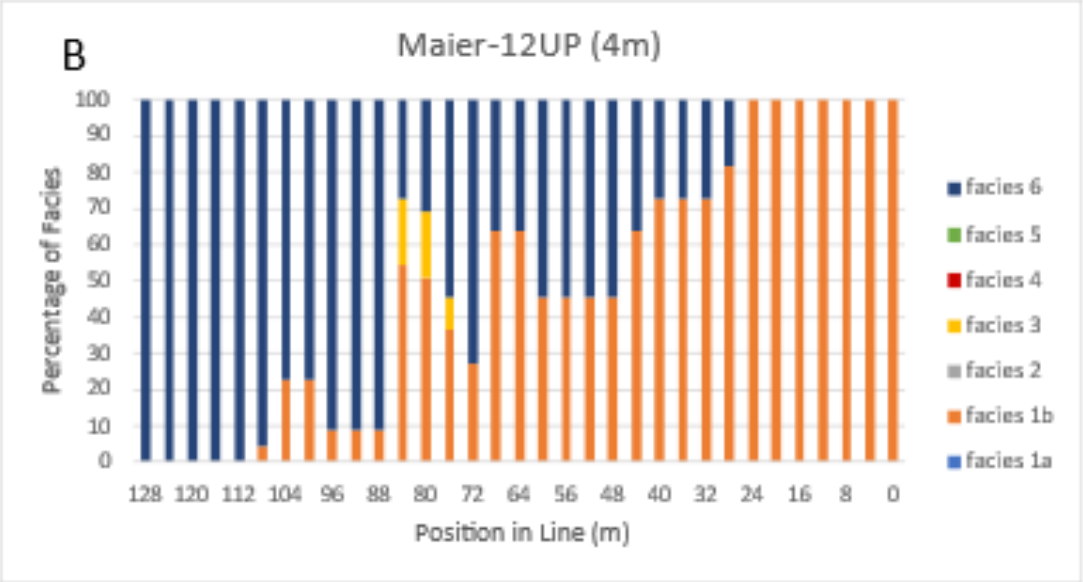

Figure 3.41: A: Maier-03UP **B:** Maier-12UP **A&B:** Left to right is interior of point bar to channel side. Both the percentage profiles show the abundance of Facies 6. Facies 6 percentage is high in both upstream, transverse profiles. Locations shown in Figure 3.40.

The least abundant facies are Facies 2 (unit bars) and 5 (gravel sheets) with Facies 2 being limited to the mid-bar to downstream sections of the point bars. Facies 2 ranged from 0 to 3% in abundance. Facies 5 had *c.*0-5 % abundance, with Facies 5 usually only present at thalweg depth, or filling depressions in the GPR profiles.

Facies 3 (dunes) varies in abundance between Maier and TB3 bends, from 0-22%. Additionally, Facies 3 abundance increases from upstream to downstream (0-9% average for Maier bend and TB3), seen in the longitudinal lines (Figure 3.42).

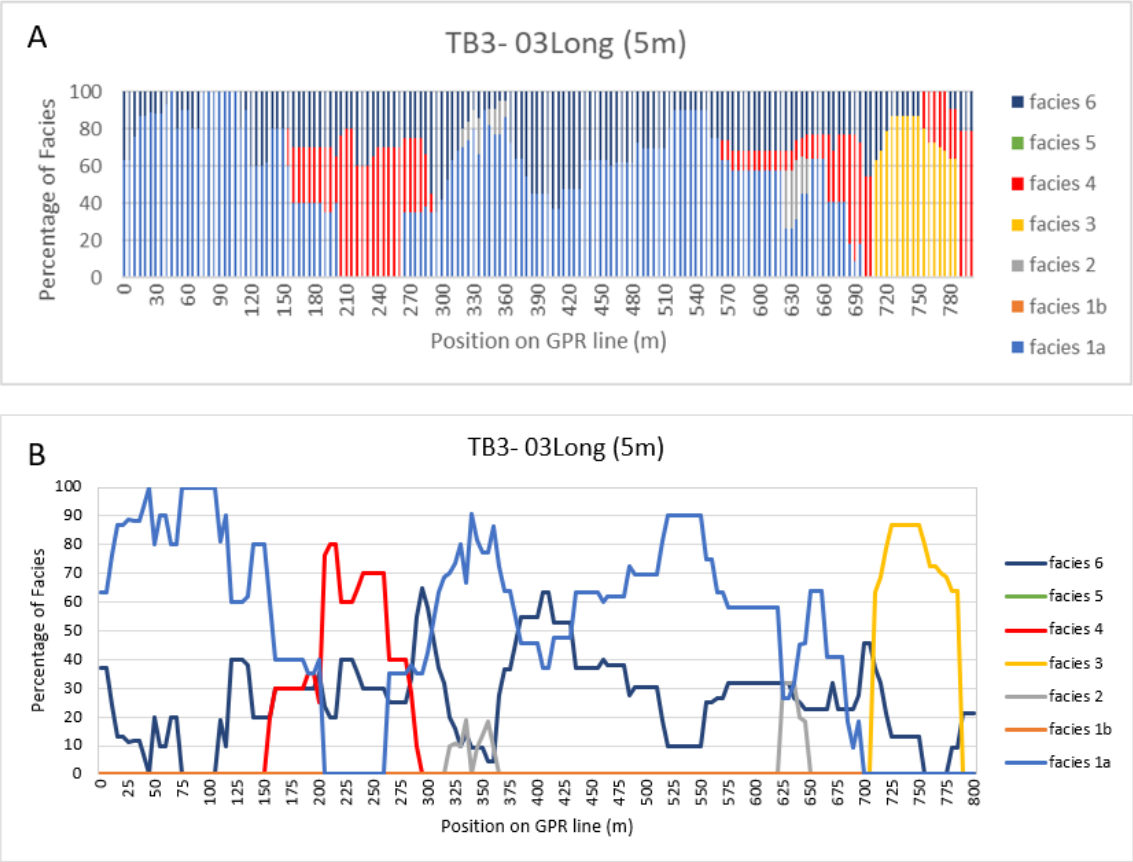

Figure 3.42: TB3-03Long: A: Percentage of facies for longitudinal line of TB3 on the channel side. Left to right is upstream to downstream. Location is marked in Figure 3.15.**B:** Line chart showing the data as A**.**

The abundance of Facies 4 increases from upstream to downstream. Facies 4 (bar top hollows) occurs from the upstream to downstream sections (Figures 3.39 and 3.42), due to bar top hollows being primarily found at the mid-bar to tail end sections of the point bar.

3.4.2 Comparison of Facies Abundance between Maier Bend and TB3

All six facies are present within Maier and TB3 bends. In both Maier and TB3 point bars, Facies 1 (lateral accretion surfaces) is the most abundant facies. However, Facies 1b (Figure

3.39) is more abundant in the Maier Bend point bar. The grain size of the sediment within the Maier Bend makes it more difficult for the GPR to survey the small scale features seen within Facies 1a. In TB3, Facies 1a (Figure 3.39) is the most abundant, ranging from 50-90% in abundance. Within both point bars, Facies 1 decreases in abundance from upstream to downstream (Figure 3.39).

Facies 2 (unit bar) is only seen in the downstream end of the transverse lines in Maier (Figure 3.43). However, in the longitudinal line of the Maier Bend point bar, Facies 2 is present not only on the downstream end, but also, in the mid-bar sections (Figure 3.45). In TB3, Facies 2 can be seen from upstream to downstream transverse lines (Figure 3.39).

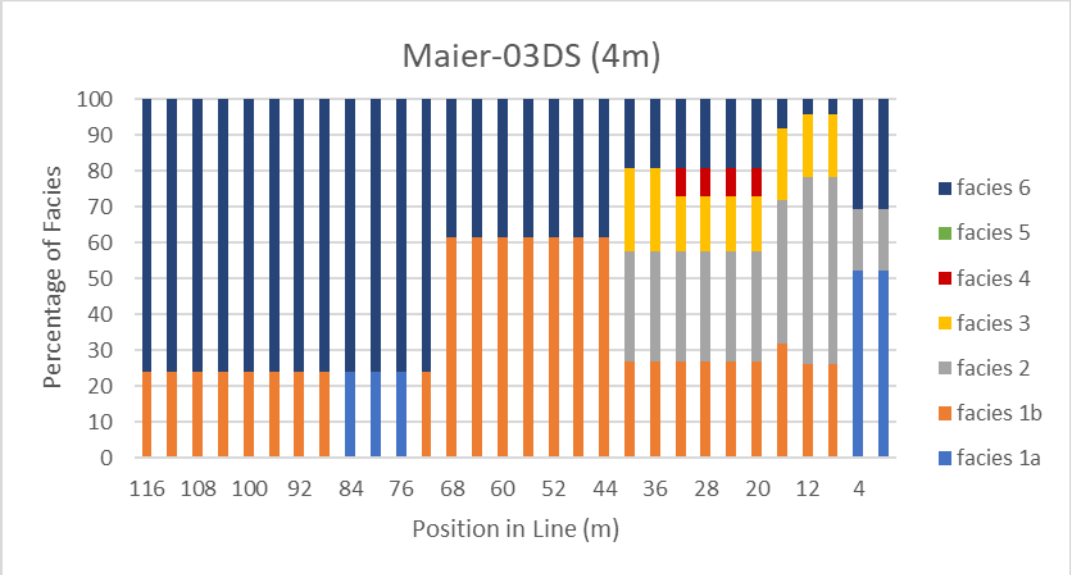

Figure 3.43: Maier-03DS: Downstream, transverse percentage profile. It highlights the unit bars that are seen within the downstream end of the Maier Bend point bar. Left to right is interior of the bar to channel side.

TB3 has a significant increase in Facies 3(dunes) from the upstream to downstream lines, with its abundance averaging 3% to 21% (Figure 3.41). Maier Bend has a slight increase (Figure 3.44) in the number of dunes present (averaging 0.14 % to 2.63 %), but not as great as TB3.

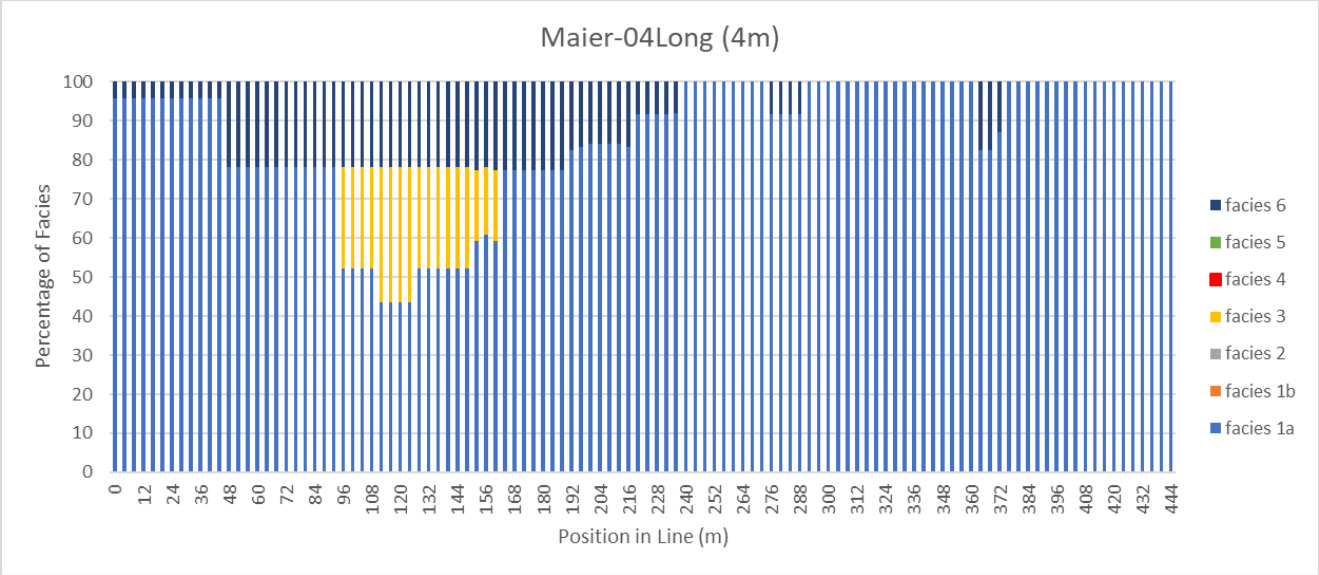

Figure 3.44: Maier-04Long: Facies percentage chart for a longitudinal GPR profile on Maier Bend, showing a slight increase in dune presence at the mid-bar/downstream section of the point bar. Left to right is upstream to downstream. Location of profile on Figure 3.14.

In both Maier Bend and TB3, there is an increase in Facies 4 (bar top hollow) from upstream to downstream. TB3 has more Facies 4 present because of the significant size of the bar top hollow that is present at the bar tail (Figure 3.39). Maier Bend also has bar top hollow structures in some of the downstream GPR profiles, but it may not be as well preserved as the Maier Bend point bar migrated more laterally than TB3.

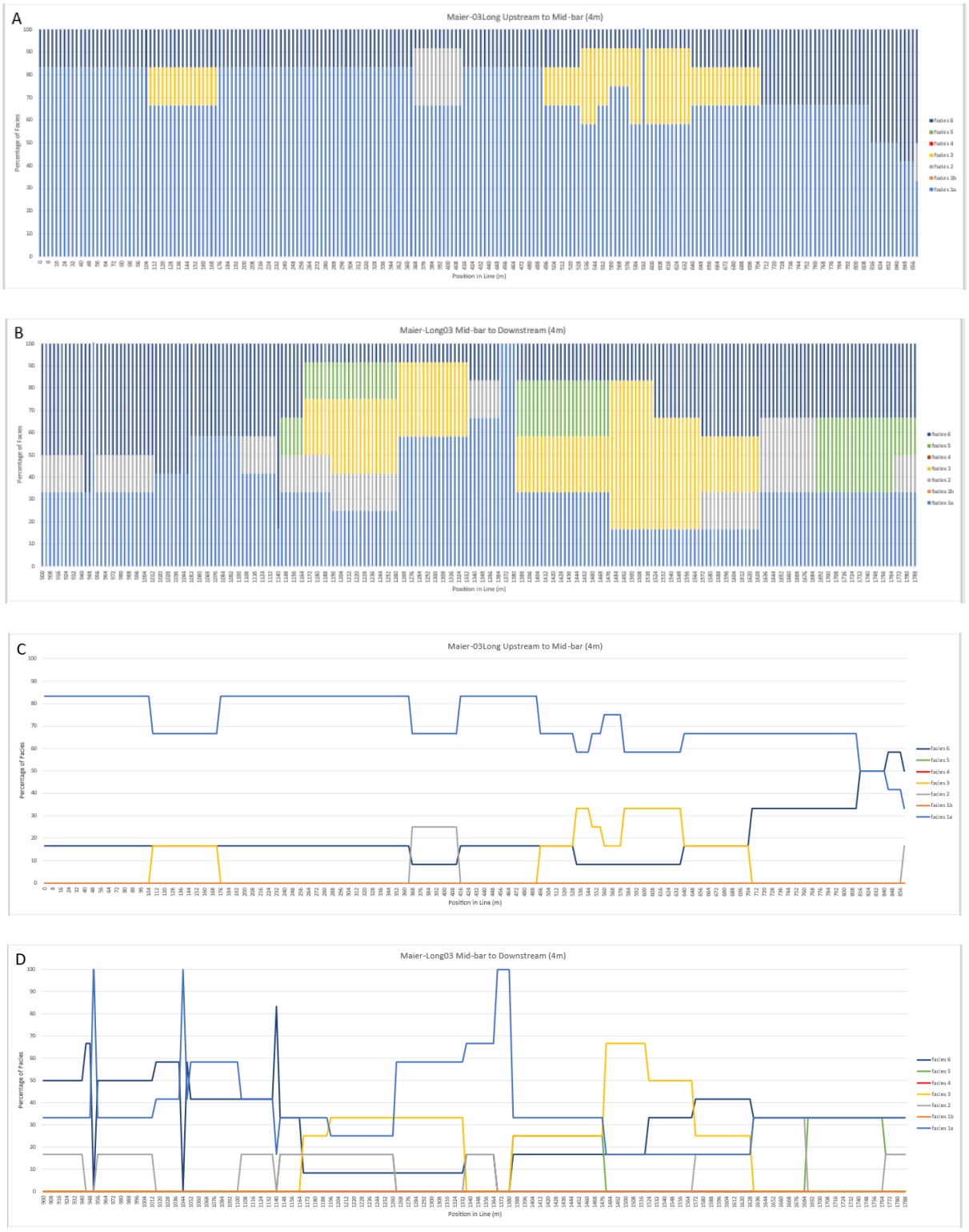

Figure 3.45: Longitudinal line of Maier Bend point bar (Maier-03Long). percentage profile closest to the channel showing the upstream to downstream quantification of the facies. Left to right is upstream to downstream. **A:** Profile for the upstream to mid-bar section of the point bar. **B:** Mid-bar to downstream section of the point bar. **C&D:** Line charts showing the same data as A and B.

Facies 5 (planar deposition) is not seen at all in the Maier Bend transverse lines, but can be seen in the longitudinal lines (Figure 3.45). In both bends, Facies 5 increases from upstream to downstream. TB3 has an increase in Facies 5 from an average to 0-5 %. However, for TB3, Facies 5 is only present in the downstream, transverse lines (Figure 3.39).

Facies 6 (hyperbolae) is abundant in both the Maier Bend and TB3 point bars. This is because the hyperbolae are not necessarily dependent on the depositional environment in which the other facies were created. Instead, the abundance of Facies 6 is dependent on the number of point reflectors that can cause interference on the GPR panels. These point reflectors (hyperbolae) can be caused by changes in grain size such as an increase in the abundance of gravel. Also, the point reflectors can also be caused by buried trees or branches. There are much fewer hyperbolae represent in TB3, averaging 7-15 %. In Maier Bend, there are more hyperbolae present (Figure 3.39), suggesting that there are more elements (gravels, trees) causing these point reflectors. The number of hyperbolae present ranges from 35-45 % in the Maier Bend point bar.

CHAPTER 4: DISCUSSION AND CONCLUSIONS

4.1 Introduction

Meandering rivers are abundant in nature and important to the environment by providing resources for humans and many other organisms (Ward and Stanford, 1995; Nagayama and Nakamura, 2018). In addition, meandering rivers play a major role in shaping the surrounding landscape and in the transport of sediment, developing features such as point bars. Point bars affect the morphology and flow within the channel, and thus sedimentation within the bends. Furthermore, point bar deposits make up an important component of ancient alluvium, and therefore it is important to understand the preservation of these features (Ghinassi et al., 2014). Point bars have been found to undergo different styles of migration and past studies have proposed that these different migration styles influence the sediments preserved (Jackson, 1976a; Willis, 1993; Ghinassi et al., 2014).

The objectives of the present research were accomplished through the processing, analysis, and quantification of aerial imagery, GPR profiles, and MBES data. Two point bars on the Wabash River, IL/IN, with different styles of migration (TB3 and Maier bend) served as the study sites for this research. A facies scheme was developed based on the analysis of longitudinal and transverse GPR transects that aimed to provide a framework for the facies that should be expected in bends with different modes of migration. This facies scheme also allowed quantification of the percentage of facies within the GPR profiles of the two bends. The results from these two contrasting bends were compared to examine the common or differing distinguishing features between them. This thesis posed three principal questions that are reviewed in this chapter.

Q1.) What sedimentary facies characterize bends with different styles of migration?

Both Maier and TB3 bends exhibited all six facies (Figure 4.1) defined in Table 3.1. These facies are interpreted as: lateral accretion surfaces that sometimes have visible small-scale sedimentary features (Facies 1a and b), unit bars (Facies 2), dunes (Facies 3), bar top hollows (Facies 4), planar deposition (Facies 5), and hyperbolae (Facies 6).

The lateral accretion surfaces form as sediment is deposited on the point bar. In Facies 1a, small-scale sedimentary features such as dunes can be seen packaged between the accretion surfaces. Facies 1b also consists of lateral accretion surfaces, but no small-scale features are visible, which is likely because these features are too small for the resolution of the GPR. Facies 2 is initiated through the unsteadiness of flow or sediment flux (Jopling, 1966; Smith, 1971; Lunt & Bridge, 2007) and form through a combination of vertical, lateral, and downstream accretion (Herbert et al., 2019). Facies 3 forms when fluid flow causes moderate shear stresses on a riverbed mobilizes bedload sediment transport that then forms dunes (Facies 3). Dunes migrate downstream as grains are transported up and over the stoss side of the dune. Facies 4 forms as the tail end of the point bar wraps around the bend, leaving a depositional low on the interior of the bed (Best et al., 2006). Facies 5 forms when gravel is deposited in sheets at thalweg depth, or when sediment is deposited and fills scours or bar top hollows. Facies 6 are point reflectors found in GPR profiles and are created when the EM signal reflects off an object in the subsurface like a rock or tree limb.

Although the type of facies did not change between the two bends, distinct differences were present in the abundance of facies in each bend depending on the style of migration. Facies 1 overall was the dominant facies within both bends (light blue in Figure 4.1), but one distinguishing characteristic between Maier and TB3 is the difference in abundance of facies 1a

and 1b (lateral accretion surfaces). Facies 1b with lateral accretion surfaces, but lacking the small-scale features, were more common in Maier Bend. However, this is less likely due to differences in bend migration style and more likely due to grain size differences and the angle at which the GPR surveys were taken.

In TB3, Facies 2 (unit bars) are found in TB3 more frequently in comparison to Maier Bend (light gray in Figure 4.1). In Maier Bend, the highest percentage of Facies 2 only reached an average of 0.14-2.63%, whereas TB3 reaches an average up to 21%. The higher abundance of Facies 2 could be a distinguishing characteristic for a translating bend like TB3. This abundance may be due to more sediment being transported from upstream to downstream within the point bar in TB3 as the bend translates downstream.

Facies 3 (dunes) increases in abundance from upstream to downstream in both Maier bend and TB3 (yellow in Figure 4.1). This is likely due to a change in grain size from upstream to downstream, making it more visible resolution-wise in the GPR profiles. TB3 has a higher abundance of Facies 3 compared to Maier Bend which be due to Maier Bend having a higher gravel content compared to TB3 (Jackson, 1976a), affecting the resolution at which the dunes can be seen within the GPR profiles. The higher abundance could also be due to how TB3 migrates. More sediment is being moved downstream in TB3; therefore, there is a greater opportunity for dunes to form on the TB3 point bar.

In TB3, there is also a greater abundance of Facies 4 (bar top hollows) compared to Maier Bend (red in Figure 4.1). This is likely due to TB3 translating downstream allowing a more prominent bar top hollow to form as the tail end wraps around the bend. Facies 4 is also present in Maier, but the bar top hollow is not as distinct, likely because of the lesser degree of downstream migration, accretion and preservation of the downstream part of the bend.

Facies 5 has low abundance in both point bars and is the least abundant of all the facies quantified in this thesis. The lack of Facies 5 abundance is likely due to it mostly being found towards thalweg depth (green in Figure 4.1) where the resolution of the GPR profiles decreases and makes it more difficult to interpret.

Facies 6 is abundant in all profiles (dark blue in Figure 4.1). However, there is a higher abundance within the Maier Bend point bar compared to the TB3 point bar. Maier Bend has a higher gravel content, especially at the upstream end of the point bar, which increases the chance of point reflectors (hyperbolae) that could occur within the profiles.

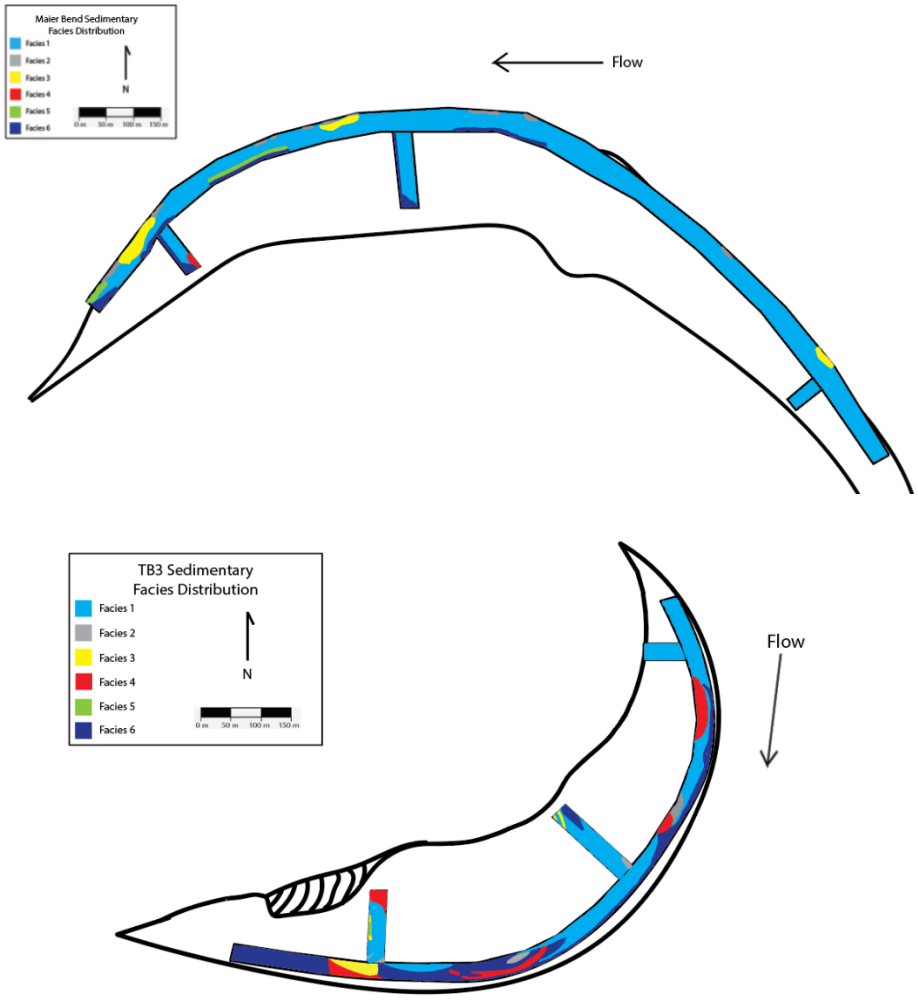

Figure 4.1: Sedimentary facies distribution for the Maier bend and TB3 point bars.

Q2.) How are these facies represented spatially in the alluvial architecture of these bends with different styles of migration?

In both Maier Bend and TB3, Facies 1 (lateral accretion surfaces) dominate throughout the point bar, representing migration of the point bar. At the tail end of each point bar, there is a significant increase in the diversity of facies. Dunes, bar top hollows, and unit bars become more abundant moving from the upstream to downstream sections of the point bar, although it is likely dunes are present throughout, but their stratification may be below the resolution of the GPR.

Facies 2 (unit bars) are only seen on the channel side of the transverse and longitudinal lines of the GPR profiles for Maier Bend and TB3. In TB3, unit bars are present; however, for Maier Bend, unit bars are only present in the downstream end of the GPR profiles. In aerial imagery of the Maier Bend point bar, unit bars are present in the mid-bar section, but are not seen in the GPR profiles. Therefore, the absence of unit bars in the GPR profiles is possibly due to the surveys not being taken close enough to the channel edge. However, if this were the case, it would be expected that unit bars should be interpreted at depth when observing 'deeper' sections of the bend. Another possible explanation is that unit bars that are preserved are incorporated into the lateral accretion surfaces as the high angle surfaces seen in the GPR profiles when the Maier Bend point bar migrates northward. However, this cannot be confirmed easily with just the GPR profiles.

In the aerial imagery, Facies 3 (dunes) is present across most of the point bar and channel, but they are not always seen in the GPR profiles due to the resolution of the GPR, or as their stratification becomes incorporated between the lateral accretion surfaces (Facies 1a). Dunes are especially prominent at the tail end of both Maier Bend and TB3, as apparent in both longitudinal and transverse GPR profiles. Another feature seen at the tail end of the point bars

are bar top hollows, with TB3 possessing a larger and more prominent bar top hollow than Maier Bend.

Facies 4 is only found at the tail end of the point bars. This is because bar top hollows can only form as the tail end of the point bar wraps around the bend and a depositional low is generated.

In Maier Bend and TB3, Facies 5 was interpreted at thalweg depth. However, Facies 5 was also interpreted as being deposited within bar top hollows at the downstream end of the TB3. Facies 5 that is found at thalweg depth is interpreted as planar deposition of gravel, but the Facies 5 that was deposited in the bar top hollows are likely finer sediment deposited at higher flow stages.

Facies 6 is seen in all sections of the point bars. The presence of the hyperbolae is dependent on the amount of material that can cause these point reflectors to form within the profiles.

Q3.) How does the present characterization of depositional facies compare to previous depositional models of meandering rivers?

4.1.1 The Depositional Model of Jackson (1976)

The major inspiration to study the morphology of the Wabash River was the depositional model developed by Jackson (1976a). His model was based on the premise that the depositional facies are dependent on the nature of flow development within bends of different curvature and was developed by examination of trenches in the cutbanks and scroll bars of specific Wabash River bends (Jackson, 1976a). Jackson did not study TB3 but studied the Maier Bend extensively. Figure 4.2 shows the sedimentary logs of Jackson (1976a) based on the Maier and Helm bends, and describes the sedimentary facies seen in scroll bars and transverse bars in the

fully-developed and transitional depositional facies. Jackson (1976a) also displays an intermediate sedimentary log, but this is based on a different bend along the Wabash River with a different migration style and bend curvature. Above the two sediment logs, Jackson displays a sketch of the idealized distribution of depositional facies dependent on bend curvature, although most bends do not follow this idealized pattern. Figure 4.3 shows the inferred distribution of depositional facies based on historical migration of four bends (Jackson, 1976a), showing the intermediate facies for Maier Bend is predicted to be much smaller than in the idealized classic facies model (fully developed flow).

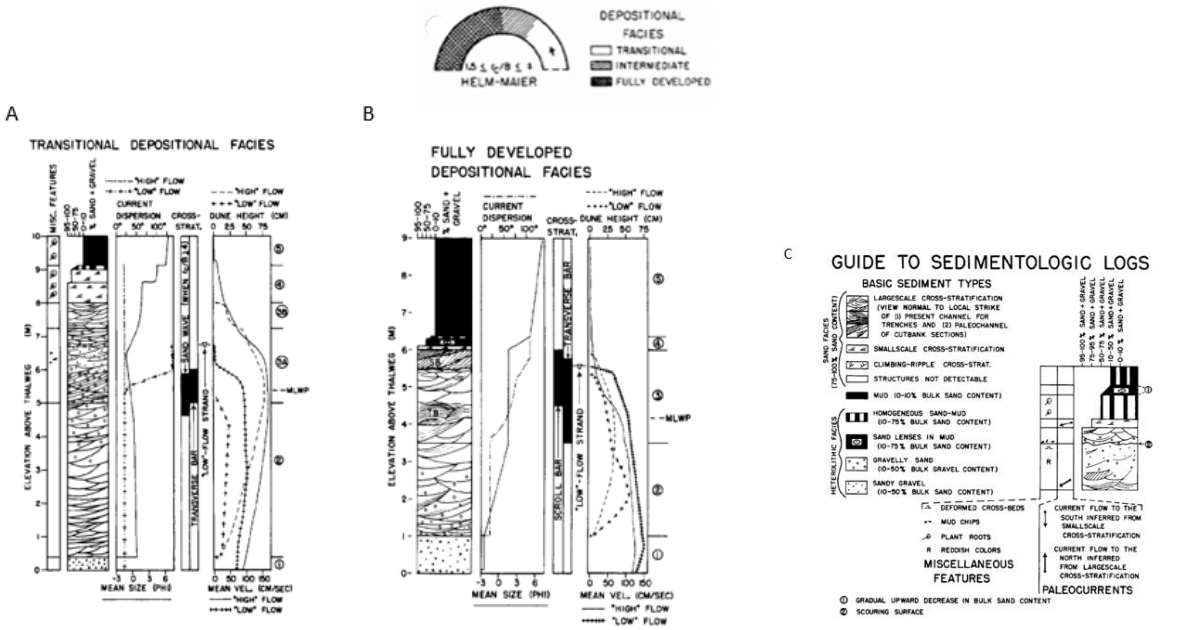

Figure 4.2: The sedimentary logs of Jackson (1976a) for each of his depositional facies based on the Maier and Helm bends in the Lower Wabash River. In the top right of the figure, the image shows the idealized distribution of the depositional facies around the Maier-Helm Bends. When Jackson references current velocity and current bed-material size, it is the velocity and bed-size material at the time he was studying the bends. **A:** Transitional depositional facies. Based on transitional patterns of bedforms, current velocity, and bed-material size around Helm and Maier bends. **B:** Fully developed depositional facies. Based on fully developed patterns of bedforms, current velocity, and bed-material size of Helm and Maier bends. **C:** Explanation of the symbols for the sedimentary logs shown in A and B. From Jackson, 1976a.

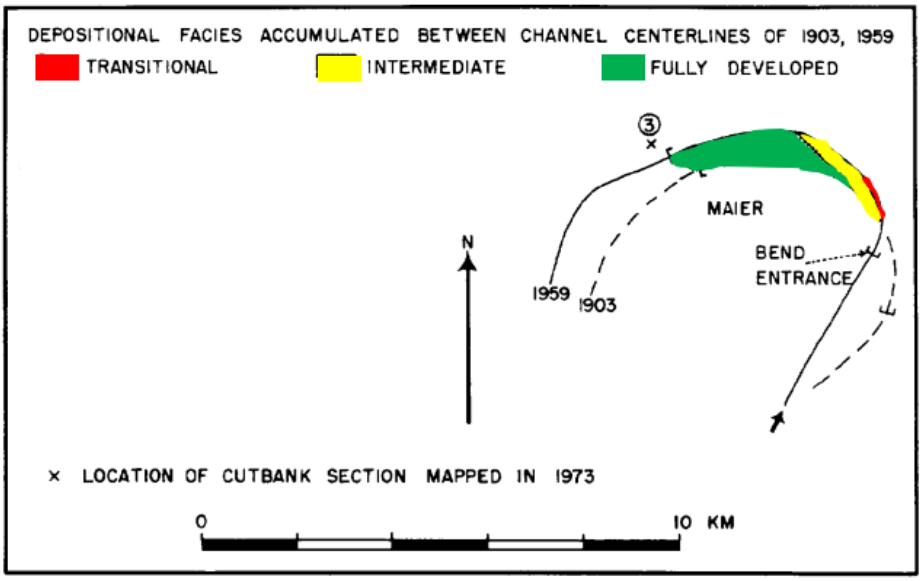

Figure 4.3: Inferred accumulation of depositional facies by historical migration of Maier Bend. The distribution depositional facies proposed by Jackson for Maier Bend is based on its position in 1973. Modified from Jackson 1976b.

The sedimentary logs and descriptions of Jackson (1976a) show cross-stratification that is formed in lateral accretion packages with a general fining upward sequence of grain size (Figure 4.2). This is likely similar to Facies 1a that represents lateral accretion surfaces with packages of dunes and high-angle surfaces in between the strata. To illustrate this, Figure 4.4 shows the sedimentary log of Jackson (1976a) for transitional depositional facies when scaled to an upstream GPR profile for the Maier Bend point bar. Although the sedimentary logs of Jackson (1976a) are more detailed than the GPR profiles, the scale between the interpreted sedimentary features can still be compared. The scale of the cross-stratification does have a similar scale to the small-scale features interpreted in the GPR profile. Additionally, in the sedimentary log, it can be seen that there is an increase in smaller sedimentary features closer towards the surface. This can also be interpreted in this GPR profile (see high-angle surfaces marked in green in Figure 4.4). However, due to the resolution of the GPR, this might not be evident in every GPR

profile. Furthermore, the elevation above the thalweg given in Jackson's sedimentary logs (Figure 4.4) is similar (0-6m) to that in the depth of GPR profiles herein (0-5.5m). However, the GPR panel shows the presence of lateral accretions surfaces that were not recognizable in the vertical logs of Jackson (1976a) that were based on bank sections.

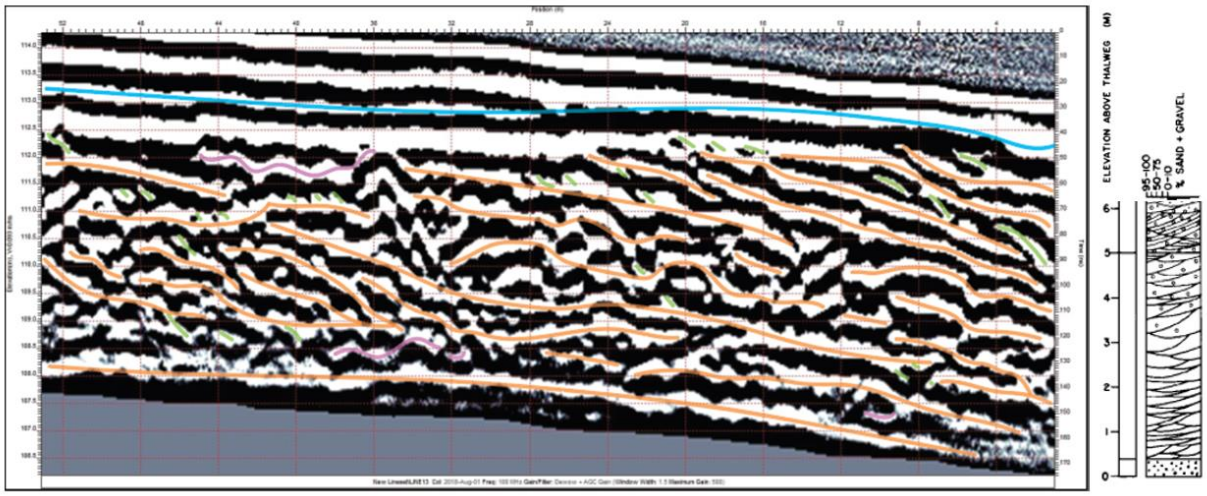

Figure 4.4: Jackson's transitional depositional facies (1976a) scaled to an upstream GPR profile in Maier bend, showing that the scale of bed forms in Jackson's (1976a) log are a similar scale to the sedimentary facies found in the GPR profiles.

When comparing the facies described by Jackson (1976a; Table 4.1) to the facies quantified in the present research, several similarities are apparent. One facies that is seen in both is Facies 2 (unit bars), with the transverse bars of Jackson (1976a) being described in this thesis as unit bars. Figure 4.5 shows an image from Jackson (1976a) displaying a transverse bar that is somewhere along the mid-bar to downstream section of Maier Bend. When comparing Jackson's image of transverse bars to unit bars on Maier Bend (Figure 3.9), they appear to be the same.

Attributes	Dunes	Sand waves	Transverse bars	Scroll bars
Streamwise vertical profile	Asymmetric wave	Asymmetric wave and symmetric wave about equally common; rare scour trough	Highly asymmetric triangular wave, often with scour trough	Asymmetric wave, never with scour trough
Crest-to-trough height (cm)*	5–120	50–250	30–200	10–200
Wavelength (m)*	1–30	20–60	Often solitary † 20–500	Usually solitary † 10–40
Mean velocity magnitude (cm/s)*	50–180	130–180	40–130	20–80 over crest 0–20 over trough
Depth over crest (cm)*	30–1200	300–900	30–500	1–50
Mean particle size of bed material (mm)	0·3–3·5	1·5–3·5	0·4–1·0	0·3–1·0
Bedforms superimposed on stoss-sides	Usually none: on dunes greater than 50 cm high, rarely smaller dunes	Dunes always superimposed	Always dunes near crest. Often dunes on entire stoss-side and in trough	Near crest: smallscale ripples, dunes less than 15 cm high, upper-regime plane bed
Times of development and migration‡	1-maximum	4-maximum	1–7	1–3
Hydrodynamic interpretation	Dunes of Simons, Richardson & Nordin (1965)	Dunes in deep, strong flows over coarse bed materials	§	Gilbert-type delta
Flow separation observed over lower slipface and trough?	Never	Never	Rare, weak separation	Frequently, but usually indefinite owing to near-zero trough velocities

* Measured over bedform crest, when bedform is actively migrating.
† Only one along a bend or along a straight reach.
‡ River stage, in metres, at gaging station at Mt Carmel, Illinois.
§ Deep-flow analogues of barlike bedforms of Costello & Southard (1974). Perhaps analogues to the sand waves of Boothroyd (1969) and of Boothroyd & Hubbard (1974).

Table 4.1: Attributes of largescale ripples in the Lower Wabash River. From Jackson 1976b.

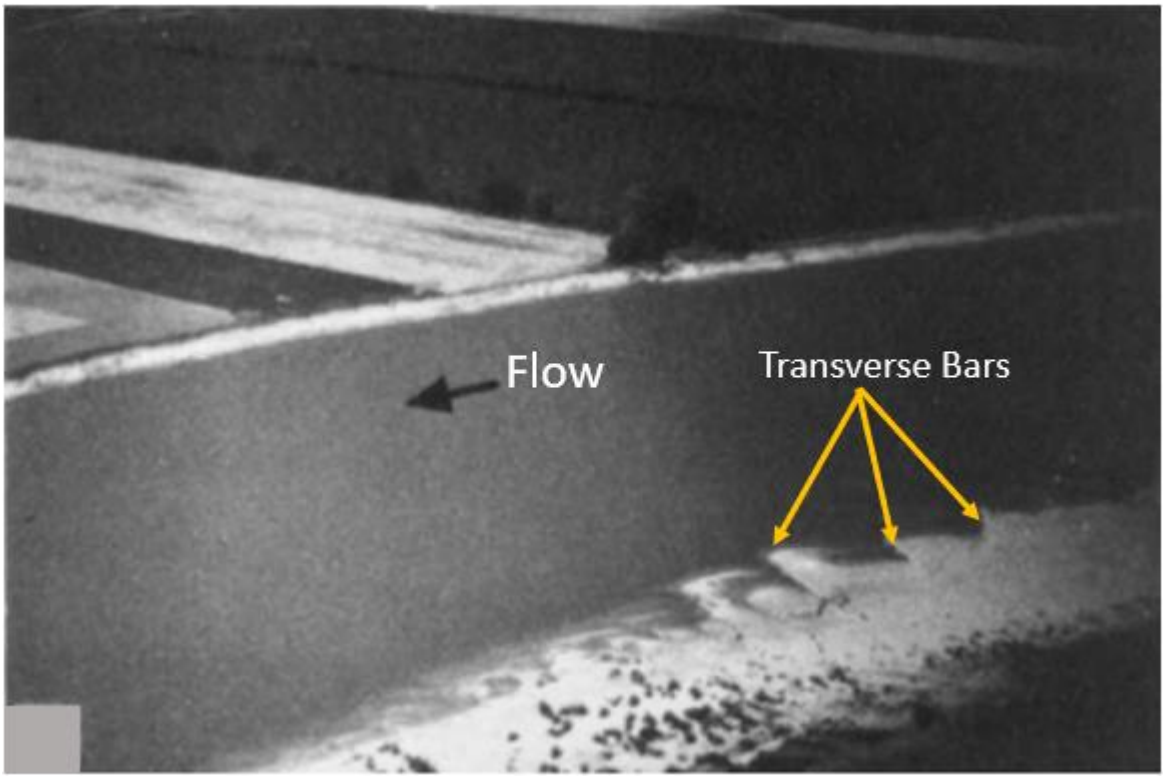

Figure 4.5: Oblique view of five transverse bars near Maier traverse 4, on 24 June 1972. Average crestline-to-crestline spacing of four leftmost bars is about 25 m. From Jackson, 1976b.

Additionally, the scale of the transverse bars is very similar to the scale of unit bars described in this thesis. Figure 4.6 shows Jackson's (1976a) sediment log for the fully developed facies in comparison to a transverse GPR profile from this thesis. The GPR profile is from the downstream end of the Maier Bend point bar and where Jackson stated his fully developed facies would occur (figures 4.2 & 4.3). When comparing the sediment log to the GPR profile, we can see the transverse bars that Jackson describes occurring at roughly the same depth as they occur in the profile (see unit bars marked by pink line on GPR profile in Figure 4.6). However, Jackson only shows transverse bars between 4 and 5 meters above the thalweg, but not deeper like the unit bars that are seen in the GPR profile (Figure 4.6).

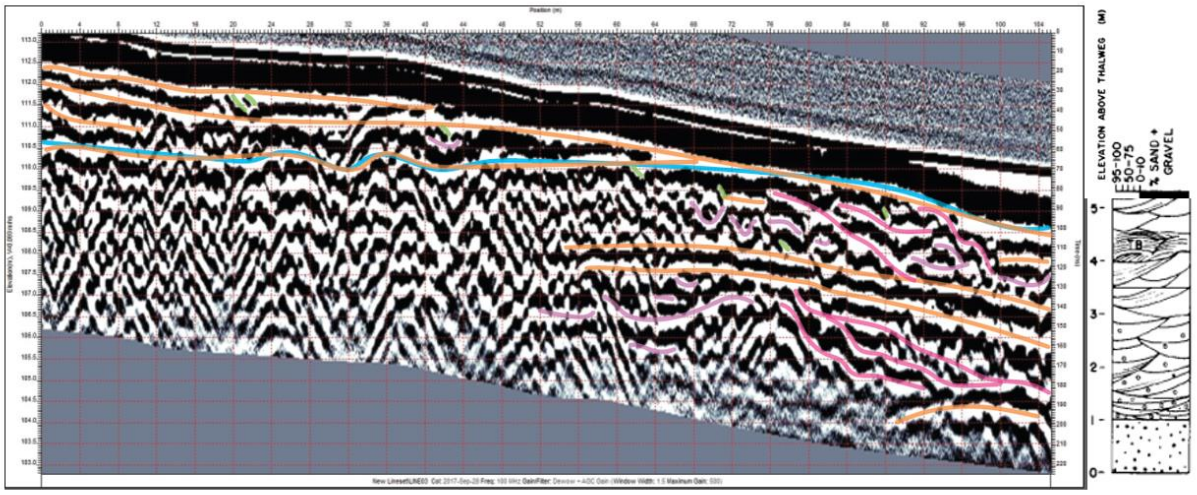

Figure 4.6: Jackson's fully developed depositional facies (1976a) scaled to a downstream depositional GPR profile in Maier Bend, showing that the scale of bedforms in Jackson's (1976a) log are a similar scale to the sedimentary facies found in the GPR profiles.

Additionally, Jackson (1976b) describes transverse bars as being as long as half the local channel width, with wavelength of the transverse bars are roughly 20-500m, and a crest-to-trough height of 30-200cm (0.3-2m) (Jackson, 1976b). In Table 3.1, unit bars are described as 0.2-2m thick and are comparable to the crest-to-trough height reported by Jackson. The unit bars stretch across Maier Bend for c. 30-150m and are similar to the wavelength given by Jackson (20-500m). This

variable distance is because these transverse bars were solitary (Jackson, 1976b), as also observed for the unit bars in this thesis. Lastly, Jackson (1976b) describes dunes superimposed on the stoss side of the transverse bars, which is also evident in the aerial imagery studied herein, where dunes can be seen on the stoss side of unit bars in Maier Bend (Figure 4.7).

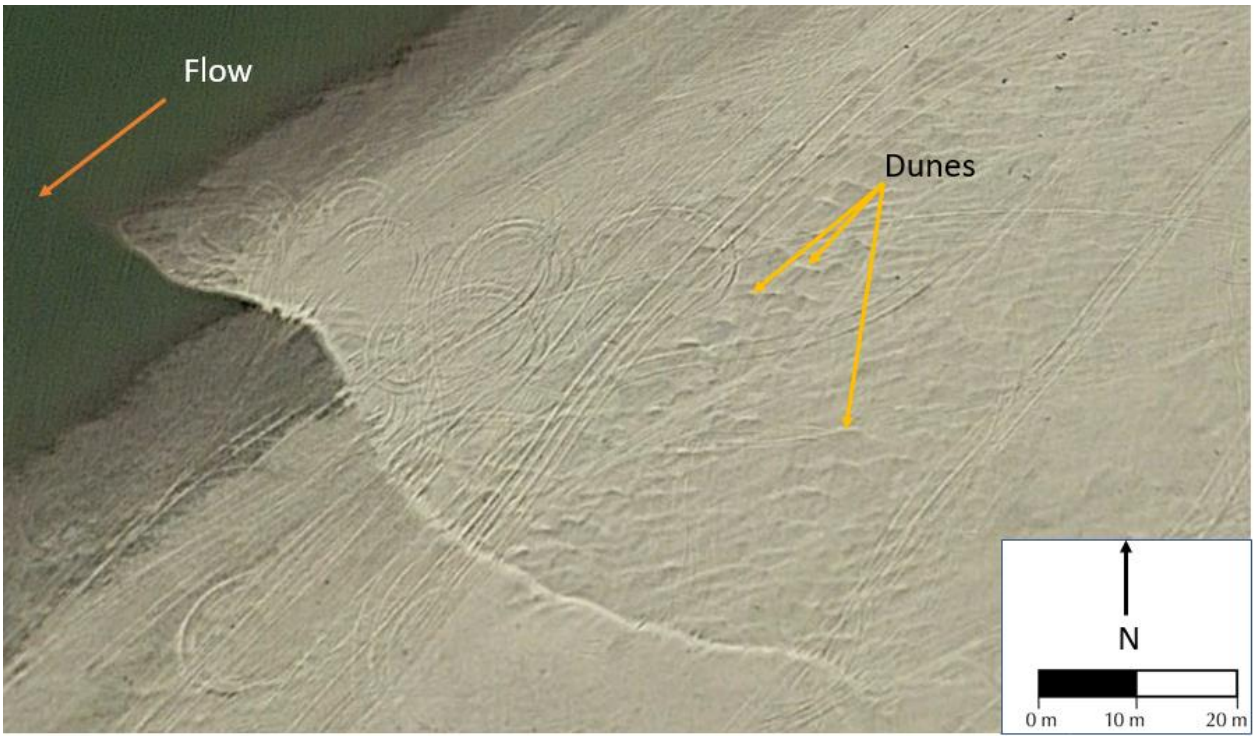

Figure 4.7: Unit bar on the downstream end of Maier Bend with dunes are superimposed on the stoss side.

Dunes are another sedimentary feature that Jackson identified as prevalent in his model. Jackson (1976b) refers to dunes as the most common and widespread large bedform at all flow stages. Although dunes were not seen in all of the GPR profiles in the present thesis, dunes can be seen on the surface of the Maier Bend point bar in aerial imagery and MBES plots (Figures 3.3, 3.4, and 3.5). The crest-to-trough height for dunes were described as roughly 0.05-1.2m (Jackson, 1976b), which is close to the height of the dunes described in this thesis (0.15-0.5m). As stated above, it is likely that more dune-scale cross-stratification is present than revealed in the GPR profiles herein, due to the scale of the dunes being smaller than the GPR resolution.

Thus, many of the structureless sections in between larger reflectors (such as those in Facies 1a) are likely characterized by dunes, as shown in the sedimentary logs given in Jackson (1976a).

A facies identified in this thesis that was not found by Jackson is Facies 4 (bar top hollows), possibly because the areas that Jackson trenched did not contain any bar top hollows that the current thesis has shown only occur in a specific part of the point bar. In addition, Jackson did not study TB3 that has been shown herein to have a larger, and more evident, bar top hollow than in Maier Bend.

4.1.2 Interpretation of Bedding Geometry by Willis (1993)

Willis (1993) developed a theoretical model to predict variation in the three-dimensional geometry of meander bend large-scale stratigraphy with varying bend geometry and hydraulics. This theoretical model was then applied to bedding geometry of outcrops from the Devonian Catskill Magnafacies (NY, USA) and the Miocene Siwalik Group (Potwar Plateau, Pakistan) to determine the migration pattern that occurred during deposition of these ancient sequences (Willis, 1993). Figure 4.8 shows the progressive changes in simulated point bar geometry after each migration step for differing styles of bend migration.

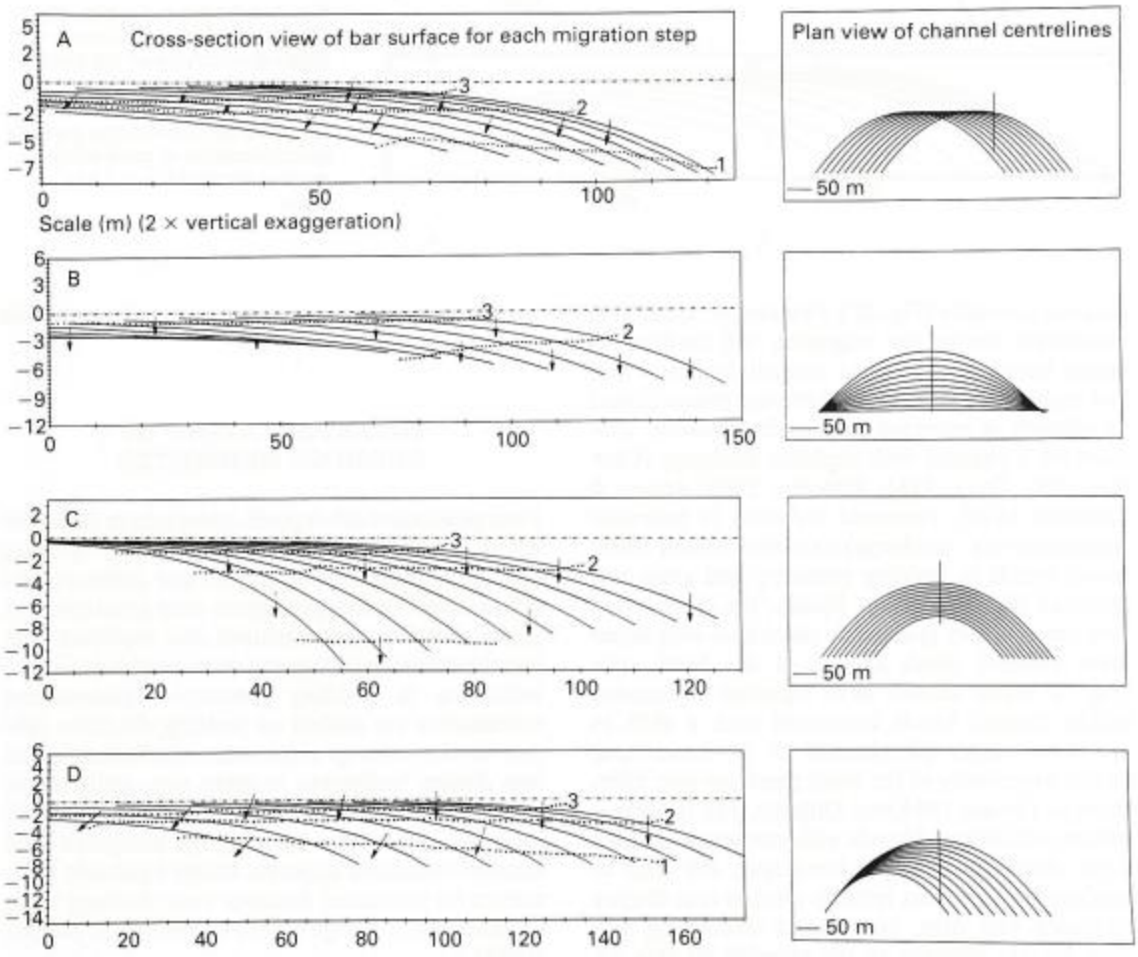

Figure 4.8: Profiles displaying progressive changes in simulated bar geometry as viewed in a plane perpendicular to the channel belt axis. Solid lines show apparent bar geometry after each migration step. Grain size contours (in phi increments) are displayed by dotted lines. Arrows show downstream channel orientation relative to the cross-section's exaggeration. Cross-section orientation relative to migrating channel centerline is displayed in box to the right of profiles. **A:** Variation in apparent bar geometry due to down valley bend translation; cross-sections progress from bend cross-over to bend apex positions. **B:** Progression of apparent point bar geometry due to sinuosity increase. All sections pass through the bend apex. **C:** Variation in apparent bar geometry with increasing bend wavelength. All profiles pass through the bend apex. **D:** Apparent bed geometry produced by increasing bend wavelength and progression from bend crossover to bend apex cross-sections. From Willis, 1993.

Figure 4.8B displays the progression of apparent point bar geometry due to an increase in sinuosity in both a plan view and cross-section view of bar surface for each migration step. Additionally, the grain shows a fining upward pattern from 2-3 phi (dotted lines in Figure 4.8B). Based on the plan view image, Fig. 4.8B represents expansion of the point bar similar to that in Maier Bend. Therefore, in the simulation for Fig. 4.8B, it is expected that at the apex of the bend

the lateral accretion surfaces will show low-angle deposition with very little increase in the angle of deposition when observing the channel side of the point bar. Figure 3.5 shows the slope of the Maier bend point bar from the interior of the bar to the channel for the upstream, mid-bar, and downstream sections. The slope of the point bar ranges between 1-2 degrees, which is similar to Willis's (1993) model. The slope flattens at the top, but increases in the slope angle closer to the channel side of the bend. Although the slopes are similar in shape and angle, grain size also plays a major role in the angle of bedding geometries, and the sediment grain size differ greatly between Willis's model and Maier Bend. The sediment in the Maier bend point bar ranges between -3 (pebble) to 6 (medium silt) phi (Jackson, 1976a) whereas the maximum grain size in Willis's (1993) model is 3 phi. Therefore, even though the slopes are similar in shape (Figure 4.9), the model is not entirely comparable to the point bar in Maier Bend.

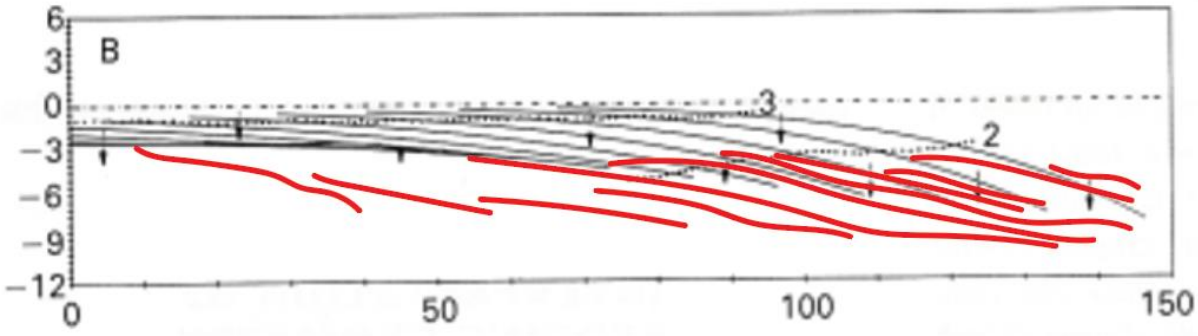

Figure 4.9: Lateral accretion reflection surfaces (red lines) overlain on Willis's cross-sectional view of apparent bar geometry for an expanding point bar.

Figure 4.8A represents variation in apparent bar geometry due to down valley bend translation and represents a transverse view of the bend apex. In the cross-section, the bar surface accretes as low-angle surfaces at first, but then steepens as the accretion surfaces move closer to the channel. In TB3, the bend apex at the time the GPR surveys were taken are closer to the upstream end of the point bar (Rowley, 2020). For the GPR surveys near the bend apex, there

are low-angle accretion surfaces in all of the profiles, and some steepen into unit bars when observed closer to the channel side. In the point bar surface profiles shown in Chapter 3 (Figures 3.4 and 3.5), the slope from the interior of the point bar can be seen as low-angle, but then steepens towards the channel. Therefore, the slope shape of TB3 and Willis's (1993) model are roughly similar (Figure 4.10). However, their absolute slopes are quite different. The slope from the interior to the channel side of the point bar ranges from 2.4-2.9 degrees for TB3 while the slope of Willis's model is closer to 4 degrees (Willis, 1993). Again, this is likely due to the difference in grain size, or because TB3 also has some characteristics of an expanding point bar.

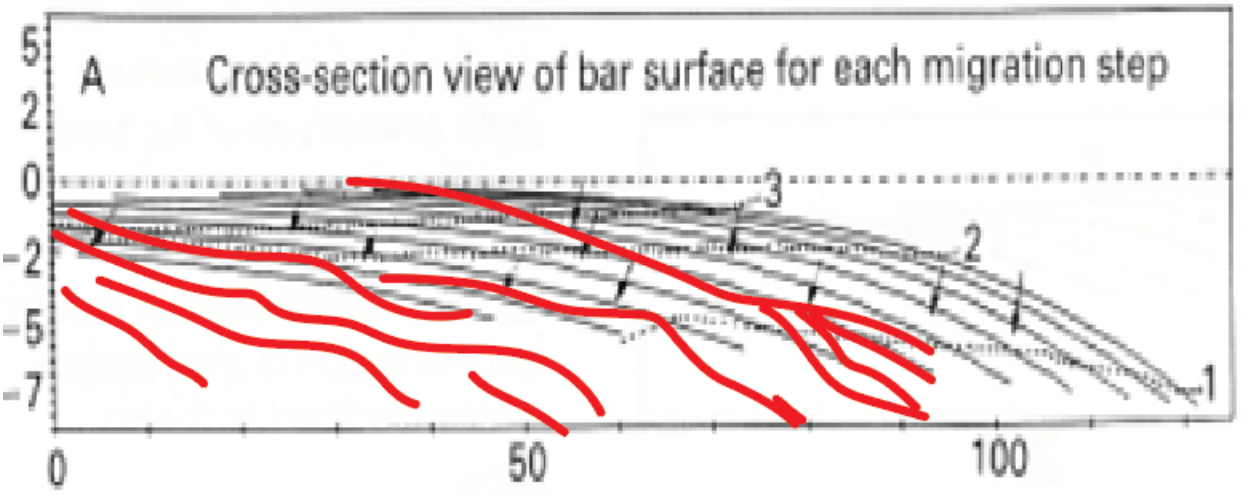

Figure 4.10: Lateral accretion reflection surfaces (red lines) overlain on Willis's cross-sectional view of apparent bar geometry for a translating point bar.

4.1.3 The Effects of Accretion-package Geometry on Lithofacies Distribution in Point-bar Deposits by Hagstrom et al.

Hagstrom et al. (2019) aimed to show that the accretion-package geometry affects the lithological variability of point bars. Based on high-quality 3-D seismic data and information from hundreds of wellbores from the Lower Cretaceous McMurray Formation in Alberta, Canada, five recurring accretion-package geometries were determined: uniform width, wide at

apex, narrow at apex, downstream wedge, and upstream wedge (Hagstrom et al., 2019). Each of these recurring accretion-package geometries are commonly associated with different modes of migration (Hagstrom et al., 2019). Furthermore, there are certain lithologic patterns that Hagstrom et al. (2019) observed in relation to certain accretion-package geometries. Also, based on the data, the point bars that have a higher planform complexity due to multiple modes of migration may exhibit more lithological variability than a single migration mode (Hagstrom et al., 2019).

The formation that is studied in Hagstrom et al. (2019) is primarily composed of three facies: sandstone, interbedded sandstone and mudstone, and mudstone which is a different grain size distribution than that present in the modern Wabash River. The Wabash River consists of grain sizes that are gravel to fine grained sand and sometimes silt (Jackson, 1976a). Therefore, this difference in grain size distribution would not make these studies a perfect comparison. However, what can be compared between the two studies is the geometries of the accretion-packages. The accretion packages created by meander migration can be observed on the floodplains, in the 3-D seismic datasets, and outcrops of point bar deposits (Hagstrom et al., 2019). As mentioned in the previous paragraph, the specific accretion-package geometries are associated with specific bend migration styles. Maier Bend exhibits expansion, which based on the data collected and observed by Hagstrom et al. (2019), is associated with uniform width (Figure 4.11).

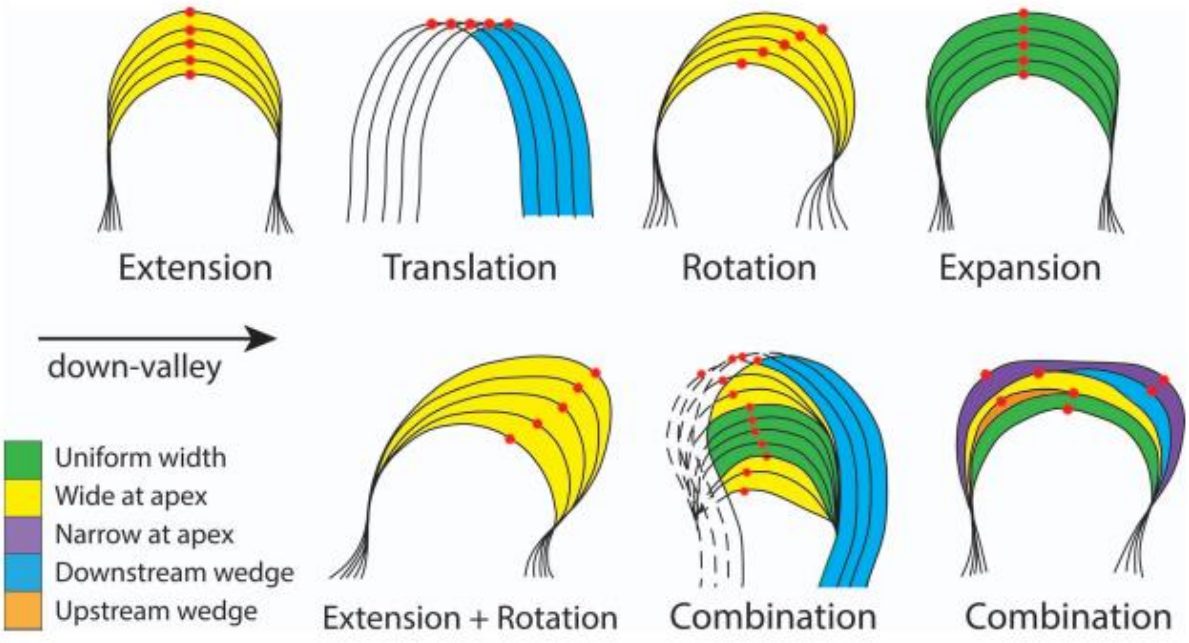

Figure 4.11: Accretionary styles created by different modes of meander migration (Daniel, 1971). Red dots are points of maximum bend curvature. Flow is clockwise. From Hagstrom et al., 2019.

Uniform width accretion-package geometry is described as accretion-geometry packages that extend from point-bar head to >50% of the distance between bar apex and tail; the ratio of maximum to minimum accretion package width is <2.5 (Hagstrom et al., 2019). In other words, the accretion packages starting at the bar head are 50% or less in length than the length from the bar apex to bar tail. Also, the smallest width of the accretion package is 2.5 times smaller than widest part of the accretion packages. The width of the lateral accretion surfaces is unfortunately not comparable just from the GPR profiles, but the length can be measured by measuring the length of the interpreted lateral accretion surfaces within the GPR profiles. The distance from the Maier Bend point bar apex to the bar tail is *c.*700m (Fig. 2.4; Rowley, 2020). The accretion surfaces are about 20-150m in length at the upstream end of the point bar. Therefore, it is >50% the length from the bar apex to tail as described by Hagstrom et al. (2019).

The TB3 bend exhibits both expansion and translation downstream. Consequently, it could exhibit both the accretion-package geometries described by Hagstrom et al. (2019),

including uniform width as well as a downstream wedge. The downstream wedge accretion-package geometry is described that the maximum accretion package width is found downstream of the bar apex (Hagstrom et al., 2019). Also, the accretion package does not extend upstream of the bar apex (Hagstrom et al., 2019). The bar apex for TB3 is located at the upstream end of the point bar (Fig 2.4; Rowley, 2020), meaning that the accretion-package geometries do not, and cannot, extend upstream. As in Maier Bend, the width of lateral accretion surfaces also could not be measured in the GPR profiles for TB3.

4.2 Conclusions

This research has found that the sedimentology of bends in the Wabash River comprise six facies: Facies 1a (lateral accretion surfaces with small scale features in between the surfaces), Facies 1b (lateral accretion surfaces with no small scale features), Facies 2 (unit bars), Facies 3 (dunes), Facies 4 (bar top hollows), Facies 5 (planar deposition surfaces), Facies 6 (hyperbolae). Facies 1a and 1b (lateral accretion surfaces) are found throughout the point bars and are the most abundant facies found within both point bars. The presence of 1a versus 1b depends on grain size, size of the small-scale features between the lateral accretion surfaces, and the resolution of the GPR profiles. Facies 2 (unit bars) is primarily found on the channel side of the longitudinal and transverse GPR profiles. Facies 3 (dunes) can be found anywhere within the point bar but are seen the most at the downstream end of point bars. Facies 4 (bar top hollow) is only found at the downstream end of the point bars. Facies 5 (planar deposition) is found primarily at thalweg depth or filling bar top hollows and is the least abundant facies found within both point bars. Facies 6 can be found anywhere within the GPR profiles but are dependent on the presence of objects that would cause hyperbolae in profile.

This research has found that there are similarities between the sedimentary facies of Maier Bend and TB3, bends that possess migration characteristics that are dominated by expansion and translation respectively. However, distinct differences exist between the two bends, particularly at their downstream ends. Bend TB3, which has a dominantly translational migration, possesses a more significant variety in facies at the downstream end of its point bar, with a prominent bar top hollow and presence of dunes. Maier Bend also has an increase in the diversity of its sedimentary facies at the downstream end of its point bar, but it is not as marked as seen in TB3. This difference in diversity of facies is likely due to the translation that TB3 experiences whereas Maier bend only experiences expansion.

When comparing the present results with the depositional model of Jackson (1976a), there are strong similarities in the types of sedimentary facies between the two studies, notably in the presence of unit bars (transverse bars in Jackson, 1976a), dunes, and accretion surfaces. The principal difference is that Jackson (1976a) did not recognize bar top hollows, which as shown herein are more poorly developed at Maier Bend, and possibly the other bends studied by Jackson (1976a).

The slopes of Maier Bend are similar to the slopes calculated in Willis's model and are visually quite similar (Figure 4.9); however, the Maier Bend and Willis's model (1993) differ greatly in reference to grain size. Bend TB3 accretion surfaces also visually somewhat match the model of Willis (1993) in shape (Figure 4.10), but the slope angles are dissimilar. Bend TB3's point bar also has a different grain size distribution to the simulations of Willis (1993).

Lastly, the data of this thesis was also compared to the model of Hagstrom et al. (2019). The model of Hagstrom et al. (2019) focused on relating lithofacies distributions to specific accretion-geometry packages based on how the bend migrated. This thesis focused on comparing

the accretion-geometries established in the model to that present in the two Wabash bends, rather than how the lithofacies distribution is affected. It was found that Maier Bend was not entirely comparable to the proportional changes expected to be seen in the accretion-geometry packages, but did agree with the overall conclusion that the expanding point bars create accretion packages formed by sedimentation concentrated at the bar apex (Hagstrom et al., 2019). Bend TB3's point bar also exhibits the major conclusion that Hagstrom et al.'s model (2019) determined which is the greatest deposition is seen on the downstream end of the point bar and the "wedge" shape is clearly visible.

4.2.1 Future Research

The present research focused on developing a facies scheme for point bars with two different modes of migration, and the scheme also quantified the frequency of each facies throughout the two point bars. Although this research is another step towards understanding point bar morphology, there is still more that needs to be conducted to further understand point bar morphology and its preservation in the rock record.

First, additional work needs to be completed for Maier and TB3 along with other point bars within the Wabash River to assess the sedimentary facies to the full depth of the channel thalweg. It would be beneficial to resurvey the bend with an enhanced Sensors and Software Ultra Receiver GPR. In theory, this enhanced GPR system can image twice as deep as the present data, and thus possibly to thalweg depth. By imaging to thalweg depth, features that are too deep to be visible in current GPR profiles may be quantified, allowing the full lateral accretion surfaces to be imaged. Also, by collecting more GPR data, there would be an opportunity to create detailed 3-D grids to better visualize how the features in the transverse and longitudinal lines relate to one another. Additionally, shallow coring should be conducted to

ground truth the new GPR data. Along with applying this methodology to TB3 and Maier bends, this methodology could also be applied to other point bars in the Wabash River to test and improve the current facies scheme. This methodology could also be applied to other meandering rivers of a similar, or larger, scale to see how they compare. Future work applying the methods used in this thesis to large meandering rivers would provide an opportunity to test features that may be scale-dependent or scale-invariant in the facies of meandering rivers. More context concerning which features in a meandering river of similar scale may be present and preserved, will make it easier to predict which facies may be preserved in the rock record and their formative processes.

REFERENCES

Allen, J. R. L., 1964, Studies in fluviatile sedimentation: Six cyclothems from the Lower Old Redstone, Anglo-Welsh Basin, Sedimentology, v. 3, p. 163-198

Allen, J. R. L., 1970a, Studies in fluviatile sedimentation: A comparison of fining upwards cyclotherms with special reference to coarse-member composition and interpretation, Journal of Sedimentary, v. 40, p. 298-323

Allen, J. R. L., 1970b, A quantitative model of grain size and sedimentary structures in lateral deposits, Geological Journal, v. 7, p. 129-146

Alvarez, C. A. and Franklin, E. M., 2017, Formation and morphology of subaqueous barchan dunes, 24th ABCM International Congress of Mechanical Engineering, Dec. 3-8, 2017, Curitiba, P. R. Brazil, p. 1-6, http://www.sistema.abcm.org.br/articleFiles/download/8970

Baker G. et al., 2007, An introduction to ground penetrating radar (GPR), The Geological Society of America Special Paper 432, p.1-18, https://pubs.geoscienceworld.org/books/book/586/chapter/3803983/An-introduction-to-ground-penetrating-radar-GPR

Best, J. L., 2005, The fluid dynamics of river dunes: A review and some future research directions, Journal of Geophysical Research, v. 110, i. F4, p.1-21, https://doi.org/10.1029/2004JF000218

Blindow, N., Ground Penetrating Radar, Environmental Geology, Springer-Verlag, p. 283-335, http://dx.doi.org/10.1007/978-3-540-74671-3_10

Bridge, J. S., 1975, Computer Simulation of sedimentation in meandering streams, Sedimentology, v. 22, p. 3-44

Bridge, J. S., 1977, Flow, bed topography and sedimentary structure in open channel bend: a three-dimensional model, Earth Surface processes, v. 2, p. 281-294

Bristow C. S. and Jol H. M., 2003, An introduction to ground penetrating radar (GPR) in sediments, Jol H. M. and Bristow C.S., Ground Penetrating Radar in Sediments, Geological Society Special Publication 211, p.1-8

Collinson, J.D., 1978, Alluvial Sediments, Sedimentary Environments and Facies, Blackwell Scientific Publications, p. 20-42

Daniel, J.F., 1971, Channel movement of meandering Indiana streams: U.S. Geological Survey, Professional Paper 732-A, p.1-18

Daniels, D., 2009, Antennas, Jol H. M. and Bristow C.S., Ground Penetrating Radar: Theory and Application, p.99-139, Elsevier Science, https://www.sciencedirect.com/book/9780444533487/ground-penetrating-radar-theory-and-applications

Ghinassi, M., et al., 2014, Plan-form evolution of ancient meandering rivers reconstructed from longitudinal outcrop sections, Sedimentology, v. 61, p.1-26, https://www.researchgate.net/publication/259556010_Plan-form_evolution_of_ancient_meandering_rivers_reconstructed_from_longitudinal_outcrop_sections

Ghinassi, M., et al., 2016, Downstream-migrating fluvial point bars in the rock record, Sedimentary Geology, v. 334, p. 66-96, http://dx.doi.org/j.sedgeo.2016.01.0050037-0738/

Herbert, C. M., et al., 2019, Unit bar architecture in a highly-variable fluvial discharge regime: Examples from the Burdekin River, Australia, Sedimentology, v. 67, i. 1, p. 576-605, https://doi.org/10.1111/sed.12655

Hickin, E.J., 1978, Meandering Channels, Sedimentology, Encyclopedia of Earth Science, Springer, Berlin, Heidelberg, p. 703-709, https://doi.org/10.1007/3-540-31079-7_134

Jackson, R. G., 1975a, A depositional model of point bars in the lower Wabash River, PhD dissertation, Univ. of Ill., Urbana-Champaign., https://www.proquest.com/dissertations-theses/depositional-model-point-bars-lower-wabash-river/docview/302741230/se-2?accountid=14553

Jackson, R.G., 1975b, Velocity-bedform-texture patterns of meander bends in the lower Wabash River of Illinois and Indiana, v. 86, i. 11, p. 1511-1522, https://dx-doi-org.proxy2.library.illinois.edu/10.1130/0016-7606(1975)86%3C1511:VPOMBI%3E2.0.CO;2

Jackson, R.G., 1976a, Depositional Model of Point Bars in the Lower Wabash River., Journal of Sedimentary Petrology, v. 46, p. 579-594., https://doi-org.proxy2.library.illinois.edu/10.1306/212F6FF5-2B24-11D7-8648000102C1865D

Jackson, R. G., 1976b, Largescale ripples of the lower Wabash River, Sedimentology, v. 23, i. 5, p. 593-623, https://doi-org.proxy2.library.illinois.edu/10.1111/j.1365-3091.1976.tb00097.x

Jopling, A.V., 1966, Some applications of theory and experiment to the study of bedding genesis, Sedimentology, v. 7, p. 71-102, https://onlinelibrary-wiley-com.proxy2.library.illinois.edu/doi/10.1111/j.1365-3091.1966.tb01580.x

Julien, P. Y., 2018, River Engineering, River Mechanics, Cambridge University Press, p. 379-426, https://doi.org/10.1017/9781316107072.015

Konsoer, K. M., et al., 2016a, Three-dimensional flow structure and bed morphology in large elongate meander loops with different outer bank roughness characteristics, Water Resources Research, v. 52, i. 12, p. 9621-9641, https://doi.org/10.1002/2016WR019040

Konsoer, K. M., et al., 2016b, Spatial variability in bank resistance to erosion on a large meandering, mixed bedrock-alluvial river, Geomorphology, v. 252, p. 80-97, http://dx.doi.org/10.1016/j.geomorph.2015.08.002

Lunt, I. A. and Bridge, J. S., 2007, Formation and preservation of open-framework gravel strata in unidirectional flows, Sedimentology, v. 54, p. 377-414, https://onlinelibrary-wiley-com.proxy2.library.illinois.edu/doi/10.1111/j.1365-3091.2004.00627.x

Martinez, A. and Byrnes, A. P., 2001, Modeling Dielectric-constant values of Geologic Materials: An Aid to Ground-Penetrating Radar Data Collection and Interpretation, Current Research in Earth Sciences, p.1-16, https://www.kgs.ku.edu/Current/2001/martinez/martinez.pdf

Miall, A. D., 1981, Facies Models for Meandering Rivers, Analysis of Fluvial Depositional Systems, American Association of Petroleum Geologists, v. 20, p.32-38 , https://doi-org.proxy2.library.illinois.edu/10.1306/CE20422

Nagayama, S. and Nakamura, F., 2018, The significance of meandering channel to habitat diversity and fish assemblage: a case study in the Shibetsu River, northern Japan, Limnology, v. 9, i. 1, p. 7-20, https://doi.org/10.1007/s10201-017-0512-4

Neal A., 2004, Ground-penetrating radar and its use in sedimentary: principles, problems, and progress, Earth Science Reviews, v. 66, p. 261-330, https://www.sciencedirect.com/science/article/abs/pii/S0012825204000054

Park, S. W. & Ahn, J., 2019, Experimental and numerical investigations of primary flow patterns and mixing in laboratory meandering channel, Smart Water, v. 4, p. 1-15, https://doi.org/10.1186/s40713-019-0016-y

Rhoads, B. L., 2020, River dynamics: geomorphology to support management, Cambridge University Press, p. 197-233, https://doi.org/10.1017/9781108164108.009

Robinson, M., et al., 2013, Ground Penetrating Radar, Geomorphological Techniques: Part 1, Sec. 5.5, British Society for Geomorphology, p.1-26, https://www.geomorphology.org.uk/sites/default/files/geom_tech_chapters/1.5.5_GPR.pdf

Rowley, T., 2020, Field Investigation on point bar dynamics and planform evolution in meandering rivers, PhD dissertation, Louisiana State University, https://digitalcommons.lsu.edu/cgi/viewcontent.cgi?article=6196&context=gradschool_dissertations

Rowley, T., et al., 2021, Relationship of point bar morphology to channel curvature and planform evolution, Geomorphology, v. 375, p.1-20, https://doi-org.proxy2.library.illinois.edu/10.1016/j.geomorph.2020.107541

Sambrook Smith, G. H., 2006, The sedimentology and alluvial architecture of the sandy braided South Saskatchewan River, Canada, Sedimentology, v. 53, p.413-434, https://doi.org/10.1111/j.1365-3091.2005.00769.x

Sensors and Software, 2018, Ekko Project: Processing Module, User's Guide, Sensors and Software Inc., p. 1-91, https://www.sensoft.ca/wp-content/uploads/2018/04/Processing-Module-Users-Guide.pdf.

Shan, J. F., et al., 2018, Reconstruction of meandering paleo-channels using dense well data, Daqing Oil Field, Songliao Basin, China, Petroleum Science, v. 15, p. 722-743, https://doi.org/10.1007/s12182-018-0270-x

Smith, N. D., 1971, Transverse bars and braiding in the Lower Platte River, Nebraska, Geological Society of America Bulletin, v. 82, p. 3407-3420, http://scholar.google.com.proxy2.library.illinois.edu/scholar_lookup?hl=en&volume=82&publication_year=1971&pages=3407-3420&journal=Geol.+Soc.+Am.+Bull.&author=N.D.+Smith&title=Transverse+bars+and+braiding+in+the+Lower+Platte+River%2C+Nebraska

Smith, N. D., 1974, Sedimentology and bar formation in the upper kicking horse river, a braided outwash stream, Journal of Geology, v. 82, n. 2, p. 205–223, http://www.jstor.org/stable/30061976?origin=JSTOR-pdf

Smitha, N., et al., 2016, Kirchoff and F-K migration to focus ground penetrating radar images, International Journal of Geo-Engineering, v. 7, p 1-12, https://doi.org/10.1186/s40703-016-0019-6

Stierman, D., et al., 2005, Geophysical and GIS Investigations of the Oak Openings Sand Ridge in NW Ohio, North Central Meeting of the Geological Society of America in Minneapolis, May 19th, http://www.eeescience.utoledo.edu/faculty/stierman/oakopen/gsa/P05.htm

Tkchenko, N. V., 2006, Optics and Optical Devices, Optical Spectroscopy, Elseiver Science, p. 15-38, https://doi.org/10.1016/B978-044452126-2/50026-5

Utsi, E. C., 2017, Ground Penetrating Radar: Theory and Practice, Butterworth-Heinemann, p.1-11, 84-90, https://www.elsevier.com/books/ground-penetrating-radar/carrick-utsi/978-0-08-102216-0

van Bendegom, L., 1947, Eenige beschouwingen over riviermorphologie en rivierbetering, De Ingenieur, v. 59, i. 4, p. 1-11

Walker, R. G. & Cant, D.J., 1984, Sandy fluvial systems, Facies Models, Geoscience Canada, 2nd Ed., p. 71-89, http://www.muststayawake.com/SDAG/library/ESS/Walker_Cant(Fluvial)198x.pdf

Ward, J. V. and Stanford, J.A., 1995, Ecological connectivity in alluvial river ecosystems and its disruption by flow regulation, Regulated Rivers: Research and Management, v. 11, p. 102-119, https://onlinelibrary.wiley.com/doi/epdf/10.1002/rrr.3450110109

Woodward, et al., 2003, The use and application of GPR in sandy fluvial environments: methodological considerations, Jol H. M. and Bristow C.S., Ground Penetrating Radar in Sediments, Geological Society Special Publication 211, p. 127-141, https://www.researchgate.net/publication/249551195_The_use_and_application_of_GPR_in_sandy_fluvial_environments_Methodological_considerations